Predicting the Spatio-Temporal Evolution of Tumor Growth and Treatment Response in a Murine Model of Glioma

By

David Andrew Hormuth, II

Dissertation
Submitted to the Faculty of the
Graduate School of Vanderbilt University
in partial fulfillment of the requirements
for the degree of
DOCTOR OF PHILOSOPHY
in
Biomedical Engineering
May, 2016
Nashville, Tennessee

Approved:
Thomas E. Yankeelov, Ph.D.
Michael I. Miga, Ph.D.
John C. Gore, Ph.D.
Vito Quaranta, M.D.
C. Chad Quarles, Ph.D.

To my bride

ACKNOWLEDGEMENTS

I would like to thank my Ph.D. advisor, Thomas Yankeelov, for his guidance and expertise throughout my dissertation project and my development as a scientist. I would also like to thank Tom for providing some levity during my dissertation through his sense of humor and for reminding me that "there's always money in the banana stand" and that "I've (not) made a huge mistake". I would also like to thank my committee members, Professors John Gore, Michael Miga, Vito Quaranta, and Chad Quarles for providing valuable insight and dedicating time to advising me on this work.

I would also like to thank all my colleagues at the VUIIS who have helped shape this project through feedback and discussions at our annual retreat and cancer imaging group seminars. Specifically, I would like to thank John Gore and all the other members of the VUIIS for creating a great institute that fosters collaboration and a wonderful place for the training of imaging scientists. Additionally, I would like to thank current and former members of Tom's group, the cancer imaging group, the multiscale modeling group, my MCN B01014 office mates, and everyone on the small animal imaging floor. I would like to specifically thank those who helped get me started on my imaging experiments (Jack Skinner, Danny Colvin, Jennifer Whisenant) and my computational experiments (Jared Weis, Stephanie Barnes, Nkiruka Atuegwu).

I would like to acknowledge and thank the sources of funding for this project: the National Institutes of Health for funding through NCI R01CA138599, NCI R21CA169387, NCI U01CA174706, NCI R25CA092043, the Vanderbilt-Ingram Cancer Center Support Grant NIH P30CA68485, the Kleberg Foundation for the generous support of our institute's imaging program. This work was also partially supported by a pilot project from the Physical Sciences in Oncology

Center at the H. Lee Moffitt Cancer Center and Research Institute (PIs: Robert Gatenby, M.D., Robert Gillies, Ph.D.).

Finally, I would like to acknowledge and thank my family, my friends, and my 12th South community group for encouraging me through my project and supporting Jamie and I here in Nashville. I would like to thank my parents for setting me on a path for a career in science and encouraging me through this project. I would also like to thank my sister for our frequent Google chats. I also would like to thank my son, Theo, for all of our cheerful walks into daycare/work, laughs and chases in the evening, and for unplugging or turning off my computer only a couple times. Most importantly, I would like to thank my wife, Jamie Hormuth, for being my companion, partner in parenting, and supporting me (and listening to science-y things) throughout this dissertation, graduate school, and everywhere else.

TABLE OF CONTENTS

Page

Page

LIST OF TABLES

LIST OF FIGURES

Figure Page

Figure Page

CHAPTER 1

INTRODUCTION

1.1 Motivation

The National Cancer Institute estimated that during the year 2015 nearly 23,000 people in the U.S. were diagnosed with brain or other nervous system cancers [1]. The most common malignant brain tumor is glioblastoma, which are highly aggressive and invasive and have a median survival of 12-15 months. Patients are typically evaluated using magnetic resonance imaging (MRI) to diagnose suspected brain tumors. Patients are initially treated with surgical resection followed by radiotherapy concomitantly with temozolomide [2]. Response to chemo-radiotherapy, however, is often varied due to heterogeneity in inter- and intra-tumor radiosensitivity [3,4]. Unfortunately, nearly all glioblastoma patients exhibit disease progression around 7 to 10 months and will begin treatment for the recurring tumor. Treatment for recurring tumors are often individualized as no current treatment options for recurring tumor have clearly shown improved survival for the entire patient population. The non-uniformity of patient response to both their initial and subsequent treatment options demonstrates a need to improve overall patient care and understanding of an individual's disease.

One promising direction for improving the clinical care of cancer, in general, and glioblastomas, in particular, is the development of individualized mathematical models of tumor

growth. Through the use of non-invasive imaging data, mathematical models can be parameterized by the unique characteristics of an individual's tumor to provide a "forecast" of future tumor growth and treatment response. Prior to the start of treatment, these individualized tumor forecasts could be used by clinicians to evaluate several treatment options and then select the treatment that most benefits the individual. A similar approach can be applied to optimize an individual's radiation therapy dose distribution and treatment frequency to maximize damage to tumor tissue and spare healthy tissue. Individual tumor forecasts could also be used after the start of therapy to predict response or time to progression to help guide future treatment. Using an individualized mathematical tumor model to inform clinical decisions before and after the start of treatment have the potential to transform the clinical care of glioblastoma.

1.2 Specific Aims

Mathematical models of tumor growth typically incorporate parameters that are measured by highly invasive methods or within idealized (*in vitro*) systems. Non-invasive imaging methods, particularly magnetic resonance imaging (MRI) and positron emission tomography (PET), can now provide quantitative and 3D characterizations of, for example, tumor vessel blood flow, permeability, cellularity, hypoxia, metabolism, and cell proliferation. These measureables can be incorporated into realistic biophysical models that can potentially be used to predict tumor growth and (ultimately) therapy response on an individual basis.

The overall goal of this dissertation is to develop models of *in vivo* glioma growth that are initialized, constrained, and validated by noninvasive, quantitative imaging data (in particular, diffusion-weighted MRI (DW-MRI), and contrast enhanced MRI (CE-MRI)). To achieve this goal we have identified the following three specific aims:

Aim 1: Develop the means to accurately estimate model parameters within the standard reaction diffusion equation and evaluate the accuracy of the model in predicting *in vivo* tumor growth. First, we will determine, *in silico*, the measurement strategies required to accurately estimate model parameters and test how accurately these parameters can be used to predict future growth. We then will perform the analogous studies *in vivo* where quantitative DW-MRI will be used to provide estimates of cell number in rats with C6 gliomas. Tumor regions will be identified using CE-MRI. Parameters for the reaction diffusion equation will then be estimated from changes in serial DW-MRI data and used to predict future tumor growth. The accuracy of the predictions that are observed in the *in silico* and *in vivo* datasets will then be compared. We hypothesize that the standard reaction diffusion equation will accurately predict the bulk tumor morphology, but poorly describe the *in vivo* intra-tumoral heterogeneity (e.g., voxel cell number).

Aim 2: Develop a model that accurately captures bulk tumor growth and intra-tumor cellularity. The reaction diffusion equation will be coupled with mechanical properties of surrounding brain and tumor tissue to more accurately describe *in vivo* glioma growth. The mechanical properties of the surrounding brain tissue influence both the overall glioma expansion rate (tumor volume) and the direction of tumor growth (morphology). Voxel-wise heterogeneity

will be introduced through the inclusion of a voxel-specific carrying capacity. Rats with C6 gliomas will be imaged with DW-MRI and CE-MRI. Cell number will be estimated using DW-MRI in tumor regions identified in CE-MRI data. Model parameters will then be estimated from the serial DW-MRI data. The predicted tumor growth will be compared to the *in vivo* tumor growth. We hypothesize that the modified reaction diffusion equation will more accurately describe tumor morphology and voxel cell number compared to the unmodified equation.

Aim 3: Develop a subject-specific model incorporating the effects of whole brain radiation therapy. Imaging data will be obtained from rats with C6 gliomas receiving whole brain radiation therapy. The cytotoxic effects will then be incorporated into the model developed in Aim 2, altering the tumor cell growth characteristics. Cell number will be estimated using DW-MRI in tumor regions identified in CE-MRI data. The cytotoxic effects will be estimated from serial cell number maps. The observed treatment response will be compared to the predicted treatment response. We hypothesize that this model driven by imaging data obtained before and after treatment will accurately predict the distribution of tumor cells at the conclusion of treatment.

1.3 Significance

Mathematical models of cancer have been developed to describe tumor growth and invasion over a large range of spatial scales (nm to cm) and temporal scales (ns to years). Such models can be used to test hypotheses, guide experimental design, and predict future tumor growth [5,6]. Although there exists a large and ever expanding field of models characterizing tumor

growth, there currently is a paucity of models that are translatable to clinical application. In particular, mathematical models that could be specialized to the individual patient to provide accurate descriptions of tumor growth and response to therapy would be a powerful tool for clinicians to select and guide patient therapy. However, there are several fundamental challenges that hinder the translation of mathematical models to clinical care including the selection of a model that is sufficiently complex to answer clinical questions while remaining computationally feasible, the parameterization of models on an individual basis, and the validation of model predictions to experimental measurements or clinical outcomes. This Dissertation aims to develop parsimonious models that can: 1) describe both bulk tumor growth and cellularity changes at the local level, 2) be readily parameterized through subject-specific measurements, and 3) are validated (or refuted) by *in vivo* measurements.

The simplest predictive mathematical models (e.g., exponential growth) describe the change in a single property (e.g., tumor volume) [7,8] as a function of a single parameter (e.g., growth rate). A benefit of these models is that they can be parameterized readily from experimental data and be used to predict future tumor growth [8,9]. Of course, reducing tumor growth to a single property results in a loss of tumor specific details related to (for example) cell density, vascular density, proliferation rates, and the level of response (or lack thereof) of cells to treatment that is observed within tumors [10,11]. Furthermore, such models are not capable of characterizing spatial variations in these parameters. Incorporating additional model terms may more accurately describe the inter- and intra-tumor variation of (for example) cell density, vascular density,

proliferation rate, and response (or resistance) of cells to treatment providing a more complete description of tumor growth. These more complex models of tumor growth, however, often incorporate parameters (e.g., chemotaxis sensitivity coefficients, production rate of growth factors, oxygen or glucose gradients, growth factor gradients) that are measured by highly invasive methods (e.g., surgery biopsy, or animal sacrifice) or within idealized (*in vitro*) systems [12–15]. While measuring these parameters *in vivo* and in 3D at a single time point is extremely difficult, measuring these quantities serially with reasonable spatial and temporal resolution in animal or clinical studies becomes impracticable and highly disruptive. The reliance of existing mathematical models on these parameters that are either extraordinarily difficult or impossible to measure non-invasively fundamentally limits their application for making individualized predictions of future tumor growth based on patient data.

We have proposed that models incorporating parameters that are measureable only through invasive methods could be altered to incorporate non-invasive measurements from medical imaging systems [16]. MRI and PET can be used to provide non-invasive measurements, in 3D and at multiple time points, of quantities relevant to tumor growth. More specifically, MRI and PET can provide measurements of cellularity, blood volume, blood flow, hypoxia, oxygen saturation, and metabolism [17,18]. The discretization of imaging measurements into sub-volumes (voxels) lends itself naturally to the application of mathematical models. Furthermore, the ability to make repeatable, non-invasive, spatially discretized, quantitative measurements of tumor growth supports the development, testing, and refinement of mathematical models resulting in a

more accurate description of tumor growth. Reformulation of mathematical models of cancer to incorporate measurements readily available from imaging data will enable these models to be used for individualized tumor growth predictions.

Several groups have incorporated imaging measurements into mathematical models of tumor growth [9,16,19–27]. Recent work in both breast [19] and pancreatic [20] cancers, have shown that models initialized and constrained with patient data can be used to accurately predict bulk tumor growth. Although a majority of the literature has focused on primary brain cancers, it has not been demonstrated how accurately these models predict bulk tumor growth or intra-tumor properties. There are several approaches for modeling glioma growth that use imaging data to estimate parameters (D = tumor cell diffusion coefficient, k = tumor cell proliferation rate) from the reaction diffusion equation. None of these approaches, however, uses D and k estimated from patient data to predict future tumor growth and then validate that prediction to an *in vivo* measurement. For example, the work of Swanson *et al* has focused on estimating patient-specific growth kinetics to evaluate the efficacy of a prescribed treatment option in terms of survival time [22] or "days gained" [23]. This work has not shown, however, how accurately their model predicts the shape, size, and cellular distribution within the tumor. Alternatively, the work of Clatz *et al* [28] and Bondaiu *et al* [29] have shown that a reaction diffusion based model can accurately describe tumor growth shape and size, but it has not been shown how well it can predict future tumor growth. The development and validation of these models will lead to a better understanding of the limitations and the possibilities of translating mathematical models to clinical application.

1.4 Innovation

Mathematical modeling of cancer is a growing field that is beginning to shift from developing models that study fundamental growth characteristics of tumors to models that are applied to inform clinical decisions. The overarching innovation of this Dissertation is at the center of this transition by developing an experimental and modeling framework in which imaging measurements acquired before and after the start of therapy can be used to inform a mathematical model describing the spatio-temporal evolution of an individual's tumor. More specifically, the innovation of this work is threefold. Firstly, we will develop models of tumor growth at the pre-clinical level providing a more controlled setting to develop, test, and refine tumor growth models. Secondly, we will develop a set of models describing tumor growth in the absence and presence of treatment that can be readily parameterized through non-invasive imaging. Thirdly, we will validate or refute model descriptions directly to *in vivo* measurements obtained from a cohort of rats with C6 gliomas.

Subject-specific models are commonly developed at the clinical level where they may be hampered by a limited number of patient measurements for model parameterization and validation. Using a murine model of glioma allows a more controlled environment to develop, test, and refine tumor growth models to most accurately describe the observed tumor growth. This experimental and modeling framework allows for more frequent observation of tumor growth, investigation of a wider array of imaging measurements, the availability of histology at the conclusion of the study, and a potentially larger cohort of subjects than what is typically available in the clinical setting.

Furthermore, more experimental control allows a more rigorous analysis of both model parameter estimation and tumor growth predictions. For example, more control in the number and frequency of imaging measurements allows us to test the effect of data sampling on the accuracy of estimated parameters. Additionally, the frequent observation of tumor growth allows the accuracy of predicted tumor growths to be compared to *in vivo* measurements at several future time points. This framework is a key component in the development and validation of novel tumor growth models.

The foundation of the models developed within this work is a reaction diffusion model of glioma growth. The first Aim focuses on the development of a framework to accurately estimate model parameters from the reaction diffusion equation and predict future tumor growth. The improvement of this model over existing implementations is the incorporation of a spatially varying proliferation rate allowing spatially heterogeneous tumor growth. Additionally, the first Aim evaluates the accuracy and precision of model predictions with an *in silico* tumor and a cohort of *in vivo* tumors. The second Aim will improve upon the methods developed in the first Aim by developing and evaluating a set of biophysical models aimed at improving the description of bulk and local tumor growth. The third Aim will incorporate the therapeutic effects of single fraction whole brain radiotherapy to predict response to treatment. Critically, all of these models will be validated by comparing predicted tumor growth to imaging measurements of *in vivo* tumor growth. With an accurate model of tumor growth, quantitative MRI and/or PET measurements made before and shortly after the initiation of therapy could be used in a model of tumor growth to help guide

clinical care. For example, accurate characterizations of an individual patient's tumor could allow clinicians to prepare the optimal treatment strategy (e.g., surgery planning, radiotherapy planning, chemotherapy dose and schedule, identifying biopsy targets) or pre-emptively identify treatment failure. At its best, the standard-of-care radiographic measurements [30–32] provide delayed assessment of cellular and tissue response while, at its worse, these measurements are unable to distinguish recurring tumor tissue from non-tumor tissue inflammation. Patient-specific modeling may help the clinical care shift from simple volumetric assessments of tumor growth to a more complete assessment of a patient's current and future status.

1.5 Outline

In this dissertation, a description of the development of predictive biophysical models for tumor growth and treatment response is given. Chapter 1 provides the motivation and specific aims for this investigation. Chapter 2 provides background information regarding cancer imaging, radiation therapy, and mathematical modeling of cancer. Chapter 3 focuses on the development of the means to accurately estimate model parameters from *in vivo* imaging data and an assessment of the accuracy of predictions made with the standard reaction diffusion model. Chapter 4 evaluates prediction accuracy of three novel mathematical models aimed to address the limitations of the standard reaction diffusion model. In Chapter 5, three novel models of response to radiotherapy are developed and evaluated. Finally, Chapter 6 summarizes the major results and discusses the limitations and future directions for this work.

CHAPTER 2

BACKGROUND

2.1 Cancer Imaging

Medical imaging has a critical role in the screening, diagnosing, and care of cancer. Before the detection of cancer, people who are at an increased risk to develop particular cancers (e.g., breast cancer, lung cancer) can be screened using medical imaging data (e.g., mammography [33], low-dose computed tomography [34]) to detect suspicious areas that may be cancerous. After the detection of suspicious areas, medical imaging modalities such as magnetic resonance imaging (MRI), positron emission tomography (PET), ultrasound, computed tomography (CT) are used to determine 1) the location of the tumor, 2) the size of the tumor, and 3) if the tumor has spread to help diagnosis or stage a cancer [2,35–38] and guide biopsies [39–41]. Once diagnosed, medical imaging also plays a crucial role guiding or planning cancer treatments such as surgery [42,43], ablation [44–46], or radiotherapy [47–49] with the goal of removing or targeting as much as the cancer tissue as possible while sparing healthy tissue. Additionally, medical imaging is used to determine if the patient is responding to their treatment by monitoring changes in tumor size [30,50–52] and monitoring functional or environmental changes in the tumor (e.g., standardized uptake value of glucose [18], *apparent* diffusion coefficient [53,54], perfusion [55,56]). After the

conclusion of therapy, medical imaging also plays a surveillance role to watch for recurring tumor or new metastases.

The non-invasive nature of medical imaging that makes it a valuable asset in the frequent observation of cancer from the initial detection to post-treatment surveillance also makes it well suited for integration into mathematical models. More specifically, imaging measurements from MRI, CT, and PET can provide quantitative measurements in 3D of properties relevant to tumor growth. For example, mathematical modeling can utilize this quantitative, temporally and spatially sampled data to provide both anatomical information (e.g., tumor size, tissue location, blood vessel location and size) and physiological information (e.g., metabolism, perfusion) to characterize tumor growth. MRI methods using contrast agents, such as dynamic contrast enhanced MRI (DCE-MRI) [56] and dynamic contrast susceptibility MRI (DSC-MRI) [56], can provide estimates of plasma volume, extracellular-extravascular space, and perfusion, which could be used to estimate the delivery of pharmaceutical agents. Alternatively, models characterizing tumor metabolism could incorporate measurements from ^{18}F-Fludeoxyglucose (FDG-PET) which measures glucose uptake. The models within this dissertation utilize MRI data to identify tissue structures, identify tumor tissue, and estimate tumor cellularity.

Different anatomical regions within the brain (white and gray matter) can be identified from signal contrast in T_1 maps. In MRI, T_1 is a rate that characterizes the return of the net magnetic moment to equilibrium (also known as longitudinal relaxation). In one T_1 approximately 63% of the bulk magnetization has returned to equilibrium. Longitudinal relaxation is strongly dependent

on physical composition of the tissue resulting in T_1 values that vary from tissue to tissue. For example, in a study at 4.7 T T_1 maps can provide contrast between white matter, gray matter, and CSF [57]. T_1 can be altered in cancerous tissues due to changes in water content (e.g., inflammation or edema), macromolecular content, pO_2, and pH [58]. Tissue T_1 can also be decreased using a paramagnetic contrast agent such as gadolinium-diethylenetriamine pentaacetic acid (Gd-DTPA) and observed using a method called contrast-enhanced MRI (CE-MRI). When placed within a magnetic field the Gd ion creates a strong local magnetic field, due to its unpaired electrons, which alters the magnetic field experienced by water protons in its vicinity. The net effect of the altered magnetic field is a shortened T_1 for the water protons. The relaxation experienced by the water protons is highly dependent on the distance to the Gd center. Water protons can also have a transient contact interaction with the unpaired electrons, also reducing T_1. To avoid toxicity, Gd ions are chelated to DTPA amongst others [59]. It should be noted that chelation can also result in a diminished effect of Gd ions on water protons due to increased separation between the two elements. As tumors typically have leaky blood vessels [60], Gd-DTPA can escape the vasculature and accumulate in the extravascular space resulting in shortened T_1 values within this region. T_1-weighted images acquired after the injection of Gd-DTPA typically show increased signal in tumor regions compared to images acquired before injection of the contrast agent. Panels (a-b) in Figure 2.1 shows an example of the increased signal intensity (blue region of interest in panel (b)) that can be observed in tumor regions following the injection of Gd-DTPA. Panel (c) in Figure 2.1

shows the decreased T_1 that is observed in tumor tissue (blue line), while healthy tissue T_1 remains relatively constant (red line).

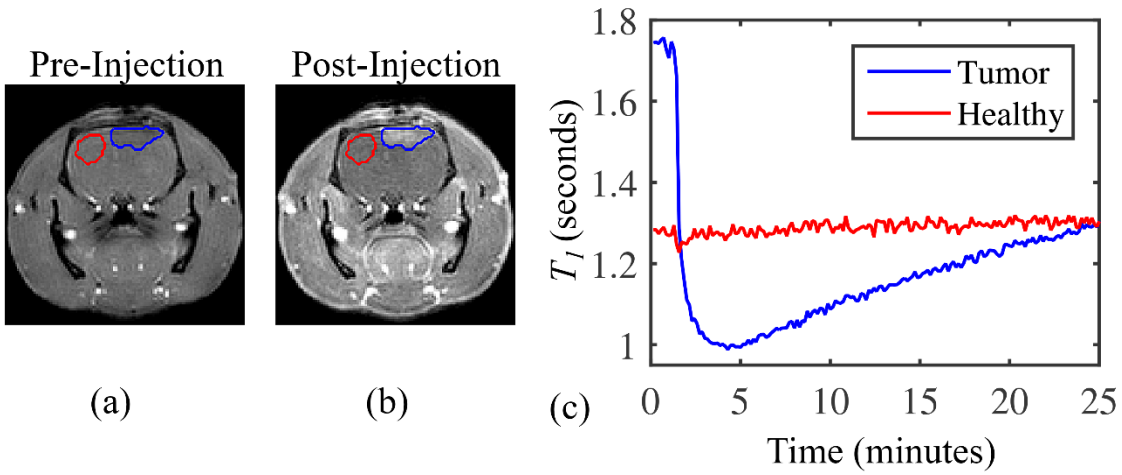

Figure 2.1. Pre-and post-injection T_1 weighted MRI. Panels (a) and (b) show the central tumor slice of a rat with a brain tumor before and after the injection of a contrast agent. The red outline represents healthy brain tissue, while the blue outline represents tumor tissue. The tumor tissue is hyper-intense (panel (b)) following the injection of the contrast agent. Panel (c) shows the dynamic change of tissue T_1 in the same regions of interest from panels (a-b) following the injection of the contrast agent. Tumor T_1 (blue line) decreases from ~1.8 seconds to ~1 second following the injection of the contrast agent.

There are, however, several limitations to using CE-MRI for identifying tumor tissue in post-treatment cases. The main limitation is that it relies on the presence of leaky vasculature within the tumor. A decrease in leaky vasculature could occur during anti-angiogenic therapies that can normalize the vasculature [61]. This vascular normalization is the result of inhibition of VEGF that prunes immature vessels and normalizes the remaining vessels resulting in a false indication of volume reduction [62] . Radiotherapy can also alter CE-MRI interpretations by

falsely indicating a volume increase [62]. Pseudoprogression as observed post-radiotherapy is typically due to increased inflammation, edema, and vessel permeability in the tumor and surrounding tissue and is challenging to distinguish from actual progression.

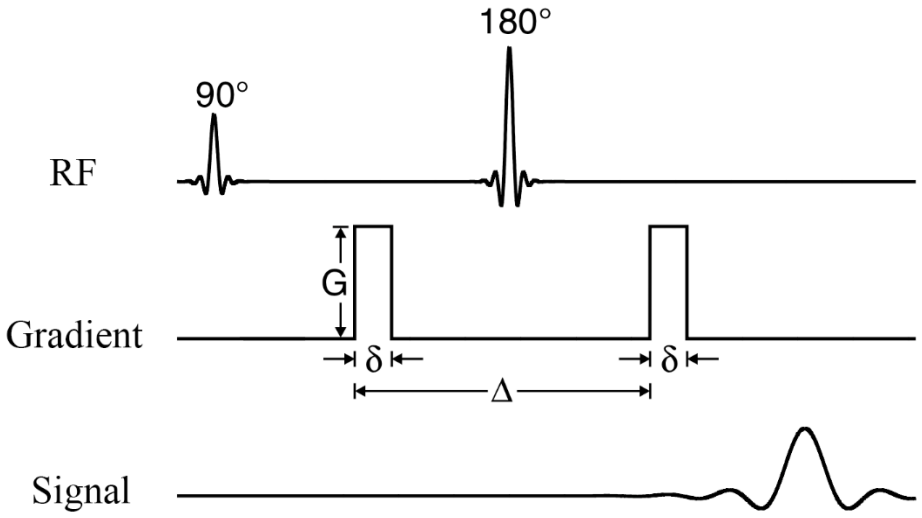

Figure 2.2. Pulse sequence diagram for a pulsed gradient spin-echo experiment. The top line depicts the excitation (90°) and refocusing (180°) radiofrequency pulses (RF). The diffusion gradient is shown in the middle line. The diffusion gradients are separated from by time Δ and have an amplitude of G and duration of δ. If spins move during time Δ, they will have a net phase that is related to the distance they have moved along the direction of the gradient. The final line represents the signal.

Tumor cellularity can be estimated by calculating the *apparent* diffusion coefficient (ADC) from diffusion-weighted MRI (DW-MRI) data [63]. DW-MRI is an imaging method that is sensitive to the diffusion of water within tissue. A commonly used diffusion-weighted sequence is the pulsed gradient spin-echo, Figure 2.2, which uses gradients applied before and after the 180° refocusing pulse to label spins within the tissue. Briefly, an initial gradient of amplitude G, duration

δ, applied along (for example) the *x*-axis, is used to add phase (ϕ) to spins that varies with its position along the *x*-axis ($\phi_1 \propto \gamma \cdot G \cdot x_1 \cdot \delta$, ϕ_1 is the initial phase shift, γ is the gyromagnetic ratio, and x_1 is the initial position along the x-axis). The 180° refocusing pulse then reverses this phase (i.e., $\phi_1 = -\phi_1$). A second gradient of equal amplitude and duration, is applied after a time Δ resulting in a second phase shift ($\phi_2 \propto \gamma \cdot G \cdot x_2 \cdot \delta$, ϕ_2 is the second phase shift, and x_2 is the position along the *x*-axis at the during the second gradient). The net phase shift is then the sum of ϕ_1 and ϕ_2, shown in Eq. (2.1):

$$\phi_2 - \phi_1 \propto \gamma \cdot G \cdot \delta \cdot (x_2 - x_1) \ . \tag{2.1}$$

During time Δ molecules continue to move by random motion potentially resulting in a displacement along the direction of the gradient (*x*-axis). The probability of a spin having this net phase can be described using a Gaussian distribution with a mean net phase equal to zero, and a standard deviation shown in Eq. (2.2):

$$\left\langle \left(\phi_{net}\right)^2 \right\rangle \propto \gamma^2 \cdot G^2 \cdot \delta^2 \cdot (x_{net})^2 \ , \tag{2.2}$$

where ϕ_{net} is the net phase and $\left(x_{net}\right)^2$ is the mean square displacement along the *x*-axis. For random Brownian motion [64], the mean square displacement can be written in terms of the diffusion coefficient (*D*) of the moving molecules, Eq. (2.3):

$$\left\langle \left(\phi_{net}\right)^2 \right\rangle \propto \gamma^2 \cdot G^2 \cdot \delta^2 \cdot (2 \cdot D \cdot \Delta) \ . \tag{2.3}$$

The end effect on this phase displacement on the MR signal (S) is an attenuation of the intrinsic signal S_0, shown in Eq. (2.4):

$$S = S_0 \cdot e^{-\gamma^2 \cdot G^2 \cdot \delta^2 \cdot (2 \cdot D \cdot \Delta)} \quad . \tag{2.4}$$

By altering G, δ, and/or Δ different levels of signal attenuation can be obtained for a given sample which can then be used to estimate S_0 and D.

In tissue, the diffusion of water molecules is often lower than free water due to restrictions to free movement. This reduced diffusion coefficient is called the *apparent* diffusion coefficient, or ADC. In tissue, the ADC can be effected by cell density, cell membrane permeability, cell size, and tissue tortuosity. For example, as cell density and/or cell size increase the ADC typically decreases as there are more barriers to free water movement. Several groups [65–69] have observed an inverse relationship between ADC and cellularity (cells per area or cells per volume). A notable example is from Sugahara *et al* [68] who observed a strong correlation ($r = 0.77$, $p = 0.007$) of ADC with histology estimated cell density in glioma patients. Studies in extracranial lesions ($r = 0.73$, $p < 0.001$, [69]), breast cancer ($r = 0.54$, $p < 0.01$, [67]), and pre-clinical models of breast cancer ($r > 0.57$, $p = 0.03$, [65]) have also shown have also shown correlation between ADC and cell density. However, ADC can also increase as a result of increased cell membrane permeability allowing water to move more freely between intra- and extra-cellular spaces. In the study by Latour *et al* [70] they observed that an increase in cell membrane permeability of erythrocytes could also result in an increase in the effective diffusion coefficient. A third influence

on changes in ADC is the tortuosity of the tissue which as tissue tortuosity decreases water molecules need to make fewer turns to travel through the tissue. A study by van der Toorn *et al* [71] in a murine model of ischemia observed both an increase in tortuosity and a decrease in ADC following cardiac arrest.

In this dissertation we utilize a simple linear relationship between ADC and cell number to provide non-invasive estimates of cell number [9,19,63,72–74] using Eq. (2.5):

$$ADC(\bar{x}) = -\left(\frac{ADC_w - ADC_{min}}{\theta}\right) N(\bar{x}) + ADC_w, \tag{2.5}$$

where $ADC(\bar{x})$ is the measured ADC at position $\bar{x}$, ADC_w is the ADC of free water, ADC_{min} is the minimum ADC which we assume corresponds to the voxel with the largest number of cells, θ is the maximum number of cells an imaging voxel can support, and $N(\bar{x})$ is the number of cells at position $\bar{x}$. Eq. (2.5) can be re-arranged to estimate $N(\bar{x})$ directly from ADC measurements using Eq. (2.6):

$$N(\bar{x}) = \theta\left(\frac{ADC_w - ADC(\bar{x})}{ADC_w - ADC_{min}}\right). \tag{2.6}$$

There are, however, several limitations to directly relating ADC to cell number. One limitation is that we assume all changes in ADC are only related to changes in tissue cellularity, while in reality the origin of changes in the ADC can be ambiguous. For example, an increase in cellularity would result in a decrease in ADC, but a decrease in ADC may be the result of an increase in cellularity

or an increase in cell size or a decrease in membrane permeability. In cancer, several or all of these phenomena may change as the tumor grows or receives treatment. A second limitation is that the standard ADC measurement approach is insensitive the different contributions to the ADC. The standard pulsed gradient spin-echo is insensitive to different size of restrictions (e.g., cell size) and to changes in individual contributions (e.g., changes in permeability versus cellularity, extracellular versus intracellular diffusion). Alternative ADC measurement methods (e.g., oscillating gradient spin-echo [75]) or diffusion models (e.g., bi-exponential diffusion) may allow for identification of different contributions to the ADC. To the first order, however, the standard pulse gradient spin-echo estimate of the ADC can provide a non-invasive measurement of cellularity [65–69] that correlates well with histology estimates of extracellular volume and cellularity.

2.2 Radiation Therapy

2.2.1 Ionizing Radiations Effect on Cell Death

Ionizing radiation primarily damages DNA, although recent research suggests lower-dose radiotherapy may primarily target the cell membrane or cytoplasm [76]. While every molecule within the cell is exposed to ionizing radiation, damage to DNA is significantly impacted compared to other molecules as it has only two copies, is infrequently duplicated, and critical to all cellular [77]. The outcome of the damage incurred by ionizing radiation is determined by the DNA damage

response (DDR). The DDR is responsible for the detection of damage and the signaling of response pathways leading to cell death, DNA repair, temporary blocks in the cell-cycle, or permanent blocks in the cell-cycle. Irradiation induced cell death occurs primarily after the cell attempts to divide, although cells can also die prior to mitosis (due to apoptosis activated by the DDR mechanism) or not at all [78]. Post-mitotic cell death may occur after attempting to divide at least once and results in apoptosis, autophagy, necrosis, or senescence. Prior to post-mitotic cell death cells can continue to proliferate for several generations before a mitotic catastrophe occurs.

As there is typically a delay in cell death following radiation exposure, cell survival is typically quantified by performing a clonogenic assay. Clonogenic assays assess the proliferative ability of a group of cells by counting the number of colonies formed per cells plated (also known as their plating efficiency). Cell survivability is then estimated as the ratio of the plating efficiency of the treated to the untreated cells. The clonogenic assays are then repeated at several radiation doses to generate a cell survival plot.

For stochastic interactions, the probability of the number of interactions can be described using Poisson statistics, Eq. (2.7) :

$$P(n) = \frac{e^{-D} \cdot D^{n}}{n!} \ , \tag{2.7}$$

where $P(n)$ is the probability of n interactions, and D is radiation dose. If a single interaction is assumed to result in cell death, the probability of survival (or not being hit) is simply $P(0) = e^{-D}$. For viruses, bacteria, and very sensitive human cells Eq. (2.7) is an appropriate model of survival

[79]. However, in other tissues cell survival is non-stochastic due to repair mechanisms and is often characterized at low doses using a linear-quadratic (LQ) model [79,80], Eq. (2.8):

$$P(survival) = e^{-\alpha D - \beta D^2} \tag{2.8}$$

where α and β are radiosensitivity parameters, and D is dose. α and β have units of Gy^{-1} and Gy^{-2}, respectively, while D is reported in units of Gy. (A Gy or gray is the SI unit of ionizing radiation dose defined as the absorption of one joule of radiation energy per one kilogram of matter.) One potential biological interpretation of Eq. (2.8) is the lethal-potentially lethal damage model [81]. The LPL models posits that the linear portion of the LQ model are cells that receive non-repairable lethal lesions after a single hit (dose), while the quadratic portions is representative of repairable lesions that may eventually die to subsequent lesions or misrepair. Figure 2.3 shows simulated cell survival curves using Eq. (2.7) and Eq. (2.8). As β approaches zero, the LQ model approaches the Poisson model of cell survival.

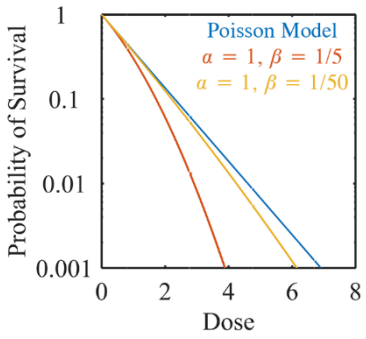

Figure 2.3. Cell survival curves for Poisson and LQ model. The probability of survival (vertical axis) is plotted against the dose of radiation (horizontal axis) for the Poisson model (blue line), the LQ model with α equal to 1 and β equal to 1/5 (orange line), and the LQ model with α equal to 1 and β equal to 1/50 (yellow line).

The LQ model is typically used by researchers and clinicians to characterize the radiosensitivity of different tissues with two simple parameters (α and β). Balancing the effects of radiation on different tissues (i.e., tumor and healthy tissues) is a critical consideration in the design of radiotherapy. As healthy and tumor tissues can often have different ratios of α and β, radiotherapy is typically given at low doses over several sessions to minimize damage to healthy tissue. Low-dose (less than 2 Gy) fractionated radiotherapy also takes advantage of several biological processes that occur between sessions improving patient outcome [82]. One process is that fractionated therapy allows healthy tissues to repair DNA damage between sessions while tumor tissues (which have a slower repair rate) are further damaged at subsequent sessions. A second process is the redistribution of cells throughout the cell cycle allowing cells that were less sensitive in the initial session (those in DNA synthesis stage) to move into a more responsive stage of the cell cycle. A similar redistribution occurs in hypoxic tumors where following radiotherapy normoxic cells are preferentially targeted resulting in more oxygen for the remaining (predominately) hypoxic cells [83]. Some of these remaining hypoxic cells become normoxic and are more sensitive to future radiotherapy sessions. A fourth biological advantage of radiotherapy is the repopulation (or rapid proliferation) that can occur following treatment resulting in a larger fraction of cells in sensitive stages of the cell cycle. Although, it should be noted that repopulation may also negatively affect treatment outcome [84,85].

2.2.2 Radiotherapy's Role in Glioblastoma Care

Radiotherapy is part of the standard-of-care for over 50% of all cancers [86]. For example, in glioblastoma multiforme patients, radiotherapy is typically applied post-resection as a means to target the residual infiltrative cancer tissue [87] and has been shown to increase median survival from 3.1 months (no radiotherapy or chemotherapy) to over 8 months [87,88]. Glioblastoma patients typically receive a radiotherapy dose of 60 Gy over 30 fractions [2]. This has primarily been performed using whole brain radiotherapy [87] or conformal radiotherapy, however developments of more focal methods (i.e., intensity modulated radiotherapy [89,90], stereotactic radiosurgery [91,92]) are increasingly preferred. More focal methods allow for healthy tissues to receive reduced doses potentially sparing side effects, such as neurocognitive defects, swelling, nausea, fatigue, vision problems, and hearing problems. One study by Hermanto *et* [89] noted that intensity modulated radiotherapy resulted in a 19-40% reduction in mean exposure in the brain stem, optic chiasm, and optic nerves compared to the standard of care. One shortcoming of focal approaches is that it may insufficiently expose infiltrative tumor, this can be improved when combined with whole brain radiotherapy [91]. However, no conclusive survival benefit has been observed for combined whole brain radiotherapy and focal approaches beyond reduction in adverse neurocognitive outcomes and late adverse effects [91].

Currently MRI, CT, and PET play an important role in the planning of target volumes (or dose distribution) for conformal radiotherapy, intensity modulated radiotherapy, and stereotactic radiosurgery [47]. The target volumes, shown in Figure 2.4, consists of the gross tumor volume

(GTV), clinical tumor volume (CTV), and planning target volume (PTV) [93]. The target volumes are typically assigned from MRI data sets [94]. The GTV is defined as the T_2 or FLAIR abnormality with a dose boost to the T_1 post-contrast enhancing region. The CTV includes the GTV plus a margin (~ 2 cm) for undetectable disease. The PTV includes the CTV plus a safety margin (~0.5 to 1 cm) to account for variations in setup and reproducibility. Once calculated, these target volumes are used for all radiotherapy sessions and are not altered as the tumor cells respond or resist the therapy. Current radiotherapy research is investigating ways to reduce the ambiguity

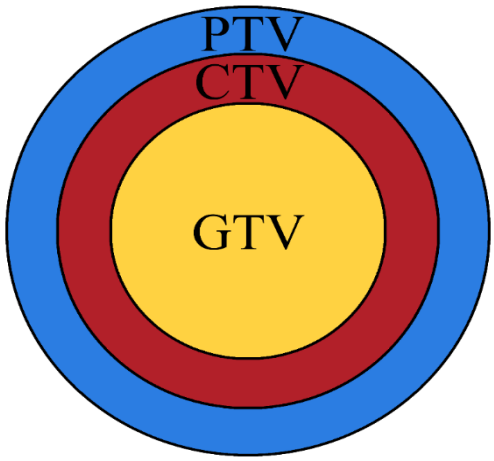

Figure 2.4. Target tumor volumes used for planning radiotherapy. The gross tumor volume (GTV) represents the detectable tumor as observed in T_2-weighted or T_1-weighted MRI and receives the highest dose. The clinical tumor volume (CTV) includes the GTV and represents the undetectable spread of the tumor. The largest volume, the planning target volume (PTV), includes the CTV and GTV with an additional margin to account for errors in daily set-up and reproducibility of dose distribution.

in CTV margins and overall reduce toxicity to healthy tissue. Mathematical modeling could potentially improve radiotherapy design by designating target volumes based on functional or physiological information rather than image identified tumor volumes. This approach would allow for individualized radiotherapy plans that incorporates tumor radiobiology to determine the optimal radiotherapy plans.

2.3 Cancer Models

2.3.1 Observation Driven Mathematical Modeling

There is an extensive mathematical modeling literature aimed at describing the spatio-temporal growth patterns exhibited by tumors. Mathematical models can provide the framework on which to test hypotheses *in silico* or to guide future *in vitro* or *in vivo* experimental design (e.g., limit search space for experiments). Early models of cancer growth focused on developing models that recapitulated *in vivo* observations of changes in volume or cell count. In particular, observations that a tumor's growth rate decreases over time [95,96] led to several early models [97,98] including the logistic model which is often the foundation of more complex models. The logistic model, Eq. (2.9), describes the change in tumor volume (V) as a function of a proliferation coefficient (a) and a carrying capacity (K):

$$\frac{dV}{dt} = aV\left(1-\frac{V}{K}\right), \tag{2.9}$$

when V is much less than K, the volumetric growth is nearly exponential; however, when V approaches K, volumetric growth slows and then ceases when V is equal to K. A recent paper by Benzekry *et al* [98] evaluated the logistic and eight other classic volumetric growth models for their ability to accurately describe and predict tumor volume measurements. The logistic model had the best model fit to breast cancer time courses, while the exponential-linear model had the highest prediction success rate. These classical models of growth generally provide accurate descriptions of bulk tumor growth (i.e., tumor volume) making them a critical starting point for the development of models characterizing other tumor properties.

Mathematical models that describe more biologically complex phenomena (i.e., tumor invasion, angiogenesis, cellular metabolism) than volumetric growth are often characterized by discrete [12,99–101], continuum [19,26,73,74,102], and hybrid discrete-continuum models [103,104]. Discrete models [12,99,100], can provide representations of individual elements (e.g., tumor cells, healthy cells, immune cells) whose status is updated using biological rules. The biological rules can, for example, decide if a cell will divide, migrate, or die [12,99] based on a cell's microenvironment. Conditions for cellular decisions such as oxygen or glucose concentration can be based off of experimental measurements. One such model from Piotrowska *et al* [99], calculates glucose concentration, oxygen concentration, and pH at each site of a lattice to determine whether a cell will die, survive through quiescence (with aerobic or anaerobic metabolism), or survive through proliferation (with aerobic or anaerobic metabolism). The authors note, that while their model can recapitulate experimentally observed growth kinetics and areas of

necrosis, additional model terms are needed to predict the onset of necrosis. This model and other discrete models can generally capture intra-tumor growth patterns observed *in vivo* (i.e., proliferating rim and the necrotic or apoptotic core [105,106]), but are computationally challenging to apply to larger scale problems. The computational demand for discrete models increases as the number of elements increase typically limiting its use to smaller scale applications.

Continuum models [19,26,73,74,102] describe tumors as a continuous field rather than a set of individual cells. At larger scales where the relevant unit of space supports millions of cells it is computationally easier to describe model elements and variables as continuous fields using (typically) partial differential equations (PDEs). Continuum models can provide characterizations of gross tumor properties but do not provide characterization of individual cellular dynamics. This limitation can be addressed using hybrid discrete-continuum models [103] which typically use continuum models to characterize nutrient concentration, and use discrete models to characterize tumor cell [12,107] or endothelial cell [15] interactions. One common continuum model is a reaction diffusion model, Eq. (2.10), used to describe the proliferation (reaction) and movement (diffusion) of cells or nutrients [12,13,19,26,74,102,103,108–110]. A standard reaction diffusion model utilizing a logistic model of proliferation is shown in Eq. (2.9):

$$\frac{\partial N(\bar{x},t)}{\partial t} = \nabla \bullet \left(D \cdot \nabla N(\bar{x},t) \right) + k \cdot N(\bar{x},t) \left(1 - \frac{N(\bar{x},t)}{\theta} \right), \tag{2.10}$$

where $N(\bar{x},t)$ is the number of tumor cells at three-dimensional position $\bar{x}$ and time t, D is the tumor cell diffusion coefficient, k is the net tumor cell proliferation, and θ is the tumor cell carrying

capacity. A benefit of this model is that very few parameters are needed to describe the proliferation and invasion of tumor cells in 3D, most of which can be estimated from experimental measurements. One application by Gatenby *et al* [108] models normal tissue, tumor tissue, and excess H^+ ion concentration as a set of three coupled reaction diffusion models. In this coupled model the amount of tumor tissue is directly related to the production of H^+ ion concentration. As the tumor tissue grows and increases the H^+ ion concentration, the normal tissue begins to die. The death of the normal tissue then makes it possible for tumor tissue to invade into surrounding normal tissue. Other applications of reaction diffusion type models have been used to model tumor cell consumption of nutrients (oxygen and glucose concentration [12,13]), tumor-induced angiogenesis (endothelial cells and matrix degrading enzymes [15], and tumor-pattern formation [111,112]).

2.3.2 Clinically Oriented Mathematical Models

Currently, the field of cancer mathematical modeling is developing a new generation of predictive models aimed at informing clinical care [16]. A current challenge, however, is that existing mathematical models often have parameters that are difficult or impossible to assess non-invasively on a patient-specific basis. This challenge requires the development of novel mathematical models, or the selection and reformulation of existing models, to include parameters that are readily measureable on an individual. Models intended for clinical applications need to answer the relevant clinical questions and be parameterized through non-invasive measurements. While a 1D model may provide accurate predictions of future tumor volume, a 2D or 3D model

may also inform clinicians on the direction growth, areas of increased proliferation, or areas of increased resistance or response.

One common model that is being investigated for clinical application is the reaction diffusion model [19,20,24,26,28,29,73,74,102,110,113]. Early work by Swanson *et al* [102] used clinical ranges of tumor doubling times and serial computed tomography (CT) observations of the velocity of tumor margin progression, v_{margin}, to estimate tumor cell diffusion, D, and proliferation, k, from the standard reaction diffusion model. With an estimated value of k and v_{margin} the Fisher's approximation can be used to determine the random walk diffusion coefficient, $D \approx v_{margin}^2/4k$. Based on observations that the tumor advanced in white matter much faster than gray matter two separate values of D were calculated, where $D_{white\ matter} = 5 \times D_{gray\ matter}$. In this preliminary work, the authors report that the simulated tumors visually agreed with clinically observed tumor geometries. Later work by Swanson *et al* [114–116] replaced CT data with serial T_1-weighted and T_2-weighted MRI to provide estimates of both the "visible" (i.e., enhancing tumor in T_1-weighted post-contrast images) and "invisible" (i.e., hyper-intense tumor in T_2-weighted images) tumor margins. The authors reported that an individual's k ($P = 0.03$) was significantly related to prognosis, while the ratio of k to D was a predictor of survival ($P = 0.01$) [116].

Work by Jbabdi *et al* [24] expanded upon the standard reaction diffusion model by describing D as a diffusion tensor estimated from diffusion tensor imaging MRI data enabling modeling of anisotropic diffusion of tumor cells. Simulated tumors "seeded" and "grown" within a healthy brain were able to qualitatively match the tumor anisotropy observed in clinical cases,

indicating the importance of incorporating structural information of the brain into the modeling description. Similarly, Ellingson *et al* [25] used serial diffusion-weighted MRI to provide spatially varying estimates of D and k to create cell invasion, motility, and proliferation level estimate (CIMPLE) maps. These "CIMPLE" maps showed strong correlation (R^2 = 0.97) to magnetic resonance spectroscopy measurements of the choline to N-acetylaspartate ratio and could be used to differentiate WHO grade II, III, and IV tumors. An alternative approach to incorporating tissue structure is by coupling a reaction diffusion model to a biomechanical model of tissue stress [26,28,109]. These approaches allow mechanical properties to be assigned to different regions of the brain (identified through image segmentation) to calculate tissue stress and deformation as a result of the tumor growth. The calculated tissue stress and deformation can be used to temporally and spatially reduce the tumor cell diffusion coefficient [109], displace tumor cells [26,110], or displace the underlying tissue structure to alter tumor growth kinetics [28,29].

The reaction diffusion model has also been applied to patients treated with surgical resections [22], chemotherapy [19,73,117], and radiotherapy [23,117–120]. The effects of treatment can be incorporated explicitly through new model terms (such as death to radiation exposure [120] or drug concentration [117]) or implicitly through the estimation of model parameters [19,73]. One approach to modeling the effects of radiotherapy in brain by Rockne *et al* [120] adds a new term to the standard reaction diffusion model (i.e., Eq. (2.8)) accounting for the loss of cells (R) due to radiotherapy:

$$R\left(\alpha, d(x,t)\right) = 1 - e^{-\alpha \cdot n \cdot d(x,t) \cdot \left(1 + d(x,t)/(\alpha/\beta)\right)}\ , \tag{2.11}$$

Eq. (2.11) describes the lethality of the radiotherapy in terms of radiosensitivity parameters (α and β), number of radiotherapy fractions (n), and dose at position x and time t, $d(x,t)$. In [120] the ratio of α to β was held constant at 10 Gy and n and d are provided by the radiotherapy plan; thus, the approach requires the estimation or measurement of only one parameter (α). Rockne *et al* demonstrated a model framework through which different therapy schedules and distributions can be tested for a patient's individual radiosensitivity. A follow up investigation of this model in nine glioblastoma multiforma patients [119] was used to estimate a patient's individual radiosensitivity parameter (α) using two pre-treatment MRIs (to estimate untreated growth kinetics) and one post-treatment MRI (to estimate treatment effect). The estimated α strongly correlated with the pre-treatment k (r = 0.89. p = 0.0007). This current implementation, however, is limited to describing the efficacy of treatment after the completion of a radiotherapy course. That is, it cannot assess early in a patient's treatment the efficacy of treatment or be used to alter the future radiotherapy schedule based on a patient's radiosensitivity. Badoual *et al* [121] expanded upon Rockne *et al*'s initial model [120] by incorporating a model of edema that recapitulated observations of a post-radiotherapy growth delay. The authors observed that a high k correlated with low progression-free survival agreement with clinical data and suggested that this model could provide early assessment of response during radiotherapy treatments.

Biophysical models of glioma growth have also expanded beyond assessing a patient's radiosensitivity and have begun investigating optimized treatment plans [122–124]. Corwin *et al*

[122,123] used the model developed in [120] to test biologically optimized radiation therapy plans *in silico*. The optimal radiotherapy plan was selected when exposure to normal brain tissue was minimized and the number of viable tumor cells post-treatment was minimized. These biologically optimized plans were then compared to the standard of care plan. The *in silico* comparison resulted in a 67-93% decrease in normal tissue dose and a 50-265% increase in treatment efficacy. An alternative approach by Bondiau *et al* [124] used model predicted invasion to evaluate the appropriateness standard CTV margins. The model predicted that the standard margins (2 cm) produced a treatment volume where greater than 53% of the volume was healthy brain. Additionally, it was observed that the standard margins excluded up to 15% of the invasive tumor. This work suggested that mathematical modeling could reduce ambiguity in assigning CTV margins on a patient-specific basis. The work of Corwin and Bondiau *et al* demonstrate the potential value modeling has to clinical radiation therapy. However, the efficacy of individualized radiotherapy plans still need to be validated with *in vivo* experiments. Development and evaluation of individualized models at the pre-clinical level may potentially validate relevance of individualized radiotherapy plans.

The development of the above, more clinically oriented, mathematical models have relied primarily on medical imaging to provide the data necessary to estimate parameters on an individual basis. Parameterization of models with medical imaging data increases the translatability of these models to clinical application. While the clinically oriented mathematical models discussed within this chapter show promising results, there still remains a lack of validated model that have

demonstrated the accuracy and precision of tumor growth predictions. In this dissertation, we aim to address this lack of validated models by 1) developing the means to use MRI data to parameterize tumor growth models on an individual basis, 2) use the image driven tumor models to simulate (or predict) future tumor growth, and 3) validate tumor growth predictions directly to *in vivo* measurements. In Aims 1 and 2, we focus on the development of accurate and precise models of untreated glioma growth. We first will evaluate the accuracy and precision of tumor growth predictions made using the standard reaction diffusion model. We then will expand upon the standard reaction diffusion model to better characterize bulk tumor growth and cell number distribution. Finally, in Aim 3 we will incorporate the effects of radiotherapy on cell death and proliferation.

CHAPTER 3

PREDICTING *IN VIVO* GLIOMA GROWTH WITH THE REACTION DIFFUSION EQUATION CONSTRAINED BY QUANTITATIVE MAGNETIC RESONANCE IMAGING DATA

Aim 1: Develop the means to accurately estimate model parameters within the standard reaction diffusion equation and evaluate the accuracy of the model in predicting *in vivo* tumor growth.

Text for Chapter 3 adapted from:

Hormuth DA, Weis JA, Barnes SL, Miga MI, Rericha EC, Quaranta V, Yankeelov TE. "Predicting in vivo glioma growth with the reaction diffusion equation constrained by quantitative magnetic resonance imaging data". *Physical Biology*. 2015; 12(4)

3.1 Introduction and Contribution of Study

This study centered on evaluating the ability of the standard reaction diffusion model to predict future *in vivo* glioma growth. While the reaction diffusion model is widely used to describe tumor growth, it is not well known how accurate it can predict *in vivo* tumor growth. This study evaluated the accuracy of tumor growth predictions made using subject-specific model parameters. This was achieved by first performing *in silico* experiments to develop the means to accurately estimate model parameters. The *in silico* study demonstrated that model parameters can be accurately and precisely estimated from measurements acquired at three different time points, and then used to accurately predict future tumor growth. The methods developed for the *in silico* case

were then applied to an *in vivo* data set to assess how accurate the standard reaction diffusion model can predict *in vivo* glioma growth.

This work contributed to the literature the characterization of both the parameter estimation and model prediction approaches needed to accurately predict *in vivo* tumor growth. The developed methods demonstrated that the reaction diffusion model can be used to accurately predict future tumor growth—provided that the tumor's biology is actually described by the reaction diffusion model. Furthermore, this study demonstrated that the standard reaction diffusion model poorly predicts *in vivo* C6 glioma growth and that the model would need to be revised to obtain accurate predictions. As the standard reaction diffusion model is often the common foundation of tumor growth models [26,102,108], the characterization of the reaction diffusion model would aid in the development of the tumor models discussed in Chapters 4 and 5. This work was published in *Physical Biology* in June 2015.

3.2 Abstract

Reaction diffusion models have been widely used to model glioma growth. However, it has not been shown how accurate this model can predict future tumor status using model parameters (i.e., tumor cell diffusion and proliferation) estimated from quantitative *in vivo* imaging data. Towards this end, we used *in silico* studies to develop the methods needed to accurately estimate tumor specific reaction diffusion model parameters, and then tested the accuracy with which these parameters can predict future growth. The analogous study was then performed in a

murine model of glioma growth. The parameter estimation approach was tested using an *in silico* tumor "grown" for ten days as dictated by the reaction diffusion equation. Parameters were estimated from early time points and used to predict subsequent growth. Prediction accuracy was assessed at global (total volume and Dice value) and local (concordance correlation coefficient, CCC) levels. Guided by the *in silico* study, rats (n = 9) with C6 gliomas, imaged with diffusion weighted magnetic resonance imaging (DW-MRI), were used to evaluate the model's accuracy for predicting *in vivo* tumor growth. The *in silico* study resulted in low global (tumor volume error < 8.8 %, Dice > 0.92) and local (CCC values > 0.80) level errors for predictions up to six days into the future. The *in vivo* study showed higher global (tumor volume error > 11.7%, Dice < 0.81) and higher local (CCC < 0.33) level errors over the same time period. The *in silico* study shows that model parameters can be accurately estimated and used to accurately predict future tumor growth at both the global and local scale. However, the poor predictive accuracy in the experimental study suggests the reaction diffusion equation is an incomplete description of *in vivo* C6 glioma biology and may require further modeling of intra-tumor interactions including segmentation of (for example) proliferative and necrotic regions.

3.3 Introduction

Mathematical models have been constructed to describe tumor growth and invasion over a large range of spatial scales (nm to cm) and temporal scales (ns to years). Substantial discussions have focused on translating these models to clinical care with the long term goal of providing

clinicians with patient-specific predictions of future tumor growth and therapy response in order to optimally select and guide patient therapy [16,125,126]. Approaches for patient-specific predictions may focus on changes in a single property such as tumor volume, or changes in tumor growth as a function of several related properties (e.g., cellularity, vascularity, nutrient distribution). Models that focus on the change in a single tumor property can be parameterized readily with experimental data [8,9], but may fail to capture spatial and temporal tumor heterogeneity of, for example, cellularity, vasculature density, proliferation rates, and the level of response (or lack thereof) of cells to treatment that is observed within tumors [10,11]. Patient-specific models that capture a tumor's spatial and temporal heterogeneity could be used to more accurately describe the delivery of treatment and subsequent response [127–130]. Unfortunately, modeling these characteristics frequently requires knowledge of parameters that can only be measured by highly invasive methods or within idealized (*in vitro*) settings [12–15]. The reliance of the existing modeling literature on parameters that are either extraordinarily difficult or impossible to measure non-invasively fundamentally limits their clinical application. Recasting these models in terms of parameters measured *via* non-invasive imaging measurements would dramatically improve the clinical relevance of patient-specific tumor growth predictions [16].

Magnetic resonance imaging (MRI) and positron emission tomography (PET) can be used to provide an array of non-invasive, quantitative, and functional measurements in 3D and at multiple time points of tumor growth. More specifically, MRI and PET can provide measurements of cellularity [53], blood volume [56,131], blood flow [56,131], hypoxia [132], oxygen saturation

[133], and metabolism [18]. Additionally, the ability to make repeatable, non-invasive, spatially discretized, quantitative measurements of tumor growth supports the development, testing, and refinement of mathematical descriptions of *in vivo* tumor growth. Several groups [9,16,19,20,22–26,63] have incorporated imaging measurements from MRI, PET, and x-ray computed tomography into mathematical models of tumor growth. Preliminary efforts in both breast [19] and pancreatic [20] cancers, have shown that patient specific imaging data can potentially accurately predict future tumor growth. This, however, has not been demonstrated for gliomas.

One common model for glioma growth is the reaction diffusion model, whereby the spatio-temporal change in tumor cellularity is due to proliferation and invasion (described by random diffusion) of tumor cells. The proliferation and invasion of cells are typically characterized with a proliferation rate and a diffusion coefficient, respectively. The reaction diffusion model of glioma growth described by Swanson *et al* [22], uses proliferation and diffusion coefficients of tumor cells estimated from T_2-weighted and post-contrast T_1-weighted MRI data obtained at two time points. The estimated tumor cell proliferation and diffusion values can then be used to simulate tumor growth following surgical resection [22] or simulate a virtual control to assess patient response to radiotherapy [23]. Jbadbi *et al* [24] extended this approach by allowing anisotropic diffusion of tumor cells by replacing the diffusion coefficient with a diffusion tensor measured using diffusion tensor imaging (DTI). The authors showed that simulated anisotropic tumor growth better matched the shape of glioma growth observed in patients. Spatially varying estimates of diffusion and proliferation were included in the work of Ellingson *et al* [25]. In this

work, serial diffusion weighted MR images were used to develop a voxel-wise analytical solution (when certain assumptions are satisfied) to a reaction diffusion model of glioma growth. The proliferation and diffusion values were compared to MR spectroscopy measurements, but these values were not used to simulate tumor growth. Another extension of the reaction diffusion model is the incorporation of mechanical properties of healthy and tumor tissue into a description of tumor growth [19,20,26,109]. The work of Hogea *et al* [26] showed the benefit of incorporating mechanical deformations caused by the invading tumor growth into a reaction diffusion model. Their effort also demonstrated the means to invert their model system to estimate parameters from imaging data.

In this work we use a reaction diffusion model of glioma growth with proliferation and diffusion values estimated from quantitative *in vivo* imaging data to predict future tumor growth and then validate (or refute) that prediction by direct comparison to future *in vivo* measurements. Using an *in silico* tumor we first developed the means to accurately estimate model parameters and assessed the accuracy of tumor growth predictions. We then performed the analogous *in vivo* study, where model parameters were estimated from serial diffusion-weighted MRI data in a murine model of glioma to predict future tumor status which could then be directly compared to experimental outcome. The *in silico* experiments show that model parameters can be accurately estimated from tumor growth datasets and then used to predict future tumor growth with low global and local errors. However, when the approach is applied to *in vivo* glioma measurements, it is shown that the reaction diffusion model provides poor predictive ability of future tumor growth.

3.4 Materials and Methods

3.4.1 Modeling Approach

The reaction diffusion equation describes the spatio-temporal rate of change in tumor cell number and distribution due to the random movement of tumor cells (diffusion; the first term on the right hand side of Eq. (3.1)), and proliferation (reaction; the second term on the right hand side of Eq. (3.1)):

$$\frac{\partial N(\bar{x},t)}{\partial t} = \nabla \bullet \left(D(\bar{x}) \nabla N(\bar{x},t) \right) + k(\bar{x}) N(\bar{x},t) \left(1 - \frac{N(\bar{x},t)}{\theta} \right), \tag{3.1}$$

where $N(\bar{x},t)$ is the number of tumor cells at three-dimensional position $\bar{x}$ and time *t*, $D(\bar{x})$ is the tumor cell diffusion coefficient at position $\bar{x}$, $k(\bar{x})$ is the net tumor cell proliferation at position $\bar{x}$, and θ is the tumor cell carrying capacity. Note that the proliferation term varies temporally as a function of cell density, $N(\bar{x},t)$, although it is assumed that the proliferation rate, $k(\bar{x})$, is temporally constant. As described below, quantitative DW-MRI provides estimates of $N(\bar{x},t)$. These data are obtained at multiple time points, early in the tumor's life cycle, and used to solve an inverse problem using Eq. (3.1) to return estimates of $k(\bar{x})$ for each voxel within the tumor, and two $D(\bar{x})$ values: one for white matter (D_{wm}) and one for gray matter (D_{gm}). The forward evaluation of Eq. (3.1) is solved using a three dimension in space, fully explicit finite difference (FD) in time simulation written in Matlab (Mathworks, Natick, MA). The simulation domain has no diffusive flux of tumor cells at brain tissue boundaries (i.e., at the skull) and the

grid spacing matches the spatial resolution of the MRI data (Δx = 250 μm, Δy = 250 μm, Δz = 1000 μm). The simulation time step was set at 0.01 days. (Appendix A provides further details on the finite difference implementation of Eq. (3.1).)

3.4.2 In Silico Experiments

Figures 3.1 and 3.2 show the approach for the *in silico* experiments. An initial distribution of tumor cells, $N(\bar{x},t_0)$, was seeded within a rat brain domain. A spatial map of k was determined from DW-MRI estimates of $N(\bar{x},t)$ from a C6 glioma bearing rat using Eq. (3.2):

$$k(\bar{x}) = -\log\left(N(\bar{x},t_1)/N(\bar{x},t_0)\right)/(t_1 - t_0)\ , \tag{3.2}$$

Where $N(\bar{x},t_0)$ and $N(\bar{x},t_1)$ represent the distribution of cells at time t_0 and t_1, respectively, while $k(\bar{x})$ remained constant in time. The initial model parameters, or P_{true} (P = (k(1), k(2),… k(n), D_{gm}, D_{wm}), where n is the number of voxels within the tumor), were selected by iteratively scaling $k(\bar{x})$ until a 12 fold increase in total tumor volume was observed over 10 days, matching the average observed tumor volume increase observed in the *in vivo* study. An FD simulation of Eq. (3.1) with an initial distribution of tumor cells $N(\bar{x},t_0)$ and parameters P_{true} was used to grow an *in silico* tumor for 10 days (1000 time steps/iterations). Tumor cell distributions, $N(\bar{x},t)$, were then sampled at days 0, 2, and 4 thru 10. Panel (a) in Figure 3.1 shows a central anatomical axial slice through a rat head and cropped images of the *in silico* tumor cell distribution seeded at day 0 and "grown" to days 2 and 4. Three different combinations of these three time points were then

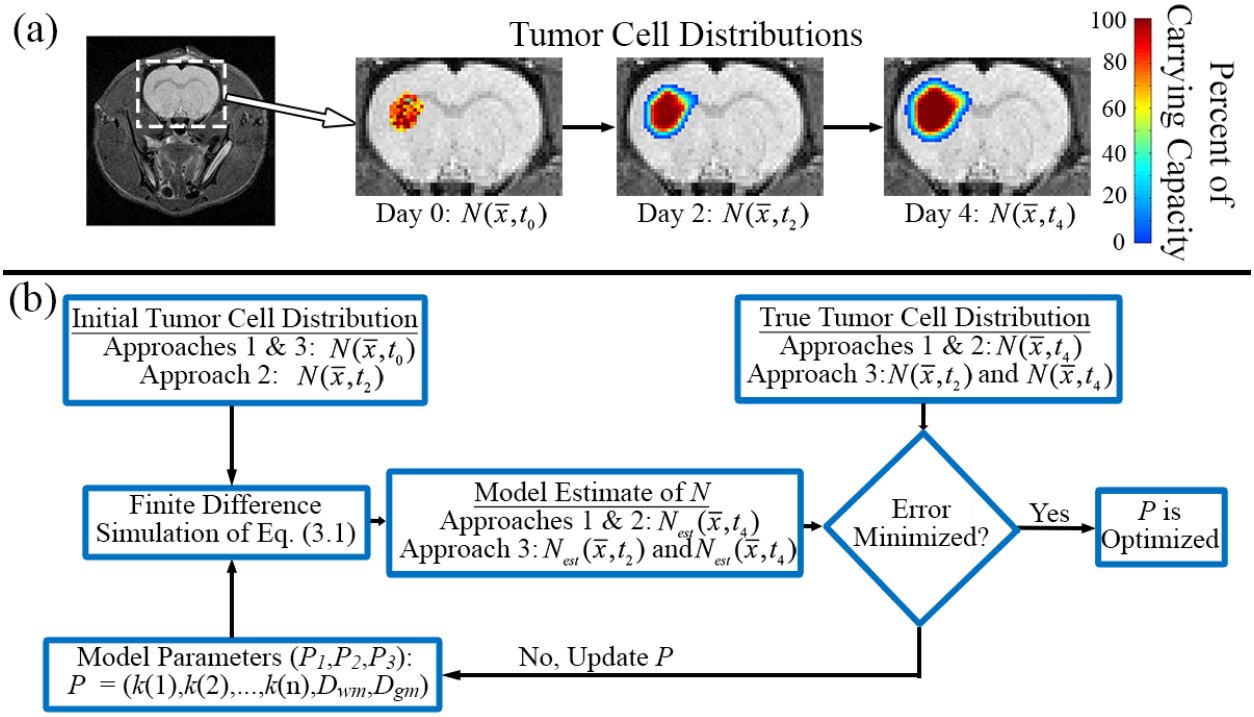

Figure 3.1. Parameter optimization approach. Panel (a) shows a central anatomical axial slice through the rat brain and cropped images of the *in silico* tumor cell distributions at days 0, 2, and 4. Panel (b) shows the model parameter optimization approach used for the *in silico* and *in vivo* studies. The process starts with an initial distribution of tumor cells and an initial guess for P. A finite difference simulation of Eq. (3.1) using the initial P and the initial tumor cell distribution is used to "grow" a model estimate of N for four days. The error between N_{est} at day 4 (or days 2 and 4 for Approach 3) and N is calculated. When the error between N_{est} and N is minimized, parameter optimization ceases and the model parameters are set to the current values of P. However, if the error is not minimized, P is updated and parameter optimization continues.

used to estimate three sets of model parameters (P_1, P_2, and P_3). P_1 was estimated using tumor cell measurements from days 0 and 4 ($N(\bar{x},t_0)$ and $N(\bar{x},t_4)$, respectively). P_2 was estimated using tumor cell measurements from days 2 and 4 ($N(\bar{x},t_2)$ and $N(\bar{x},t_4)$, respectively), while P_3 was estimated using tumor cell measurements from days 0, 2, and 4 ($N(\bar{x},t_0)$, $N(\bar{x},t_2)$, and $N(\bar{x},t_4)$

, respectively). Panel (b) in Figure 3.1 shows the parameter optimization approach for these model parameters (P_1, P_2, and P_3). For each set of estimated parameters (P_1, P_2, and P_3) a FD simulation

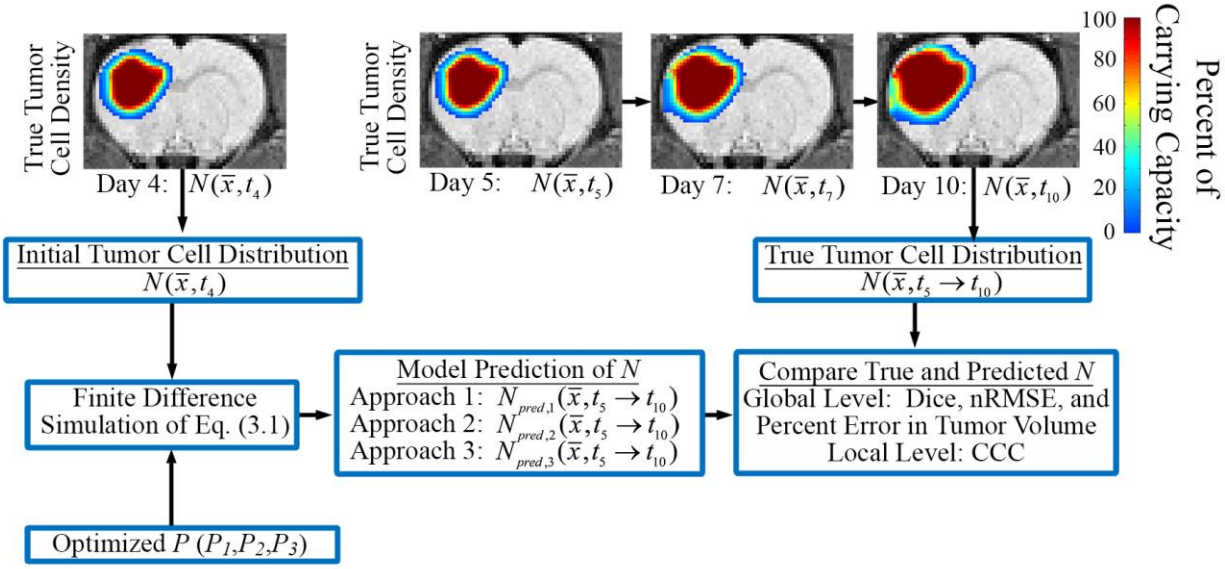

Figure 3.2. Predicted tumor growth modeling approach. This figure shows the modeling approach for predicting future tumor growth for the *in silico* and *in vivo* studies. The tumor growth prediction model is initialized with N from day 4 as well as the optimized parameters P. N at day 4 and P are used in a finite difference simulation of Eq. (3.1) to "grow" the tumor for 6 days resulting in a model prediction of N (i.e., N_{pred}). This modeling approach is repeated for each set of model parameters (P_1, P_2, P_3). The error between N_{pred} and N at days 5 through 10 is calculated at the global level (Dice similarity coefficient, nRMS error, and percent error in tumor volume) and at the local level (CCC).

of Eq. (3.1) was initialized with $N(\bar{x},t_0)$ (for P_1 and P_3) or $N(\bar{x},t_2)$ (for P_2) and used to grow a tumor to day 4 resulting in a model estimate of N for each parameter set ($N_{est,1}$, $N_{est,2}$, and $N_{est,3}$). The error between N and $N_{est,1}$, $N_{est,2}$, and $N_{est,3}$, respectively, was calculated. If this error is

minimized, the optimal values of P_1, P_2, and P_3 have been determined, otherwise P_1, P_2, and P_3 are updated with new values. The optimized P values are then used to predict future tumor growth.

Figure 3.2 shows the modeling approach for predicting future tumor cell distributions. In the following text and figures, the notation $t_a \rightarrow t_c$ is used to indicate time points t_a, t_c, and all time points between t_a and t_c. For each set of optimized parameters (P_1, P_2, and P_3) an FD simulation of Eq. (3.1) was used to "grow" the tumor from day 4 to day 10 (6 days; 600 iterations) resulting in predicted tumor cell distributions for each parameter set ($N_{pred,1}\left(\bar{x}, t_5 \rightarrow t_{10}\right)$, $N_{pred,2}\left(\bar{x}, t_5 \rightarrow t_{10}\right)$, and $N_{pred,3}\left(\bar{x}, t_5 \rightarrow t_{10}\right)$, respectively). Error between the true N and N_{pred} was calculated at both the global and local levels by calculating the percent error in tumor volume, the Dice similarity coefficient, the normalized root mean square error (nRMS error), and the concordance correlation coefficient (CCC).

3.4.3 In Vivo Experiments

All experimental procedures were approved by Vanderbilt University's Institutional Animal Care and Use Committee. Female Wistar rats (n = 9, 236-263 g) were anesthetized, given analgesics, and inoculated with C6 glioma cells (1×10^5) *via* stereotaxic injection. During each MRI procedure body temperature was maintained near 37° C by a flow of warm air directed over the animal and respiration was monitored using a pneumatic pillow. Each rat was anesthetized using 2% isoflurane in 98% oxygen for all surgical and imaging procedures. Rats were imaged beginning 10 days post-surgery (defined as day 0). Rats were imaged up to 10 days after the first

imaging time point. The first three imaging measurements for all rats occurred on days 0, 2, and 4. Rats 1-3 were then imaged on days 5, 8, and 10. Rats 4-5 were imaged on days 5, 6, and 9. Rat 6 was imaged on days 5, 6, 8 and 10, while rats 7-8 were imaged only on days 5 and 6. Rat 9 was only imaged at one additional time on day 5.

MRI was performed on a 9.4 T horizontal-bore magnet (Agilent, Santa Clara, CA, USA). The animal's head was positioned in a 38 mm diameter Litz quadrature coil (Doty Scientific, Columbia, SC, USA) and was secured by a bite bar. All MR images were sampled with a 128 × 128 × 16 matrix acquired over a 32 × 32 × 16 mm^3 field of view. In order to facilitate the modeling, the imaging volumes obtained at time points two through the end of the experiment were registered to the first time point *via* a mutual information based rigid registration algorithm performed at the scanner [134]; this ensures that the image volumes obtained at each time point are very nearly identical (See Figures B.1-B.3 for example registration results in the appendix). T_1 map was produced using data from an inversion-recovery snapshot experiment with *TR*/*TE* = 5000/3 ms, *TI* (inversion time) = (8 *TIs* logarithmically spaced between 200 - 4000 ms), and two averaged excitations.

DW-MRI was acquired using a pulsed fast spin echo diffusion sequence in three orthogonal diffusion encoding directions with *b*-values of 0, 300, 500, 700, 900, and 1100 s/mm^2, and Δ/δ = 25 ms/2 ms. The apparent diffusion coefficient (ADC) was estimated on a voxel basis using a two parameter fit of the DW-MRI data [135]. To determine $N(\bar{x},t)$, the ADC values from the DW-MRI data are then transformed to estimate cell number [66,72] using Eq. (3.3):

$$N(\bar{x},t)=\theta\left(\frac{ADC_w-ADC(\bar{x},t)}{ADC_w-ADC_{min}}\right), \tag{3.3}$$

where θ represents the tumor cell carrying capacity, *ADCw* is the ADC of free water at 37° C (2.5 × 10^{-3} mm^2/s) [135], $ADC(\bar{x},t)$ is the ADC value at position $\bar{x}$ and time *t*, and ADC_{min} is the minimum ADC value which corresponds to the voxel with the largest number of cells. The carrying capacity, θ, was calculated for each imaging voxel assuming spherical tumor cells with a packing density of 0.7405 [136] with an average cell volume of 908 μm^3 [137].

Tumor regions-of-interest (ROI) were manually placed at each time point using the T_1 maps. ADC measurements within these ROI's were then transformed to tumor cell number using Eq. (3.3). T_1 maps were used to define tumor, white, and gray matter regions in the MR images.

Similar to the *in silico* experiments, three sets of model parameters (P_1, P_2, and P_3) were then estimated for each rat. We note that the time and spatial origin of the tumor (as mentioned in Hogea *et al* [26]) was not determined as tumor growth simulations were initialized with tumor cellularity measurements from DW-MRI. The estimated parameters for each rat (parameters for rat 1; $P_{R1,1}$, $P_{R1,2}$, and $P_{R1,3}$) were used in a FD simulation of Eq. (3.1) to "grow" simulated tumors from day 4 to day 10 (6 days; 600 iterations) resulting in predicted tumor cell distributions for each parameter set (predicted $N(\bar{x},t)$ for rat 1; $N_{R1,pred,1}(\bar{x},t_5 \rightarrow t_{10})$, $N_{R1,pred,2}(\bar{x},t_5 \rightarrow t_{10})$, and $N_{R1,pred,3}(\bar{x},t_5 \rightarrow t_{10})$, and, respectively).

The three different time point combinations from the *in vivo* data sets were also fit to a model substituting a spatially invariant proliferation rate (k_{ROI}) for the spatially variant proliferation rate ($k(\bar{x})$); i.e., $k(\bar{x}) \equiv k_{ROI}$ in Eq. (3.1).

3.4.4 Numerical Methods

A Levenberg-Marquardt weighted least squares nonlinear optimization, implemented with a regularization parameter described in Joachimowicz *et al* [138,139], was used to estimate model parameters (P_1, P_2, P_3) from tumor cell distribution measurements. All parameters were constrained to non-negative values. Prior to estimating P a 3 × 3 Gaussian filter was applied to each slice of $N(\bar{x},t)$ to reduce the effects of noise within individual voxels. During the optimization scheme, k was estimated voxel-wise in areas within the tumor ROI and assigned 0 elsewhere. Additionally, D_{wm} and D_{gm} values were assigned region-wise using a white and gray matter map. The optimized parameters were determined when the objective function, Eq. (3.4), was minimized:

$$\sum_{t=t_i}^{t_f}\left(\left(\sum_{\bar{x}=1}^{\bar{x}_i=n}\left(N\left(\bar{x},t\right)\right)\right)^{-1}\cdot\left(\sum_{\bar{x}=1}^{\bar{x}=n}\left(N_{est}\left(\bar{x},t\right)-N\left(\bar{x},t\right)\right)^2\right)\right), \tag{3.4}$$

where t_i is the initial time point, t_f is the final time point, n is the total number of voxels within the tumor, and $N_{est}(\bar{x},t)$ is the model estimate of N using the current parameter set. For P_1 and P_2 optimizations, t_i and t_f were equal to day 4. For P_3 optimization t_i was equal to day 2 and t_f was equal to day 4.

To assess the effect of noise in ADC measurements on estimates of P, *in silico* parameter optimization was repeated (N = 100) for each set of parameters (P_1, P_2, P_3) with noise added to $N(\bar{x},t)$ from a normal distribution with a zero mean and a standard deviation of 3.3% of the carrying capacity (selected based on the reproducibility of ADC measurements *in vivo* [135]).

After optimization of P, these values were used in a FD implementation of Eq. (3.1), initialized with the tumor cell distribution at day 4 ($N(\bar{x}, t_4)$), to "grow" a predicted tumor from day 4 thru 10 (600 iterations). Throughout the FD simulation, as the tumor expanded into regions where an estimate of k was unavailable, k was assigned using a local average of available non-zero k's within a 3 × 3 × 3 kernel.

The accuracy of P estimated from the *in silico* dataset was evaluated by computing the percent error between the true, P_{true}, and the estimated parameter sets (P_1, P_2, and P_3), the Pearson correlation coefficient (PCC), and the CCC (similar to the PCC but with a penalty for data that do not lie on the line of unity) [140]. A Bland-Altman analysis was also performed between the true, P_{true}, and the estimated (P_1, P_2, and P_3) parameter sets. For the *in vivo* study, agreement between P_1, P_2, and P_3 estimates of $k(\bar{x})$ was assessed by calculating the PCC and CCC for P_1 and P_2, P_1 and P_3, and P_2 and P_3. For both the *in vivo* and *in silico* studies error between the predicted and true tumor growth was assessed at the global (i.e., volume) and local (i.e., voxel) levels. For the *in vivo* analysis, the tumor ROIs and measured cellularity from DW-MRI are taken as true tumor growth. At the global level, error was assessed by calculating the percent error in tumor volume, the nRMS error, and the Dice similarity coefficient (a measure of spatial overlap between two data sets ranging from 0 (no overlap) to 1 (complete overlap); [141]). The percent error in tumor volume and nRMS error were computed by comparing the true tumor volume and the tumor volumes predicted from FD simulations using P_1, P_2, and P_3 at days 5 thru 10. The Dice similarity coefficient was computed by comparing the spatial overlap between the true tumor ROIs and the

tumor ROIs predicted from FD simulations using P_1, P_2, and P_3 at days 5 thru 10. At the local level, error was assessed by computing the CCC between N and N_{pred} at days 5 thru 10. For the *in vivo* study, paired t-tests were used to evaluate the differences between percent error in tumor volume, Dice similarity coefficient, and CCC results observed with the spatially variant k and spatially invariant k models.

3.5 Results

3.5.1 In Silico Results

Illustrative results of the *in silico* experiments are shown Figures 3.3 –3.5 and summarized in Table 3.1. Figure 3.3 shows the true distribution of k (panel (a)) used to "grow" the *in silico* tumor, the estimated values of k (panels (b – d)), and plots of the true voxel values of k against the estimated values of k (panels (e – g)). Panels (b) and (e) show the results from parameters estimated from days 0 and 4. Both a low level of agreement (CCC = 0.38) and a weak linear relationship (PCC = 0.54) is observed between the true k and the k estimated using the P_1 data sets (k_{P1}). Additionally 88% of voxels in k_{P1} are overestimated. Parameters estimated using days 2 and 4 (panels (c) and (f)) showed an improved level of agreement (CCC = 0.74), stronger linear relationship (PCC = 0.80), and fewer overestimated voxels (72%) compared to k_{P1}. Using all three time points (panels (d) and (g)) resulted in the best level of agreement (CCC = 0.84), the strongest linear relationship (PCC = 0.87), and the fewest overestimated voxels (58%). Panels (h-j) show

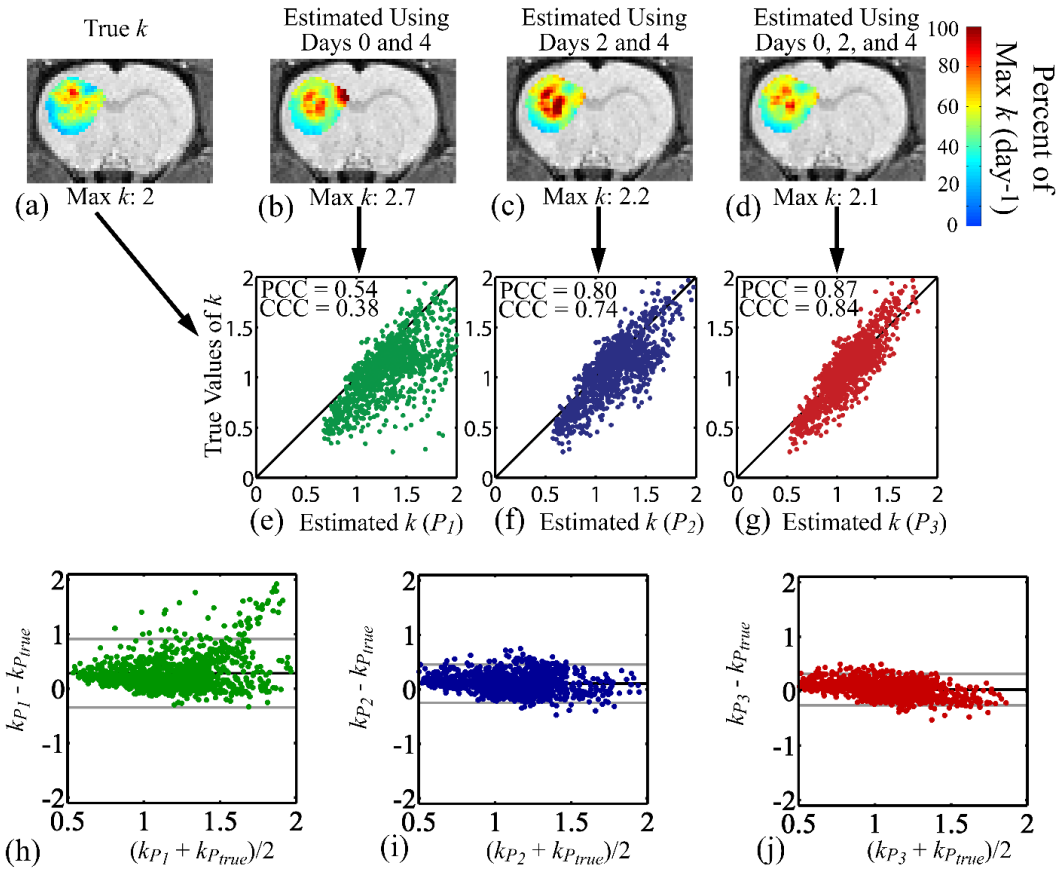

Figure 3.3. True and estimated proliferation rate maps from *in silico* study. The true (panel (a)) and estimated values (panels (b – d)) of *k* are shown for the *in silico* study. Panel (a) shows the true distribution of *k* used to "grow" the *in silico* tumor. Panels (b – e) show example parameter maps of *k* estimated using days 0 and 4 (panel (b)), days 2 and 4 (panel (c)) and days 0, 2, and 4 (panel (d)). Panels (e – g) show the individual voxel values of the true *k* plotted against the estimated values of *k* from P_1, P_2, and P_3. Additionally panels (e – g) show the PCC and CCC values between the true *k* and the estimated *k*. *k* estimated from days 0 and 4 have more voxels that are overestimated resulting in a lower level of agreement (CCC = 0.38) compared to the other two approaches. The highest level of agreement and correlation (CCC = 0.84 and PCC = 0.87) between the estimated and true *k* was observed when days 0, 2, and 4 were used to estimate *k*. Panels (h – j) show the Bland-Altman analysis comparing the k_{P1}, k_{P2}, and k_{P3} to k_{Ptrue}. The black lines represent the mean difference, while the gray lines represent the 95% confidence interval of those means. A lower mean difference was observed for $k_{P3} - k_{Ptrue}$ (0.028) compared to $k_{P1} - k_{Ptrue}$ (0.28) and $k_{P2} - k_{Ptrue}$ (0.11).

the Bland-Altman analysis for P_1, P_2, and P_3 compared to P_{true}. The black lines represent the mean difference while the gray lines represent the 95% confidence interval (CI). A larger 95% CI was observed for $k_{P1} - k_{Ptrue}$ (-0.35 to 0.91) compared to $k_{P2} - k_{Ptrue}$ (-0.25 to 0.46) and $k_{P3} - k_{Ptrue}$ (-0.26 to 0.32).

Figure 3.4 shows the true (panel (a)) and the predicted tumor cell distributions (top rows in panels (b–d)) and the percent difference between the true and predicted distributions (bottom rows in panels (b–d)). Panel (b) shows the predicted N at day 5 using P_1, P_2, and P_3. The highest error between N and N_{pred} at day 5 was observed for parameters P_1 (mean ± standard error; 31.15 ± 0.82%) compared to P_2 (19.67 ± 0.64%) and P_3 (16.84 ± 0.58%). As the tumor continues to grow, increased error is observed between N and N_{pred}. Generally, this error is increased at the periphery (greater than 100% error) relative to the interior (less than 40%). The predicted N at day 8 (panel (c)) resulted in increased mean error relative to day 5 for predictions using P_1 (41.38 ± 0.87%), P_2 (28.03 ± 0.68%) and P_3 (26.03 ± 0.64%). At the final time point (panel (d)), P_3 based predictions had a mean error (29.51 ± 0.65%) lower than P_1 (45.93 ± 0.90%) and P_2 (30.83 ± 0.67%) based predictions. The lowest cumulative error was observed for P_3 based predictions (nRMS error; mean = 0.062, standard error = 1.33×10^{-2}) compared to P_1 based predictions (nRMS error; mean = 0.289, standard error = 2.51×10^{-2}) or P_2 based predictions (nRMS error; mean = 0.102, standard error = 1.19×10^{-2}).

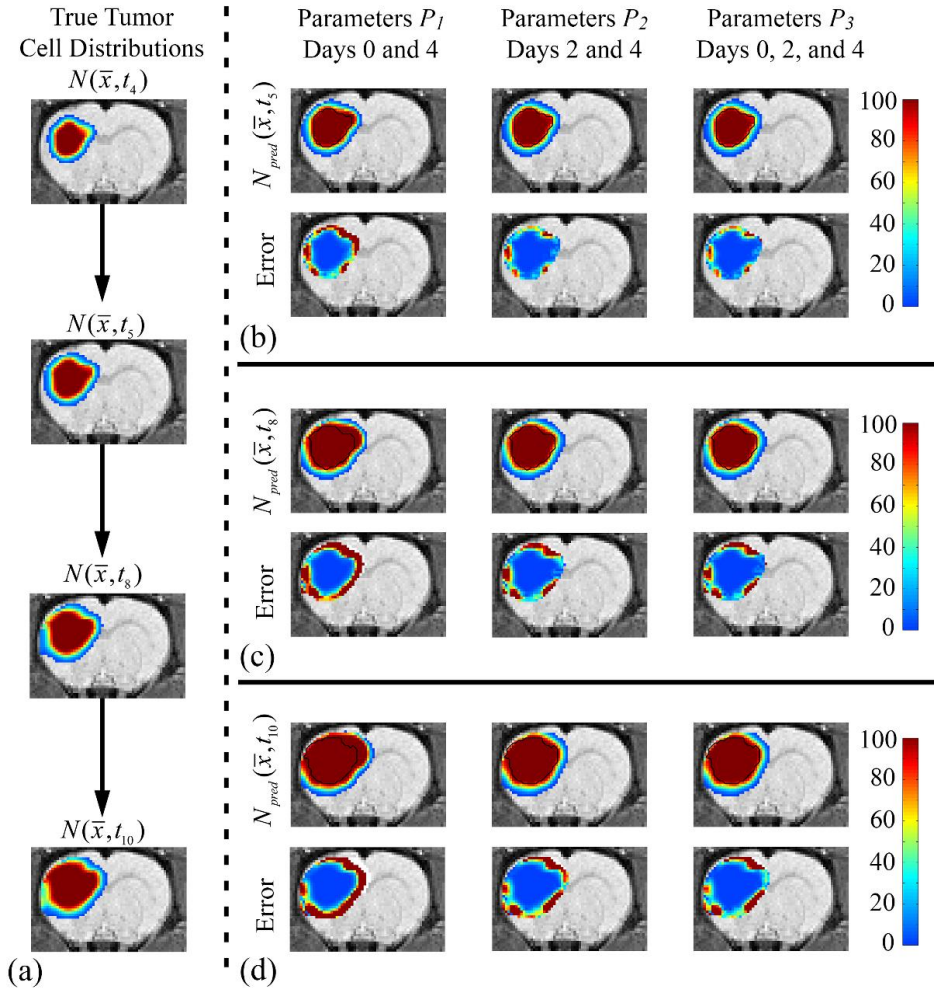

Figure 3.4. True and predicted tumor cell distributions for *in silico* study. The true and predicted tumor cell distributions for the *in silico* study are showed above. Panel (a) shows the true N at the central slice of the tumor volume on days 4, 5, 8, and 10. The predicted N (N_{pred}) and the error between N and N_{pred} for the same slice on days 5, 8, and 10 are shown in panels (b – d). The black outline displayed on N_{pred} in panels (b – d) represent the high cell density region from the true tumor cell distributions in panel (a). The color bars represent percent of the carrying capacity (top rows) and percent error (bottom rows). White regions observed in the percent error maps represent areas where no tumor cells were observed in the true data set. The top rows in panels (b – d) represent N_{pred}, while the bottom row represents the percent difference between N and N_{pred}. Additionally, the three columns in panels (b – d) represent the results using parameters P_1, P_2, and P_3. Increased error (greater than or equal to 100%) is observed at the periphery of the tumor relative to the interior of the tumor (less than 20%).

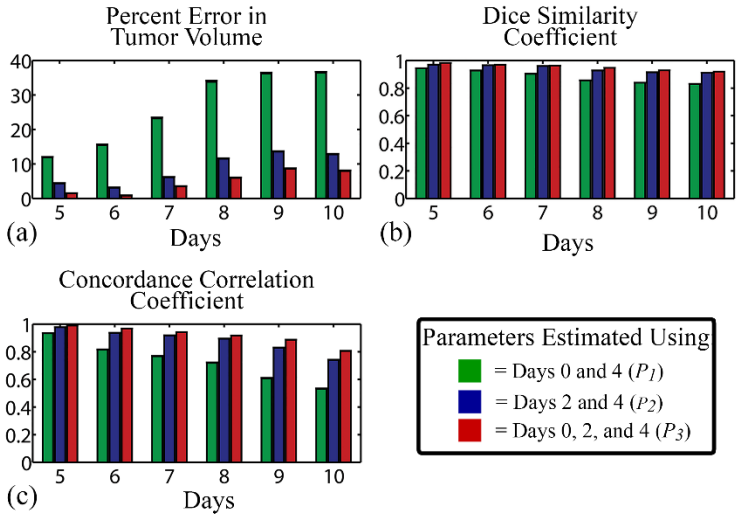

Figure 3.5. Global and local level error analysis for *in silico* study. Panels (a – b) show the result of global level error analysis while panel (c) shows the result of local level error analysis for the in silico experiments. The mean and standard error (N = 100) of each measurement is plotted at days 5 through 10. Panel (a) shows that less than 8.8% error is observed for all predictions when using parameters estimated from days 0, 2, and 4. Standard error in panel (a) is less than 0.32%. The Dice values (panel (b)) show all parameter sets result in a Dice value greater than 0.83. Panel (c), shows a steady decrease in the level of voxel agreement (decrease in CCC) over time for all sets of parameters. At each time point and for each error measurement there are significant differences between values from P_1 and P_2, P_1 and P_3, and P_2 and P_3 ($p \leq 0.05$). The standard error in panels (b) and (c) is less than 3.8×10^{-3}.

The results of the ROI and voxel level analysis are shown in Figure 3.5. Error in tumor volume generally increases the further out in time a prediction is made (panel (a)). Percent error in tumor volume ranged from 11.9 – 36.4% for P_1 based predictions, 3.1 – 13.6% for P_2 based predictions, and 0.8 – 8.8% for P_3 based predictions. All parameter sets, however, resulted in Dice values (panel (b)) greater than 0.83 at days 5 thru 10. An increased level of agreement was observed at the voxel level (panel (c)) for P_3 based predictions (CCC: 0.80 – 0.99) relative to P_1 based predictions (CCC: 0.53 – 0.93) and P_2 based predictions (CCC: 0.74 – 0.98).

Table 3.1 shows the mean percent error between the true values and estimated values of k, D_{wm}, and D_{gm}. Using all three time points resulted in less than 1.0% error in estimates of D_{wm}, whereas using two time points (days 0 and 4 or days 2 and 4) resulted in greater than 49.5% error. Less than 6.2% error was observed in estimates of D_{gm} when using days 2 and 4 or days 0, 2, and 4, while 13.7% error was observed when using days 0 and 4 to estimate model parameters. Similarly, the highest mean error in k was observed for parameters estimated from days 0 and 4 (28.3 ± 2.9%), while lower error was observed for the approaches using days 2 and 4 (13.1 ± 2.1%) and days 0, 2, and 4 (5.9 ± 1.8%).

Table 3.1. Parameter estimation error from *in silico* experiments

Percent Error: Mean (Standard Error)

	Days 0 and 4	Days 2 and 4	Days 0, 2, and 4
D_{wm}	-76.2 (0.3)	-49.5 (0.7)	-1.0 (0.5)
D_{gm}	-13.7 (0.3)	-6.2 (0.4)	-0.5 (0.2)
k	28.3 (3.9)	13.1 (2.1)	5.9 (1.8)

3.5.2 In Vivo Experiments

The results of the *in vivo* experiments are shown in Figures 3.6 – 3.8 and Tables 3.2-3.3. Figure 3.6 shows the PCC (a) and CCC (b) analysis for all nine rats, as well as k_{P1}, k_{P2}, and k_{P3} from rats 3 (c – e) and 6 (f – h). The green bars in panels (a – b) represent the comparison of k_{P1} to k_{P2}, while the blue and red bars represent the k_{P1} to k_{P3} and k_{P2} to k_{P3} comparisons, respectively. A high level of correlation existed between k_{P1} and k_{P3} (mean PCC = 0.75, standard error = 0.05)

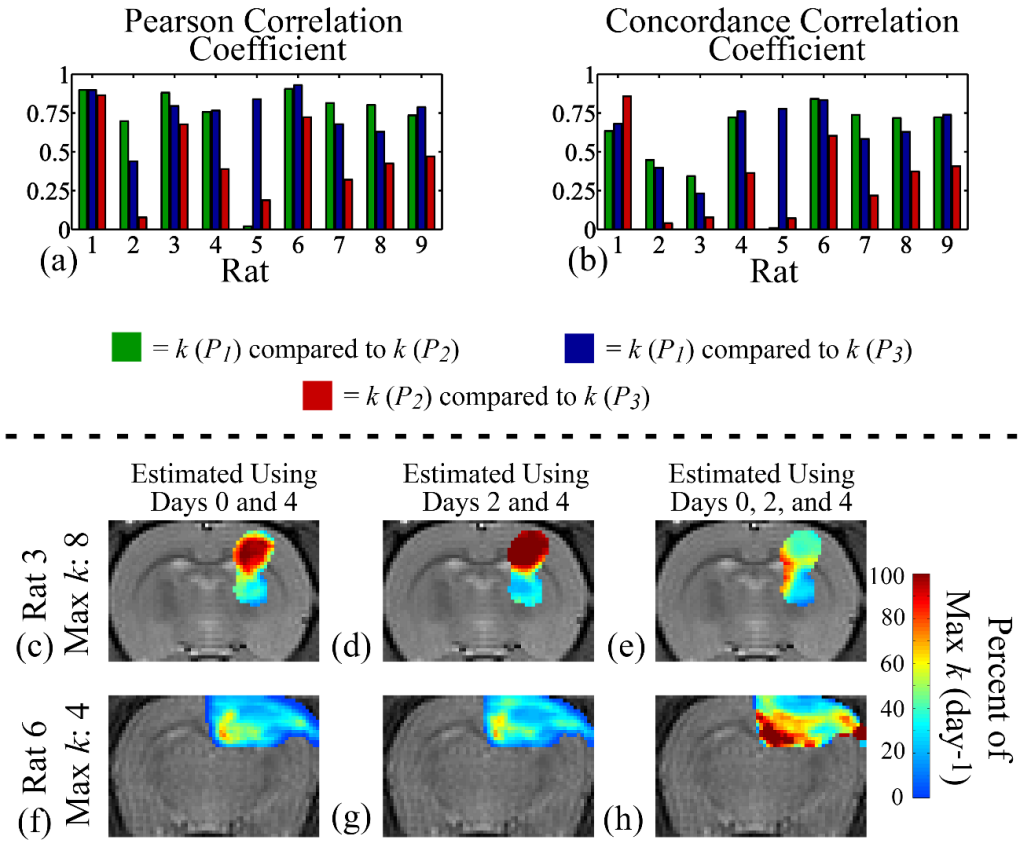

Figure 3.6. Estimated proliferation rate maps from *in vivo* study. Panels (a-b) show the results of the PCC and CCC analysis between k_{P1} to k_{P2} (green bars), k_{P1} to k_{P3} (blue bars), and k_{P2} to k_{P3} (red bars) for each rat. Higher agreement and correlation was observed between k_{P1} to k_{P2} and k_{P1} to k_{P3}, while weaker correlation and agreement was observed between k_{P2} to k_{P3}. Proliferation rate maps from the central slice of rat 3 (c-e) and 6 (f-h) are also shown above. Panels (c) and (f) show the estimated k_{P1}, whiles panels (d) and (g) show k_{P2} and panels (e) and (h) show k_{P3}. The proliferation rates in each image range from 0 to the maximum k of each rat (max k = 8 for rat 3, max k = 4 for rat 6). The proliferation maps demonstrate spatial heterogeneity of proliferation rates within the tumor. Additionally, the magnitude of k varies between the methods (i.e., using P_1, P_2, or P_3) used to estimate k.

and between k_{P1} and k_{P2} (mean PCC = 0.72, standard error = 0.09) compared to k_{P2} to k_{P3} (mean PCC = 0.46, standard error = 0.08). Similar comments apply to the CCC trends. Panels (c – h)

show estimated k_{P1} (panels (c) and (f)), k_{P2} (panels (d) and (g)), and k_{P3} (panels (e) and (h)) for rats 3 and 6. Rat 3 (c-e) is an example of a rat with a high level of correlation (PCC: 0.68 to 0.88) but a low level of agreement (CCC: 0.08 to 0.34). Rat 6 (f-h), however, is an example of a rat with both a high level of correlation (PCC: 0.72 to 0.93), and a high level of agreement (CCC: 0.60 to 0.84).

Figure 3.7 shows the true (panel (a)) and the predicted tumor cell distributions (top rows in panels (b – d)) and the percent difference between the true and predicted distributions (bottom rows in panels (b – d)) for rat 1. The left column in panel (a) shows T_2-weighted images with a white box indicating the simulation domain and a black outline around the tumor. Panel (b) shows estimated k and the predicted N at day 5 using P_1, P_2, and P_3. Decreased k_{P1} (mean ± standard error; 0.08 ± 0.02 day^{-1}), k_{P2} (0.13 ± 0.03 day^{-1}), and k_{P3} (mean ± standard error; 0.08± 0.02 day^{-1}) were observed for the low cell density regions relative to the rest of the tumor (k_{P1}; 1.51 ± 0.06 day^{-1}, k_{P2}; 1.87 ± 0.10 day^{-1}, k_{P3}; 1.32 ± 0.05 day^{-1}). The highest error between N and N_{pred} at day 5 was observed for parameters P_3 (mean ± standard error; 17.80 ± 0.50%) compared to P_1 (17.07 ± 0.50%) and P_2 (17.12± 0.51%). Increased error (greater than or equal to 100% error) is observed between N and N_{pred} at both the periphery and in regions where N has low cell numbers (less than 50% of a voxels carrying capacity). This pattern is observed also in panels (c) and (d). Increased error at day 8 (panel (c)) was observed relative to day 5 (panel (b)) with P_1 predictions having the highest error (32.58 ± 0.63%) compared to P_2 (28.27 ± 0.57%) and P_3 (31.43 ± 0.61%). The predicted N at day 10 (panel (d)) shows an overestimation of tumor size for P_2 based predictions

compared to P_1 or P_3 based predictions. However, at the voxel level the highest mean error was observed for P_1 based predictions (35.80 ± 0.54%) relative to P_2 (35.03 ± 0.53%) and P_3 (33.45 ± 0.51 %) based predictions.

Figure 3.8 presents the global and local level error analysis for the *in vivo* experiments. Panels (a-c) show the results when a spatially variant k (i.e., $k(\bar{x})$) is estimated and panels (d-f) show the results for the spatially invariant estimated k (i.e., k_{ROI}). For the spatially variant k, percent error in tumor volume (panel (a)) for P_1, P_2, and P_3 based predictions ranged from 14 – 34%, 16 – 50%, and 12 – 29%, respectively. Lower Dice values (panel (b)) were observed compared to the *in silico* study and ranged from 0.67-0.81 for all approaches. Similarly, the *in vivo* study had decreased level of agreement (panel (c)) compared to the *in silico* study with CCC's less than 0.33 for all approaches. For the spatially invariant k, percent error in tumor volume (panel (d)) for P_1, P_2, and P_3 based predictions ranged from 36 – 58%, 36 – 77%, and 32 – 54%, respectively. The Dice values were also lower than the *in silico* study and ranged from 0.66-0.79. Lower agreement (CCC < 0.25) at the voxel level was also observed for the spatially invariant k approach compared to the spatially variant k approach. The spatially invariant k's percent error in tumor volume was significantly greater ($p < 0.05$) than the spatially variant k's results for all parameter sets. Similarly, both the Dice and CCC values were significantly smaller ($p < 0.05$) for the spatially invariant k predictions compared to the spatially variant k predictions.

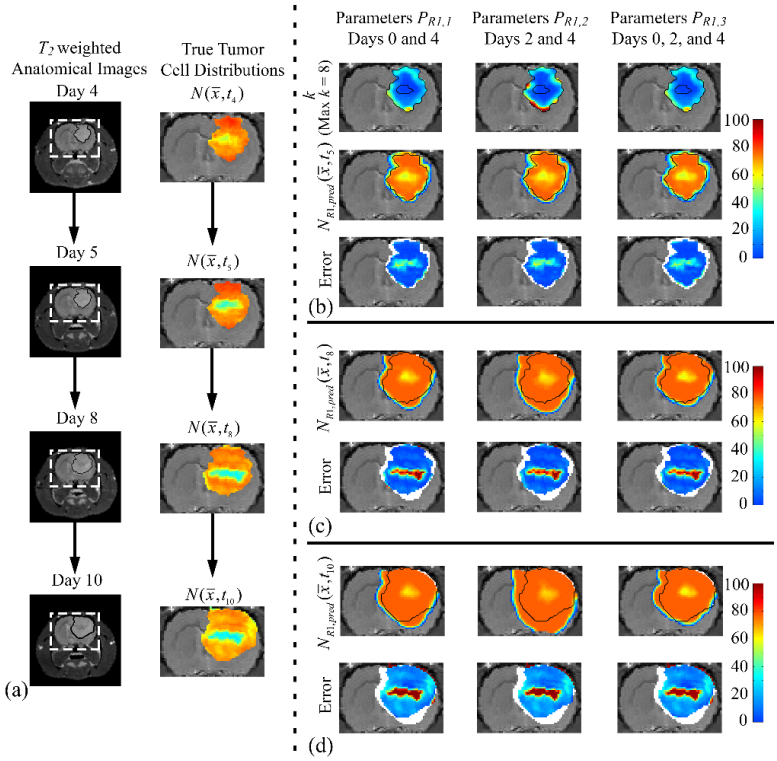

Figure 3.7. True and predicted tumor cell distributions for rat 1. The true and predicted tumor cell distributions for an example rat (rat 1) from the *in vivo* study are shown above. Panel (a) shows the T_2 weighted anatomical images (left column, black lines representing tumor ROI, white box representing simulation domain) and the true N (right column) at the central slice of the tumor volume on days 4, 5, 8, and 10. The predicted N (N_{pred}) and the error between N and $N_{R1,pred}$ for the same slice on days 5, 8, and 10 are shown in panels (b – d). The estimated k is also shown in panel (b). The color bars represent percent of max k value (top row in panel (b)), the percent of the carrying capacity (rows labeled '$N_{R1,pred}$'), and percent error (bottom rows). The black outline displayed within the k maps represent areas of low cell density on day 4. White regions observed in the percent error maps represent areas where no tumor cells were observed in the true data set. The black outline displayed on N_{pred} in panels (b – d) represent the tumor periphery observed in the true tumor cell distributions in panel (a). The top rows in panels (b – d) represent $N_{R1,pred}$, while the bottom row represents the percent difference between N and $N_{R1,pred}$. Additionally, the three columns in panels (b – d) represent the results using parameters $P_{R1,1}$, $P_{R1,2}$, and $P_{R1,3}$. Increased error (greater than or equal to 100%) is generally observed at the periphery of the tumor relative to the interior of the tumor (less than 20% error). Increased error between $N_{R1,pred}$ and N (greater than or equal to 100%) is also observed in areas where N has low cell numbers (less than 50% of a voxel's carrying capacity).

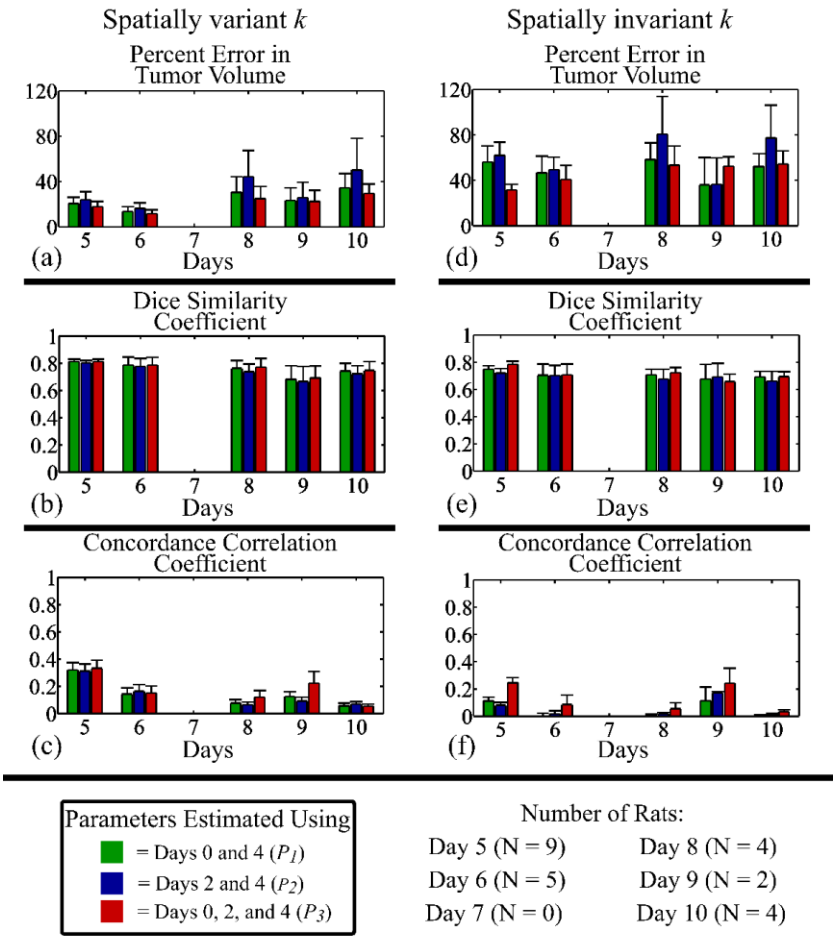

Figure 3.8. Global and local level error analysis for *in vivo* study. Panels (a – c) show the results for the spatially variant *k* predictions and panels (d – f) show the results for the spatially invariant *k* predictions. Panels (a – b) and (d – e) show the result of the global level error analysis, while panels (c) and (f) show the results of the local level error analysis for the *in vivo* experiments. The mean and standard error of each measurement is plotted at days 5 through 10. Panel (a) shows that greater than 11.7% error is observed for all predictions when using days 0, 2 and 4. No significant difference ($p > 0.05$) was observed between the results of the three different parameter sets. The Dice values (panel (b)) show that no significant difference ($p > 0.05$) was observed between the results using the three different parameter sets. Panel (c) shows a steady decrease in the level of voxel agreement (decrease in CCC) over time for all sets of parameters, but no significant difference ($p > 0.05$) between parameter estimation approaches. Predictions made with the spatially invariant *k* (panels (d – f)) resulted in increased percent error in tumor volume and decreased tumor volume agreement (lower Dice values) and decreased voxel level agreement (CCC < 0.25).

The average diffusion estimates and the nRMS error for both the spatially variant and invariant *k* models are shown in Table 3.2. For the spatially variant *k* model fits, the mean D_{wm} ranged from 1.49×10^4 to 1.57×10^4 μm^2/day, and the mean D_{gm} per animal ranged from 1.58×10^4 to 1.99×10^4 μm^2/day. The cumulative error (nRMS error) was lowest for P_3 based predictions (0.49) compared to P_1 (0.54) or P_2 (0.81) based predictions. The spatially invariant *k* model optimization resulted in higher diffusion values for both D_{wm} (greater than 3.05×10^4) and D_{gm} (greater than 3.50×10^4) compared to the spatially variant *k* results. Increased cumulative error (nRMS error > 1.04) was also observed compared to the spatially variant *k* results.

Table 3.2. Average diffusion parameter values and nRMS error from *in vivo* experiments
Mean (Standard Error)

			Days 0 and 4	Days 2 and 4	Days 0, 2, and 4
Spatially	Variant	D_{wm} (μm^2/day)	1.53×10^4 (3.71×10^3)	1.49×10^4 (4.71×10^3)	1.57×10^4 (4.15×10^3)
		D_{gm} (μm^2/day)	1.71×10^4 (2.87×10^3)	1.99×10^4 (3.86×10^3)	1.58×10^4 (4.81×10^3)
		nRMS error	0.54 (0.15)	0.81 (0.29)	0.49 (0.13)
Spatially	Invariant	D_{wm} (μm^2/day)	3.26×10^4 (1.09×10^4)	3.05×10^4 (1.01×10^4)	5.2×10^4 (2.07×10^4)
		D_{gm} (μm^2/day)	3.50×10^4 (1.13×10^4)	3.59×10^4 (8.60×10^3)	8.01×10^4 (1.99×10^4)
		nRMS error	1.27 (0.35)	1.73 (0.55)	1.04 (0.28)

Table 3.3 shows the average proliferation rate for each rat from the spatially variant ($k(\bar{x})$, where $\overline{k(\bar{x})}$ is the average voxel-wise *k* estimated within the tumor) and the estimated spatially invariant proliferation rate (k_{ROI}). $\overline{k(\bar{x})}$ ranged from 0.51 to 4.06 day^{-1}, while k_{ROI} ranged from

0.94 to 9.94 day^{-1}. k_{ROI} was larger than $\overline{k(\bar{x})}$ for six rats for parameter estimates using day 0 and day 4, nine rats for days 2 and 4, and three rats when all three time points were used.

Table 3.3. Average *k* values from *in vivo* experiments

Mean (Standard Error), Units: (day^{-1})

		Days	Days	Days
Rat 1	$\overline{k(\bar{x})}$	2.39 (0.03)	3.38 (0.05)	3.24 (0.04)
	k_{ROI}	2.38	4.22	1.54
Rat 2	$\overline{k(\bar{x})}$	1.51 (0.01)	0.84 (0.01)	1.78 (0.02)
	k_{ROI}	1.30	0.94	1.41
Rat 3	$\overline{k(\bar{x})}$	2.32 (0.04)	4.06 (0.07)	1.08 (0.02)
	k_{ROI}	2.11	8.32	1.53
Rat 4	$\overline{k(\bar{x})}$	1.62 (0.03)	1.54 (0.04)	1.50 (0.03)
	k_{ROI}	2.90	3.38	1.69
Rat 5	$\overline{k(\bar{x})}$	2.97 (0.08)	1.57 (0.03)	3.15 (0.11)
	k_{ROI}	5.75	2.44	2.13
Rat 6	$\overline{k(\bar{x})}$	0.64 (0.04)	0.51 (0.06)	0.94 (0.04)
	k_{ROI}	1.01	1.26	1.26
Rat 7	$\overline{k(\bar{x})}$	1.99 (0.03)	1.40 (0.03)	2.69 (0.03)
	k_{ROI}	2.76	5.31	1.94
Rat 8	$\overline{k(\bar{x})}$	2.59 (0.04)	1.88 (0.04)	2.63 (0.04)
	k_{ROI}	2.69	2.70	2.25
Rat 9	$\overline{k(\bar{x})}$	3.44 (0.07)	3.84 (0.07)	2.76 (0.06)
	k_{ROI}	9.94	8.19	2.07

$\overline{k(\bar{x})}$ is the average *k* estimated voxel-wise within the tumor

k_{ROI} is the spatially invariant *k* estimated for the tumor

3.6 Discussion

The results of the in silico experiments indicate that the parameters within the reaction diffusion equation (i.e., D_{wm}, D_{gm}, and k) can be accurately estimated and then used to accurately predict future tumor growth at the local and global levels, provided the tumor's growth is described by the reaction diffusion equation. While parameters estimated from data with experimentally observed noise does increase the error between the true and estimated values, when three time points are used the error between the true and observed parameters is less than 5.86%. Thus, the addition of a third time point decreases the sensitivity of the parameter optimization algorithm to approximately the same level of noise that is present in the measurement. The increased error observed for D_{wm} relative to D_{gm} may be explained due to only 4% of the voxels in the domain being identified as white matter. The limited number of voxels containing white matter most likely makes the model less sensitive to changes in D_{wm} compared to D_{gm}.

The results of the *in silico* study show, the strength of both the estimated parameters and the forward evaluation algorithm, as exhibited in the high level of overlap of tumor volumes (Dice values greater than 0.83 for P_1, P_2, and P_3) and strong agreement at the local level (CCC values greater than 0.80 for P_3; greater than 0.53 for P_1 and P_2) between N and N_{pred} (Figure 3.5). The largest disagreements occur at the tumor edges. The simple propagation (local average) of proliferation rates outside of the parameter estimation region propagates errors and may need to be improved to incorporate additional information (e.g., local cellularity, distance from vasculature, and nutrient concentration; importantly such data is also available from clinically

relevant, non-invasive imaging studies [142]). The significant differences in prediction errors (globally and locally) between the two time point approaches (P_1 and P_2) suggest the parameter optimization approach is sensitive to the spacing between measurements (P_1: 4 days, P_2: 2 days). Additionally, the lower error in P_2 based predictions compared to P_1 based predictions suggest that the tumor growth between days 2 and 4 is more representative of future growth than growth between days 0 and 4.

The *in vivo* experiments demonstrated greater error at both the global and local level compared to the *in silico* experiments. The increased error suggests that the reaction diffusion equation is an incomplete description of C6 biology. The overestimation of tumor volume estimates suggests that overall tumor growth properties are changing between the estimation time points and the prediction time points. At the global level, the expansion of the tumor may be less restricted at earlier time points compared to later time points. At the local level, these changes may be the result of an increase or decrease in proliferation due to changes in the viability of the cells within a particular voxel. The very poor CCCs (less than 0.33, Figure 3.8) similarly suggest that the reaction diffusion equation provides a poor description of local properties. The reaction diffusion equation does, however, provide tumor growth predictions that co-localize (Dice values greater than 0.62) with the true tumor volumes. Different from the *in silico* study, P_1 predictions had lower percent error in tumor volume (less than 34.4%) compared to P_2 based predictions (less than 50.1%). This suggests that the tumor growth over days 0 and 4 are more representative of future *in vivo* growth than the tumor growth over days 2 and 4. The larger distance between

measurements allows potentially inconsistent growth rates between days 0 and 2 and days 2 and 4 to be averaged over 4 days, lessening the effects of non-representative volumetric growth on model estimates and predictions. Replacing the voxel-specific proliferation, $k(\vec{x})$, with a tumor-specific proliferation rate, k_{ROI}, resulted in larger global (increased percent error in tumor volume, decreased Dice values) and local (decreased CCCs) level errors. The decreased agreement between predicted and observed tumor ROIs (decreased Dice values) using k_{ROI} suggest that a spatially variant k is an important factor in predicting tumor geometry by allowing variations in regional tumor expansion. This factor may also contribute to the increased tumor volume error due to a more uniform expansion of tumor growth.

There are several limitations in this current approach. One limitation is the assumption that all tumor cells within a given voxel (spatially variant k) or within the tumor (spatially invariant k) follow the same proliferation rules. Within tumors there may be groups of actively proliferating cells as well as cells that are quiescent or necrotic [143]. In particular, necrotic tissues (which can be relatively large compared to total tumor volume) can strongly influence tumor growth [143] and patient prognosis [94,144]. Models incorporating different proliferation rules have the potential to more accurately describe *in vivo* proliferation [100,145]; however, it is challenging to initialize these models using non-invasive measurements. Although the proliferation model in this approach is limited, the spatially variant k lessens the potential error (relative to k_{ROI}) in this assumption by discretizing the tumor into individual regions that can have a proliferation rate that more closely captures local behavior. A second limitation is that proliferation rates, k, estimated

from early time points are assumed to be constant for the remainder of the tumor growth. The logistic growth term in Eq. (3.1) allows for temporally variation of the instantaneous growth rate as cell density increases or decreases, but it does not allow for the individual voxel proliferation rates to vary temporally over the course of the experiment; this is a fundamental limitation of this model as formulated. As *in vivo* tumors expand, the characteristics of a cell's environment will change and either accelerate or slow future cell proliferation. A more realistic model would incorporate these phenomena [12,13] and adjust the spatio-temporal distribution of k throughout the simulation. These approaches, however, require model parameters that are extraordinarily difficult to measure non-invasively thereby limiting their application to subject-specific model predictions. This approach also does not consider the impact that tumor necrosis and edema may have on tumor cell proliferation [105,143,146] and the estimation of cellularity from ADC measurements (e.g., increased water diffusion may be observed in necrosis or necrosis adjacent regions due to breakdown of barriers to free water movement). However, there currently is not a widely accepted or validated method for segmenting necrosis and edema *a priori* in brain tumors. A third limitation is that as the tumor expands into voxels not included in the parameter estimation procedure (i.e., voxels outside of the tumor ROI determined at day 4), the proliferation rate in that voxel is then assigned as the average of the nearby known proliferation rates. This average value of the local k does not account for differences in environmental conditions, cell distributions, or cell phenotypes that may alter a voxel's k. A fourth limitation of Eq. (3.1) is that D is temporally fixed which results in tumor growth that is unrestricted (i.e., the model assumes that the tumor is

growing into an empty space and does not incorporate the effects of the surrounding tissue [147]) and unresponsive to changes in microenvironment properties (e.g., extracellular matrix components, growth factors, tumor necrosis factor, matrix-metalloproteinase [148,149]). This limitation can be amended through including more realistic terms such as mass effect [26,150] to temporally adjust tumor migration behavior which may increase the predictive accuracy of the model. We do note, though, that the models which include the spatial-temporal evolution of D and k must carefully consider how the model parameters will be initialized (i.e., how are the values for the additional model parameters assigned) to provide subject-specific tumor growth predictions. The poor predictive strength of the current model and the temporally constant proliferation rates hinders the reliability of both untreated (and, most likely, treated) tumor growth predictions. Expanding the model to include an additional term to describe the effect of treatment (i.e., death rate as a function of drug dose or radiation dose) or fitting for a post-treatment proliferation rate would provide a platform to compare observed treatment response to predicted treatment response.

In conclusion, parameters can be accurately estimated and used to predict future tumor growth with low error at the global and local levels, provided that the tumor's growth is described by the reaction diffusion equation. However, the *in vivo* experiments suggest that the reaction diffusion model consisting of just tumor cell diffusion and logistic growth described by Eq. (3.1) provides an incomplete description of tumor growth and must be amended to provide better descriptions of *in vivo* C6 glioma growth in rats.

3.7 Acknowledgements

The authors thank Zou Yue for performing the animal surgeries. We thank the National Institutes of Health for funding through NCI R01CA138599, NCI R21CA169387, NCI U01CA174706, NCI R25CA092043, and the Vanderbilt-Ingram Cancer Center Support Grant (NIH P30CA68485). We thank the Kleberg Foundation for the generous support of our institute's imaging program. ECR holds a Career Award from the BWF. This work was partially supported by a pilot project from the Physical Sciences in Oncology Center at the H. Lee Moffitt Cancer Center and Research Institute (PIs: Robert Gatenby, M.D., Robert Gillies, Ph.D.).

CHAPTER 4

A MECHANICALLY-COUPLED REACTION DIFFUSION MODEL THAT INCORPORATES INTRA-TUMORAL HETEROGENEITY TO PREDICT *IN VIVO* GLIOMA GROWTH

Aim 2: Develop a model that accurately captures bulk tumor growth and intra-tumor cellularity

4.1 Introduction and Contribution of Study

This study focused on developing and evaluating several model variations to address the shortcomings of the standard reaction diffusion model (Chapter 3). The first model coupled tumor cell diffusion to local tissue stress (the mechanically coupled model, or 'MC' model) in an attempt to reduce the overestimation of tumor growth predicted by the standard reaction diffusion equation. While several groups have incorporated mechanical properties into biophysical tumor models [19,26,28,29,73,109], this is the first application to a murine model of glioma growth. The second model incorporated a voxel-specific carrying capacity (the 'CC' model) to reduce voxel-level error. The voxel-specific carrying capacity was a simplified alternative to building a set of coupled partial differential equations (and the concomitant set of problems of having to estimate several additional parameters) to describe both the physical and environmental limitations on tumor cell growth. The CC model was also a novel application of this model to tumor modeling. The third model combined the MC and CC models (the 'MC-CC' model) to reduce both global and local level errors. The results of this study demonstrated that incorporating a mechanically coupled

diffusion coefficient (MC and MC-CC models) resulted in significantly decreased error in tumor volume compared to the reaction diffusion model, while the voxel-specific carrying capacity (CC and MC-CC models) also significantly decreased error in voxel cell number compared to the reaction diffusion model.

This work contributed to the cancer modeling field by building and evaluating three models of glioma growth applied to a murine model and demonstrating that tumor growth can accurately be predicted using the MC-CC model. The CC and MC-CC models demonstrated a novel (and simplified) means to incorporate local heterogeneity in cell number into a predictive model. Furthermore, the MC and MC-CC models showed the importance of coupling tumor cell diffusion to local tissue stress in modeling of glioma growth in 14 *in vivo* subjects. This work is in review at *IEEE Transactions on Medical Imaging*.

4.2 Abstract

While gliomas have been extensively modeled with the reaction diffusion equation it is most likely an oversimplification of *in vivo* glioma growth. In this study, three mathematical models of glioma growth are developed and systematically investigated to develop a framework for accurate prediction of changes in tumor volume as well as intra-tumoral heterogeneity. To more realistically describe tumor growth, we have coupled tumor cell movement to tissue stress, leading to a mechanically coupled (MC) reaction diffusion model. To describe intra-tumor heterogeneity, we include a voxel-specific carrying capacity (CC) to the reaction diffusion model. The MC and

CC models were also combined in a third model (MC-CC). To evaluate these models, rats (n = 14) with C6 gliomas were imaged with diffusion-weighted magnetic resonance imaging (DW-MRI) and contrast enhanced MRI (CE-MRI) over ten days. For each time point, DW-MRI was used to estimate cell number within the tumor regions (determined by CE-MRI). Each of the three models were fit to the cellularity data obtained on days 10, 12, and 14 post-tumor implantation to obtain estimates of model parameters. The estimated model parameters were then used to predict future tumor growth from days 15-20 which could then be directly compared to experimental data. The results show that the MC-CC model best describes *in vivo* glioma growth resulting in a statistically significant ($p < 0.05$) decrease in both global and local errors compared to the reaction diffusion model. The CC and MC-CC models accurately described intra-tumor heterogeneity with less than 12% error at the voxel-level. The results in this work demonstrate that mechanobiological effects are a necessary component to brain tissue tumor modeling efforts. In addition, the results are suggestive that models expressing a variable tissue carrying capacity are a needed component to capture tumor heterogeneity. Lastly, the results advocate the need for additional effort toward capturing tumor-to-tissue infiltrative margin geometries.

4.3 Introduction

A fundamental challenge in the care of patients with brain tumors is the limitation of standard radiographic measurements to accurately evaluate patient response and capture tumor growth kinetics. Biophysical models that incorporate patient specific measurements may be able

to address this challenge by providing accurate predictions of tumor growth and treatment response through which clinical care can be guided [16]. We [9,19,63,73,74,151] and others [20,21,24,26,28] have proposed that a practical way forward is to initialize and constrain predictive models via imaging data that can be acquired noninvasively, in 3D, and at numerous time points. Examples of such data include magnetic resonance imaging (MRI) or positron emission tomography (PET) measurements that are routinely available and can characterize tumor vascularity and perfusion [56,152], tumor cellularity [53], metabolism [153], and hypoxia [154].

A common predictive model in the mathematical analysis of tumors is a reaction diffusion (RD) model which describes the proliferation (reaction) and movement (diffusion) of tumor cells. Several groups have investigated neoplastic growth using variations of this model in several organ sites (brain [21,26,28,74,109], breast [19,73], pancreas [20], kidney [113]) and non-specifically [155–158]. In the pre-clinical setting, we have previously used MRI data collected at three time points to estimate rat-specific diffusion and proliferation parameters which were then used to predict the *in vivo* spatio-temporal evolution of the tumor. These predictions were then directly compared to experimental MRI data collected at future time points. We previously observed [74] the RD model incompletely described *in vivo* C6 glioma growth at both the global (high error in tumor volume, low agreement in tumor shape) and local (high error in voxel cell number) levels. In the present study, we seek to modify the standard RD model to improve the accuracy of model predictions at both the global and local levels.

One possibility for the high global level errors is the assumption that the diffusion coefficient is constant in time. In the standard RD model, tumor growth is restricted only by the bounds of the simulation domain (e.g., the skull in the case of a rat glioma) and not inhibited by the surrounding brain tissue. However, the force exerted by the surrounding tissue [159] during tumor expansion is a critical biological interaction that can alter both tumor expansion [147] and shape [160]. This mechanobiological interaction between the tumor mass and surrounding tissue mass has been previously incorporated into modeling brain [26,28,109,110], breast [19,73], kidney [113], and pancreatic [20] cancer. Here, we apply it to modeling *in vivo* C6 glioma growth in using a mechanically coupled RD model (MC).

Similarly, the high local level errors observed *in vivo* are a result of fundamental limitations of the standard RD model at describing intra-tumoral heterogeneity. More specifically, with a temporally constant proliferation rate and carrying capacity the cell number will saturate at steady-state within the tumor resulting in a homogenous distribution of tumor cells. The limitation of temporally constant proliferation can be addressed by incorporating additional equations or terms into the RD model that result in cell death or alteration of their proliferation status [99,108,161]. However, parameterizing these models on a subject-specific basis is challenging as they often have many free parameters that must be assigned in some reasonable way. Heterogeneity in cell density can also be obtained through spatially varying the carrying capacity which may occur due to physical limitations (e.g., decrease in available space to grow) and environmental limitations (e.g., poorly perfused, low nutrient concentration). The physical limitations on growth can be

incorporated through the use of imaging measurements which can provide estimates of the vascular and extracellular-extravascular volume fractions [151]. Similarly, models that incorporate vascular growth or remodeling [162] can also account for these spatial variations in carrying capacity. In this work, we investigate a simplified alternative to these approaches to build in heterogeneity by linking the physical and environmental limitations on carrying capacity to a single lumped model parameter which can be easily estimated throughout the tumor from data observations (this model is termed the carrying capacity RD model, or CC).

In this contribution, we seek to evaluate the ability of the MC, CC, and MC-CC (the combination of the MC and CC models) models to predict future tumor growth. Using serial DW-MRI data acquired in a murine glioma model we first estimate rat-specific model parameters to initialize and constrain the RD, MC, CC, and MC-CC models for predicting the spatio-temporal tumor evolution. Model predictions are then directly compared to the future MRI measurements.

4.4 Theory

4.4.1 Reaction Diffusion Model (RD)

The reaction diffusion model, Eq. (4.1), describes the change in the distribution and number of tumor cells due to the random movement of tumor cells (diffusion) and proliferation (reaction):

$$\frac{\partial N(\bar{x},t)}{\partial t} = \nabla\bullet\left[D(\bar{x})\nabla N(\bar{x},t)\right] + k(\bar{x})N(\bar{x},t)\left(1-\frac{N(\bar{x},t)}{\theta}\right), \tag{4.1}$$

where $N(\bar{x},t)$ is the number of cells at three-dimensional position $\bar{x}$ and time *t*, $D(\bar{x})$ is the cell diffusion coefficient at position $\bar{x}$, θ is the cellular carrying capacity (i.e., the maximum number of cells a region can support), and $k(\bar{x})$ is the tumor cell proliferation rate. Measurements from DW-MRI are used to provide estimates of $N(\bar{x},t)$ at several time points [72,74]. These $N(\bar{x},t)$ are then used to solve an inverse problem of Eq. (4.1) to return estimates of the model parameters *P*. For the RD model *P* (P_{RD}) includes voxel-wise values of $k(\bar{x})$ and two global $D(\bar{x})$ parameters, one for all voxels within the white matter and one for all voxels within the gray matter. A three dimension in space (Δx = 250 μm, Δy = 250 μm, Δz = 1000 μm), fully explicit in time (time step = 0.01 days) finite difference (FD) simulation is used to solve the forward evaluation of Eq. (4.1) written in Matlab (Mathworks, Natick, MA). $N(\bar{x},t)$ has no diffusive flux at the brain tissue boundaries (Neumann boundary condition). (Appendix A provides further details on the finite difference implementation of Eq. (4.1).)

4.4.2 Mechanically Coupled Model (MC)

To address the high global level errors produced by the RD [74] model, a mechanically coupled (MC) reaction diffusion model [19,73,109] will be used. The MC model is based on observations that the growth of tumor spheroids is inhibited as the stiffness of the embedded matrix increases [147,163]. Furthermore, as the tumor volume expands the tumor induces significant mechanical stress on the surrounding tissue [164] resulting in a mass effect. Thus, as the tumor expands there is an increasing amount of mechanical stress which can restrict further expansion

by the tumor. These biophysical effects are incorporated in the MC model by altering Eq. (4.1) to incorporate a diffusion coefficient, Eq. (4.2), that is spatially and temporally variant in response to local tissue stress:

$$D(\bar{x},t) = D_0 \cdot e^{-\lambda_1 \cdot \sigma_{vm}(\bar{x},t)}, \tag{4.2}$$

where D_0 represents tumor cell diffusion in the absence of mechanical restrictions, λ_1 is an empirically derived stress-tumor cell diffusion coupling constant, and $\sigma_{vm}(\bar{x},t)$ is the von Mises stress. Therefore, as the local von Mises stress increases, tumor cell movement will be inhibited by a decrease in the tumor cell diffusion coefficient, $D(\bar{x},t)$. $\sigma_{vm}(\bar{x},t)$ is determined by calculating the tissue displacement ($\vec{u}$) caused by the growing tumor. Eq. (4.3), which is the linear elastic isotropic mechanical equilibrium equation with an expansion force related to $N(\bar{x},t)$, is used to solve for $\vec{u}$:

$$\nabla \cdot G\nabla\vec{u} + \nabla\frac{G}{1-2\nu}(\nabla\cdot\vec{u}) - \lambda_2\nabla N(\bar{x},t) = 0\ , \tag{4.3}$$

where G is the shear modulus, ν is Poisson's ratio, and λ_2 represents a tumor cell force coupling constant. The gradient of $\vec{u}$ is then calculated to obtain the shear and normal strains. Eq. (4.4), shows the normal (ε_{xx}) and shear (ε_{xy} and ε_{xz}) strains calculated from the displacement map in the x-direction (u_x):

$$\begin{bmatrix} \varepsilon_{xx} \\ \varepsilon_{xy} \\ \varepsilon_{xz} \end{bmatrix} = \begin{bmatrix} \partial u_x/\partial x \\ \partial u_x/\partial y \\ \partial u_x/\partial z \end{bmatrix}, \tag{4.4}$$

similar calculations are repeated in the *y*- and *z*-directions. The principal normal stresses are then calculated using Eq. (4.5) :

$$\begin{bmatrix} \sigma_{xx} \\ \sigma_{yy} \\ \sigma_{zz} \end{bmatrix} = \left(\frac{2G\nu}{1-2\nu} \right) \left(\varepsilon_{xx} + \varepsilon_{yy} + \varepsilon_{zz} \right) + 2G \begin{bmatrix} \varepsilon_{xx} \\ \varepsilon_{yy} \\ \varepsilon_{zz} \end{bmatrix}. \tag{4.5}$$

The principal shear stresses are calculated using Eq. (4.6):

$$\begin{bmatrix} \sigma_{xy} \\ \sigma_{xz} \\ \sigma_{yz} \end{bmatrix} = G \begin{bmatrix} \varepsilon_{xy} \\ \varepsilon_{xz} \\ \varepsilon_{yz} \end{bmatrix}. \tag{4.6}$$

The principal normal and shear stresses that are used to calculate $\sigma_{vm}(\bar{x},t)$ using Eq. (4.7):

$$\sigma_{vm} = \left[\frac{1}{2} \left(\begin{array}{c} \left(\sigma_{xx} - \sigma_{yy}\right)^2 + \left(\sigma_{xx} - \sigma_{zz}\right)^2 + \left(\sigma_{zz} - \sigma_{yy}\right)^2 \\ + 6\left(\sigma_{yx}2 + \sigma_{yz}2 + \sigma_{xz}2\right) \end{array} \right) \right]^{1/2}. \tag{4.7}$$

The estimated parameter set, *P*, for the MC (P_{MC}) model includes voxel-wise $k(\bar{x})$ and one D_0 value. P_{MC} is estimated using the same approach for the RD model (section II.A). Poisson's ratio was set at 0.45, while *G* was assigned region-wise (i.e., cortex = 418 , corpus callosum = 238 Pa , hippocampus = 466 Pa, thalamus = 383 Pa , putamen = 275 Pa) [165,166]. λ_2 was assigned to 5.

Figure 4.1 shows how the mechanically coupled model, Eqs. (4.2) - (4.7), spatially and temporally adjusts tumor cell diffusion. Starting with the current values of $D(\bar{x},t)$, $N(\bar{x},t)$, and $k(\bar{x})$ the FD implementation of Eq. (4.1) is evolved a single time step. Tissue displacement ($\vec{u}$) is then calculated using the gradient of the latest distribution of $N(\bar{x},t)$ *via* Eq. (4.3). $\vec{u}$ can then be used to calculate $\sigma_{vm}(\bar{x},t)$ *via* Eq. (4.7), within the simulation domain. The updated $\sigma_{vm}(\bar{x},t)$ is then used to calculate a new value of $D(\bar{x},t)$ using Eq. (4.2) before starting the next time-iteration. (Appendix B provides further details on the finite difference implementation of Eq. (4.3).)

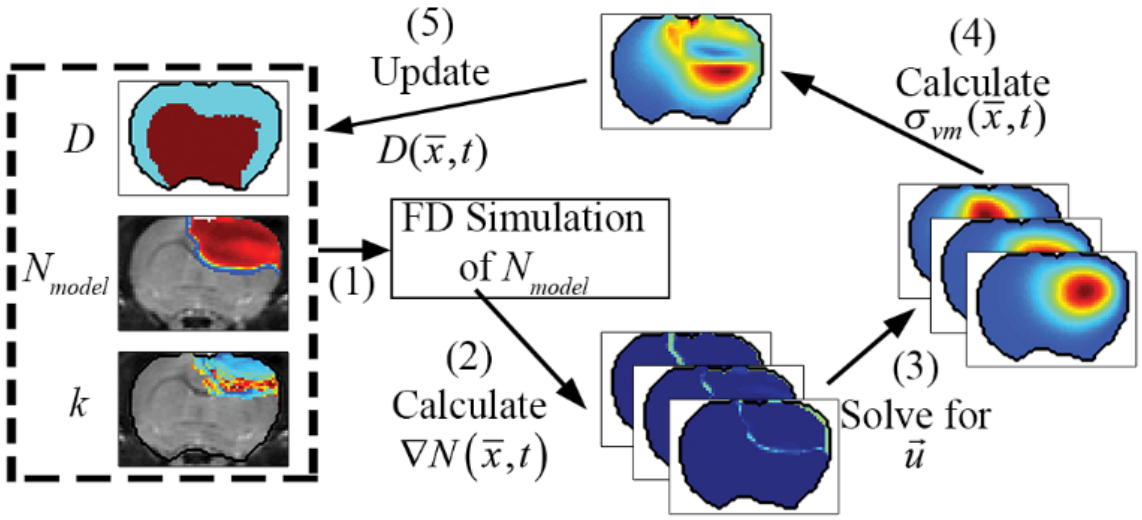

Figure 4.1. The panels depict a single iteration of the mechanically coupled tumor model. The current values of $D(\bar{x},t)$, $N_{model}(\bar{x},t)$, and $k(\bar{x})$ are used in a finite difference simulation, step (1), of Eq. (4.1). The updated $N_{model}(\bar{x},t)$ is then used to calculate $\nabla N(\bar{x},t)$, step (2). Using G, ν, λ_2, and $\nabla N(\bar{x},t)$ Eq. (4.3) is solved for $\vec{u}$ (step 3). $\vec{u}$ is then used to calculate the principal shear and normal stresses, step (4), in order to calculate $\sigma_{vm}(\bar{x},t)$ using Eq. (4.7). $D(\bar{x},t)$ is then updated, step (5), using the current value $\sigma_{vm}(\bar{x},t)$ in Eq. (4.2).

4.4.3 Voxel-Specific Carrying Capacity Model (CC)

Another shortcoming of the reaction diffusion model is that at steady-state it predicts a homogenous distribution of tumor cells within the tumor compared to the heterogeneous distribution observed *in vivo*. The *in vivo* heterogeneous distribution may occur due to several factors including local space limitations (variations in local vascularity or extracellular swelling) and local viability (distance to nearby vasculature, amount of available nutrients). One way to incorporate the heterogeneity observed *in vivo* is to allow the carrying capacity to vary spatially, effectively lumping geometric and metabolic growth constraints into a voxel-wise parameter describing the local carrying capacity. Thus, we amend Eq. (4.1) to incorporate a voxel-specific carrying capacity [167]:

$$\frac{\partial N(\bar{x},t)}{\partial t} = \nabla \bullet \left[\theta_{max} D(\bar{x}) \nabla \left(\frac{N(\bar{x},t)}{\theta(\bar{x})} \right) \right] + k(\bar{x}) N(\bar{x},t) \left(1 - \frac{N(\bar{x},t)}{\theta(\bar{x})} \right), \tag{4.8}$$

where θ_{max} is the maximum number of cells a voxel can physically support. The voxel-specific carrying capacity, $\theta(\bar{x})$, alters both the movement (preferential movement to areas with a lower packing fraction versus areas of lower cell number) and proliferation (maximum cell number varies throughout the tumor) of tumor cells. The estimated parameter set, *P*, for the CC (P_{CC}) model includes voxel-wise $k(\bar{x})$, voxel-wise $\theta(\bar{x})$, and two $D(\bar{x})$ values; one for white matter and one for gray matter. P_{CC} is estimated using the same approach used for the RD model.

4.4.4 Combined Model (MC-CC)

The fourth model amends the RD model to incorporate both a spatially-temporally variant $D(\bar{x},t)$ coupled to local tissue stress (MC) and a spatially variant $\theta(\bar{x})$ (CC). The estimated parameter set, *P*, for the MC-CC ($P_{MC\text{-}CC}$) model includes voxel-wise $k(\bar{x})$, voxel-wise $\theta(\bar{x})$, and one D_0 value.

4.5 Methods

4.5.1 In Vivo Experiments

All experimental procedures were approved by Vanderbilt University's Institutional Animal Care and Use Committee. For all imaging and surgical procedures, rats were anesthetized with 2% isoflurane in 98% oxygen. Female Wistar rats (n = 14, 236-268 g) were anesthetized and inoculated intracranially with C6 glioma cells (1×10^5) *via* stereotaxic injection. A jugular catheter was placed in each rat 8 days after the tumor inoculation surgery for injection of an MRI contrast agent. During each MRI procedure, rat body temperature was maintained near 37° C by a flow of warm air directed over the animal and respiration was monitored using a pneumatic pillow. The first imaging time point occurred 10 days after inoculation surgery. All rats were imaged on days 10, 12, and 14. Additionally, rats 1-4 were imaged on days 15, 16, 18 and 20, rats 5-6 were imaged on days 15, 18 and 20, rats 7-9 were imaged on 15, 16, and 18, rats 10-13 were imaged on days 15 and 16, and rat 14 was only imaged on 15.

MRI data was acquired on a 9.4 T horizontal-bore magnet (Agilent, Santa Clara, CA, USA). The animal's head was positioned in a 38 mm diameter Litz quadrature coil (Doty Scientific, Columbia, SC, USA). All MR images were acquired over a 32 × 32 × 16 mm^3 field of view sampled with a 128 × 128 × 16 matrix. From the beginning of the second through the final imaging session, a mutual information based rigid registration algorithm [74,134] was utilized at the scanner to register the current imaging time point to the initial imaging session.

DW-MRI was acquired using a pulsed fast spin echo diffusion sequence with three orthogonal diffusion encoding directions with *b*-values of 150, 500, and 1100 s/mm^2, and Δ/δ = 25 ms/2 ms. The apparent diffusion coefficient (ADC) was estimated on a voxel basis using standard methods [135]. $N(\bar{x},t)$ was then estimated from *ADC* values [65,66,72] using Eq. (4.9):

$$N(\bar{x},t) = \theta_{max}\left(\frac{ADC_w - ADC(\bar{x},t)}{ADC_w - ADC_{min}}\right), \tag{4.9}$$

where θ_{max} represents the maximum tumor cell carrying capacity for an imaging voxel, ADC_w is the *ADC* of free water at 37° C (2.5 × 10^{-3} mm^2/s) [135], $ADC(\bar{x},t)$ is the ADC value at position $\bar{x}$ and time *t*, and ADC_{min} is the minimum *ADC* value which corresponds to the voxel with the largest number of cells. θ_{max} was calculated using the imaging voxel dimensions, and assuming spherical tumor cells with a packing density of 0.7405 [136] with an average cell volume of 908 μm^3 [137].

T_1 was measured using data from an inversion-recovery snapshot experiment with TR/TE

= 5000/3 ms, TI (inversion time) = (8 TIs logarithmically spaced between 200 - 4000 ms), and two averaged excitations.

Contrast enhanced MRI (CE-MRI) was acquired using a spoiled gradient echo sequence with *TR*/*TE* = 45/1.4 ms, two averaged excitations, and a flip angle = 20° collected before and after the injection of a 200 μL bolus (0.05 mmol kg^{-1}) of gadolinium-diethylenetriamine pentaacetic acid (Gado-DTPA™, BioPhysics Assay Laboratory, Worcester, MA).

4.5.2 Tumor and Tissue Segmentation

Tumor regions-of-interest (ROI) were identified using the difference of the pre- and post-contrast agent images from CE-MRI. The measured tumor cell distribution, $N_{meas}(\bar{x},t)$, was then calculated within these ROIs from *ADC* measurements using Eq. (4.9). T_1 maps were used to define general white and gray matter regions and to identify the cortex, corpus callosum, hippocampus, thalamus, and putamen.

4.5.3 Parameter Estimation

The parameter estimation method is shown in Figure 4.2a. *ADC* maps obtained from DW-MRI are used to provide estimates of $N_{meas}(\bar{x},t)$ at several time points (step 1). In the following text and figures, the notation $t_a \rightarrow t_c$ is used to indicate time points t_a, t_c, and all time points between t_a and t_c. The optimal *P* for each model is determined from $N_{meas}(\bar{x},t_{10} \rightarrow t_{14})$ using a Levenberg-Marquardt weighted least squares optimization (steps 2-4) implemented with a

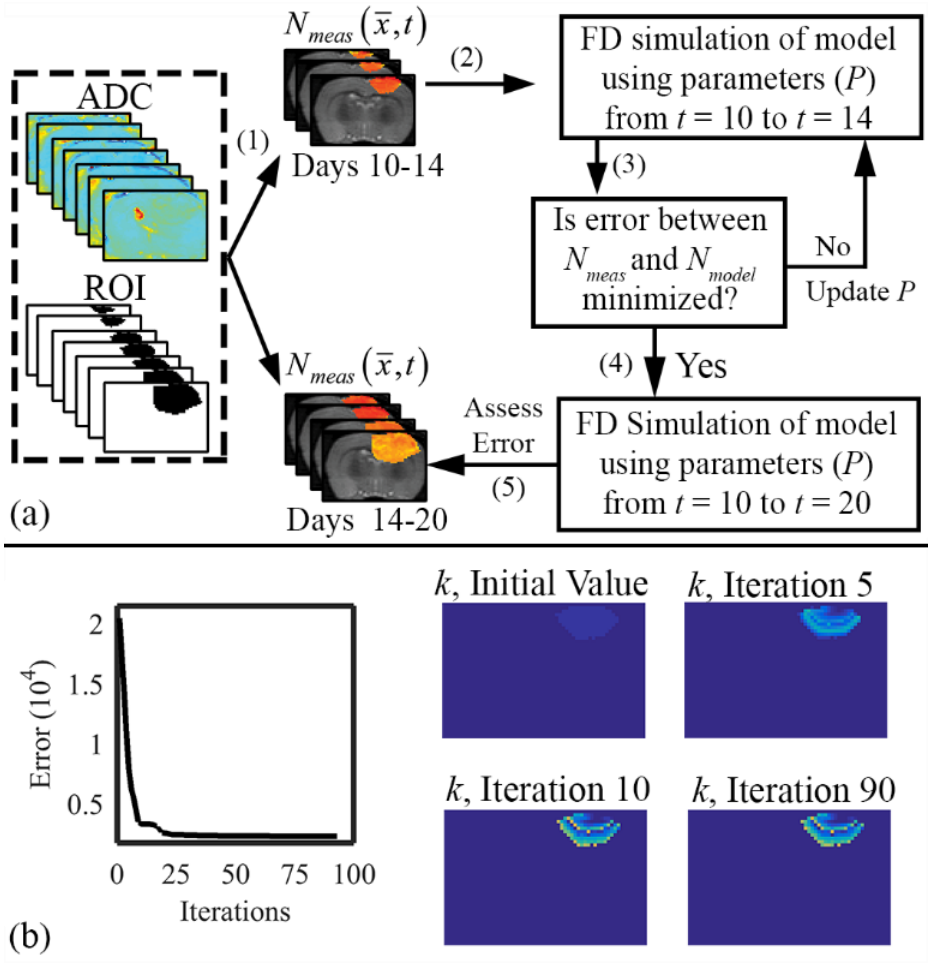

Figure 4.2. Flow chart for parameter optimization of the tumor models. In panel (a), ADC values within the tumor ROIs are used to calculate $N_{meas}(\bar{x},t)$ as indicated by step (1). A finite difference simulation, step (2), is then initialized with $N_{meas}(\bar{x},t=10)$ and an initial guess of P to simulate N at days 12 and 14 ($N_{model}(\bar{x},t)$). Error is then assessed (step 3) between $N_{meas}(\bar{x},t)$ and $N_{model}(\bar{x},t)$ using Eq. (4.10). When the error between $N_{meas}(\bar{x},t)$ and $N_{model}(\bar{x},t)$ is minimized, step (4), the optimized P is used in an additional finite difference simulation to simulate $N(\bar{x},t)$ at days 10 to 20, step (5), otherwise P is updated and the optimization continues. The left side in panel (b) shows the optimization for a representative animal (error in the objective function versus iteration). The right side of panel (b) shows the initial value for k and values of k at the 5^{th}, 10^{th}, and 90^{th} iteration.

regularization parameter described in Joachimowicz *et al* [138]. The optimal P was determined when the objective function, Eq. (4.10) , was minimized:

$$\sum_{t=t_{12}}^{t_{14}} \left(\left(\sum_{\bar{x}=1}^{\bar{x}_i=n} \left(N_{meas}(\bar{x},t) \right) \right)^{-1} \cdot \left(\sum_{\bar{x}=1}^{\bar{x}=n} \left(N_{model}(\bar{x},t) - N_{meas}(\bar{x},t) \right)^2 \right) \right), \tag{4.10}$$

where, t_{12} is the time point at day 12, t_{14} is the time point at day 14, n is the total number of voxels within the tumor, and $N_{model}(\bar{x},t)$ is the model value of N using the current parameter set P. We should note that the introduction the first term normalizes Eq. (4.10) such that no time point is excessively weighted based on the number of activated voxels. $N_{model}(\bar{x},t)$ is $N_{RD}(\bar{x},t)$ for the RD model, $N_{CC}(\bar{x},t)$ for the CC model, $N_{MC}(\bar{x},t)$ for the MC model, and $N_{MC-CC}(\bar{x},t)$ for the MC-CC model. Optimization for a representative animal is shown in Figure 4.2b. The left side of Figure 4.2b shows the objective function versus optimization iteration while the right side shows the initial value of $k(\bar{x})$ and its value at the 5th, 10th, and 90th iteration.

A 3 × 3 Gaussian filter was applied to $N_{model}(\bar{x},t)$ prior to the start of the parameter optimization to reduce the effects of noise within individual voxels. All parameters were constrained to non-negative values. $k(\bar{x})$ was estimated voxel-wise within the tumor ROI and assigned 0 elsewhere. Similarly for the CC and MC-CC model, $\theta(\bar{x})$ was estimated voxel-wise within the tumor ROI and assigned the maximum value elsewhere. A single value of D_0 was estimated for the entire brain.

4.5.4 Forward Evaluation and Error Analysis

After optimization of P for each model, these values were then used in a FD simulation initialized at day 10 and "grown" to each rat's final imaging measurement (Figure 4.2a, steps 5).

The simulated tumor growth (N_{RD}, N_{MC}, N_{CC}, $N_{MC\text{-}CC}$,) was then sampled at time points corresponding to the experimentally acquired imaging time points. As the tumor expanded into regions where an estimate of $k(\bar{x})$ was not obtained, $k(\bar{x})$ was assigned using a local average of available non-zero *k*'s within a 3 × 3 × 3 kernel.

Error between predicted and the measured tumor growth (identified using CE-MRI data) was assessed at the global and local levels. At the global level, error was assessed by calculating the percent error in tumor volume and the average surface distance (ASD). The ASD is the average minimum distance between a voxel on the surface of the model predicted tumor volume and a voxel on the surface of the measured tumor volume. At the local level, error was assessed by calculating the average percent error in cell number, the Pearson correlation coefficient (PCC), and the concordance correlation coefficient (CCC). Percent error in tumor volume was used to assess the error in volume estimates, while the agreement between ROI shapes was assessed using the ASD. The percent error in tumor volume was computed for each model by comparing the predicted tumor volume to the measured tumor volume on days 15-20. Similarly, the predicted tumor ROIs on days 15-20 were compared to the measured tumor volume on the same days to compute the ASD. Error at the local level was assessed at days 15-20 by calculating at each voxel the percent error between $N_{model}(\bar{x},t)$ and $N_{meas}(\bar{x},t)$. The voxel-wise error is then averaged to compute the average percent error in cell number. The PCC and CCC were also calculated to evaluate the correlation and agreement between voxel-wise cell number and the observed cell number. All results are presented as the mean and 95% confidence interval when appropriate.

A 1-way analysis of variance (ANOVA) was used to evaluate the differences in global and local errors between the RD, MC, CC, and MC-CC models. Tukey's honest significant difference test was then used for pairwise comparisons. A p value less than 0.05 was considered significant.

4.6 Results

4.6.1 Mechanically Coupled Model (MC)

Figure 4.3 shows the comparison at the global level of the RD and MC model predictions for rat 6. Rows (a – c) show the entire tumor volume of $N_{meas}(\bar{x}, t)$ with two outlines representing the extent of the tumors simulated from the RD (blue line) and MC (white line) models at days 15, 16 and 18. The MC model resulted in lower error in tumor volume relative to the RD model at day 15. However, as the tumor continues to grow (rows (b – c)), increased error is observed for the RD model at the final imaging time point (27.48% for the RD and 8.16% for the MC model). Panel (d) summarizes the global level error for rat 6 showing a steady increase in percent error in tumor volume for the RD model while the MC model remains below 9%. Similarly, the MC model results in a decreased ASD (0.21 mm for the MC and 0.33 mm for the RD), which is most noticeable at the later time points. It should be noted that while the MC model has lower error in tumor volume, it does underestimate the tumor size in some slices and overestimates the tumor size in others.

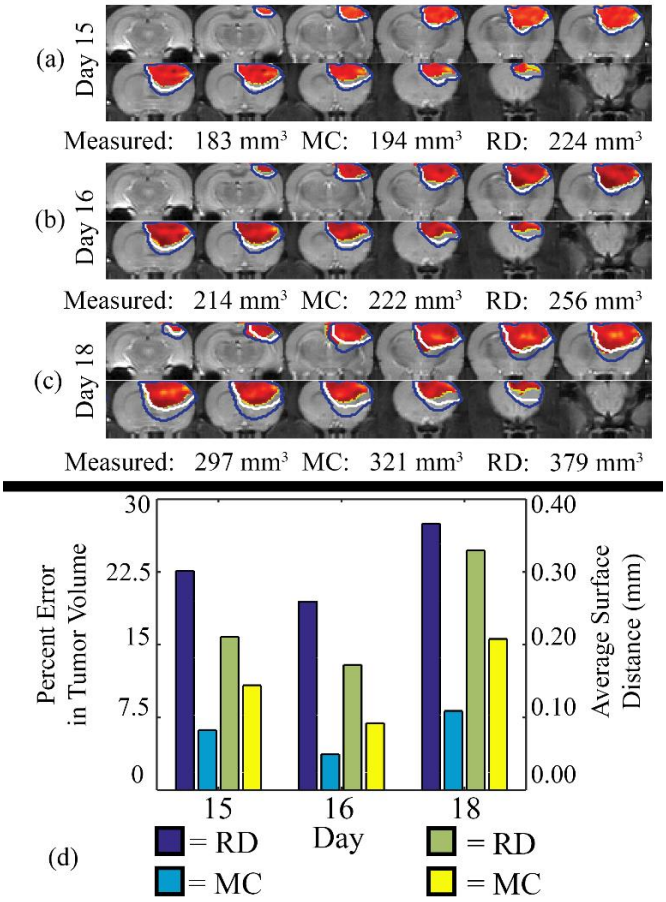

Figure 4.3. Global error analysis for the MC and RD models. Rows (a – c) shows $N_{meas}(\bar{x},t)$ with two outlines representing the simulated tumor spread for the $N_{RD}(\bar{x},t)$ (blue lines) and the $N_{MC}(\bar{x},t)$ (white lines) over the entire tumor volume at days 15, 16, and 18 for rat 7. The measured, MC, and RD tumor volume values for each day are displayed below each row. The MC model has less than 9% error at all time points, while the RD model has greater than 15% error at all prediction time points. Panel (d) quantifies rows (a – c) by showing the percent error in tumor volume (dark blue bars = RD; light blue bars = MC) and the ASD (green bars = RD; yellow bars = MC) at days 15, 16, and 18. The MC model exhibits lower global level error (decreased percent error in tumor volume and decreased ASD) compared to the RD model.

4.6.2 Voxel-Specific Carrying Capacity Model (CC)

Figure 4.4 shows the local error analysis for the CC model from the central tumor slice of rats 3, 7, and 10 on day 16. $N_{RD}(\bar{x},t)$, row (b), results in a more uniform distribution (by visual

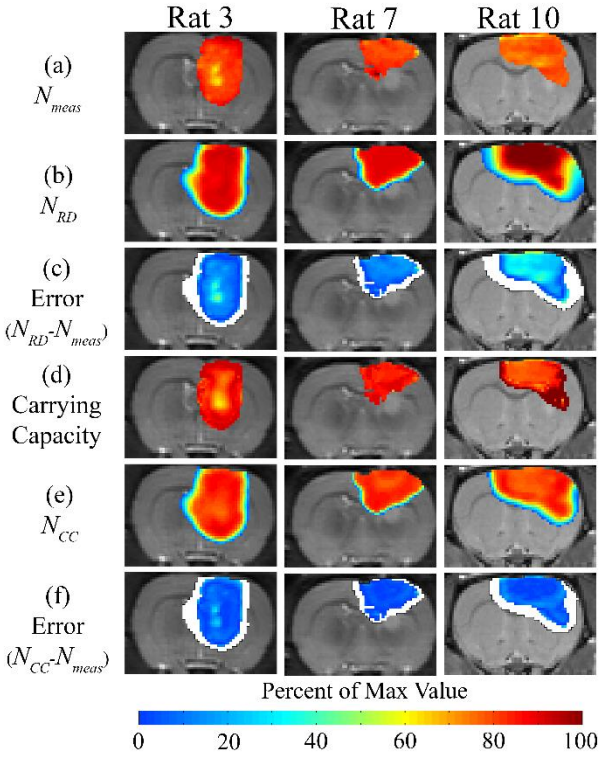

Figure 4.4. Local error analysis for the CC and RD models. $N_{meas}(\bar{x},t)$ is show in row (a), while the various model predictions of $N(\bar{x},t)$ are shown in rows (b – f) for the central tumor slice at the final imaging time point of three rats at day 16. The percent error between $N_{meas}(\bar{x},t)$ and $N_{model}(\bar{x},t)$ is shown in panels (c) and (f). The RD model, rows (b – c), poorly captures the intra-tumoral heterogeneity in $N_{meas}(\bar{x},t)$; row (c) shows a high error (greater than 40%) for all rats. In comparison, the CC model, rows (d – f), better describes the intra-tumoral heterogeneity in $N_{meas}(\bar{x},t)$. Row (d) shows the fitted carrying capacity map which is used in the finite difference simulation to obtain $N_{CC}(\bar{x},t)$, row (e). Reduced error (less than 20%) is observed in $N_{CC}(\bar{x},t)$, row (f), compared to $N_{RD}(\bar{x},t)$, row (c).

inspection) of tumor cells in comparison to what is observed *in vivo*, row (a). Row (c) shows elevated errors in areas corresponding to low $N_{meas}(\bar{x},t)$ for rats 3, 7, and 10 (13.27 ± 0.87%, 8.46 ± 0.70%, and 23.10 ± 1.17 %, respectively). Lower cellularity regions in $N_{meas}(\bar{x},t)$ are reflected in the fitted carrying capacity, row (d). The predictions of the CC model, row (e), resulted in less uniform distributions of tumor cells compared to N_{RD}. In particular, rat 3 captures some of the low cellularity regions observed in $N_{meas}(\bar{x},t)$. Rats 3, 7, and 10 showed reduced error 12.12 ± 0.90%; 5.08 ± 0.68%; 6.27 ± 0.51%, respectively) for the CC model, row (f), compared to the RD model, row (c).

Figure 4.5 compares the RD and CC models, along with $N_{meas}(\bar{x},t)$ at the local level. Panels (a – d) show the percent error in cell number as a function of the percent of maximum carrying capacity for the RD (red lines) and CC (blue lines) models. The results for rats 3, 7, and 10 are shown in panels (a – c), while the results for the entire cohort are shown in panel (d). Rat 3 in panel (a) shows significant differences ($p < 0.05$) between the RD and CC model (for $N_{meas}(\bar{x},t)/\theta < 0.95$) with the RD model resulting in a mean increase in error of 13.58% over the CC model. For rat 7, panel (b), the CC model resulted in a mean decrease in error of 6.09% compared to the RD model. Similarly, significant differences ($p < 0.05$) were observed between the RD and CC models for rat 10, where the RD model also resulted in a mean increase of 16.64% error compared to the CC model (panel c). The cohort results of panel (d) display a similar trend as the individual rats. Panels (a – d) show increased difference in percent error between the RD and CC curves between 60 and 70%. For the cohort, the CC model resulted in a mean decrease in

error of 7.48% compared to the RD model, panel (d). Panel (e) shows for a given cell value ($100\cdot\left(N_{meas}(\bar{x},t)/\theta\right)\%$) the percent of the total voxels within the tumor with that value for the RD, CC, and measured *N* (black lines) at day 16. The CC model more closely matches the *in vivo*

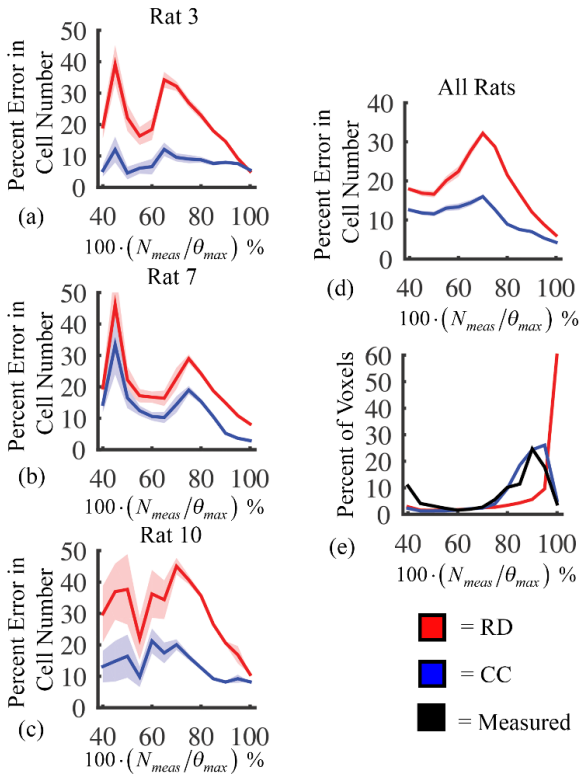

Figure 4.5. Local error comparison for RD and CC models. Panels (a – c) show the percent error in cell number (mean ± 95% CI) versus the voxel cell number as a percentage of the maximum carrying capacity for rats 3, 7, and 10 on day 16. The red lines represent the RD model, while the blue lines represent the CC model. The RD model has increased error at lower numbers (i.e., less than 80%). less than 80% of the carrying capacity), while the CC model has reduced error at all cell numbers. Panel (d) shows the results for the entire cohort. There are significant differences in the error distributions at each cell value. Panel (e) shows the distribution of cell number for the RD, CC, and measured *N* (black lines) at day 16.

model results in a distribution of $N_{RD}(\bar{x},t)$ with approximately 36% of its voxels with values less than 90% of the carrying capacity, whereas approximately 73% of the $N_{meas}(\bar{x},t)$ and $N_{CC}(\bar{x},t)$ voxels have values less than 90% of the carrying capacity.

4.6.3 Combined Model (MC-CC)

Figures 4.6 – 4.9 and Table 4.1 show the results of the global and local error analysis for the MC-CC model. Figure 4.6 shows the central slice of the tumor at each imaging time point for rat 1. Panel (a) shows the data used to estimate model parameters (i.e., $N_{meas}(\bar{x},t)$) and the T_2-weighted MRI anatomical image acquired at the same point. Row (b) shows $N_{meas}(\bar{x},t)$, while rows (c, e, g, j) show the predicted $N_{model}(\bar{x},t)$ from each model (RD, CC, MC, MC-CC, respectively.), and rows (d, f, h, k) show the percent error between $N_{meas}(\bar{x},t)$ and $N_{model}(\bar{x},t)$. The black outline on rows (c, e, g, j) represents the boundary of the measured tumor. At day 20, the RD and MC models (rows (c) and (h), respectively) both fail to capture the low cell density regions seen within $N_{meas}(\bar{x},t)$ resulting in high local level error (15.95 ± 0.89% and 18.38 ± 1.30%, respectively). Conversely, the CC and MC-CC models (rows (e) and (j, respectively) capture some low cellularity regions in $N_{meas}(\bar{x},t)$ resulting in decreased local level errors (7.96 ± 0.79% and 8.53 ± 1.01%, respectively). Increased error in cell number is observed in the center of the tumor (greater than 40%) compared to the periphery (less than 10%). All four models have low global level errors at day 15 (less than 16%). At days 18 and 20, however, the RD and CC models overestimate tumor growth (greater than 41) compared to the MC and MC-CC models

(less than 9%). Visually, it is evident that the MC-CC model combines the benefits of both the MC (low global level errors) and CC (low local level errors) models in predicting future tumor growth.

Panels (a – c) in Figure 4.7 show global and local errors applied to the complete tumor volume for rat 1, while panels (d – f) show the analogous analysis averaged over all rats on days 15, 16, 18, and 20. Panel (a) shows the percent error in tumor volume for the RD (dark blue bars), CC (light blue bars), MC (green bars), and MC-CC (yellow bars) models. Less than 9% error in tumor volume was observed for the mechanically coupled models (MC and MC-CC) at all time points, whereas the non-mechanically coupled models (RD and CC) had errors in tumor volume ranging from 13.42% to 84.12%. All models had low average surface distances less than 0.31 mm (displayed in panel (b)), at days 15 and 16. Conversely, on day 20 the RD and CC models had ASD's greater than 0.89 mm compared to the MC and MC-CC models which had ASD's less than 0.40 mm. The RD and MC models both had increased error ranging from 16.13% to 30.12% in voxel cell number, panel (c), compared to the CC and MC-CC models which ranged from 8.65 to 17.75%. Similar results are seen in the cohort panels (d – f). The non-mechanically coupled models resulted in increasing tumor volume error, panel (d), over time ranging from 16.08 to 50.37% whereas the mechanically coupled models had less than 10% error in tumor volume estimates. Similarly, panel (e) shows that the MC and MC-CC models both have decreased average surface distances ranging from 0.15 mm to 0.34 mm compared to the RD and CC models which ranged from 0.19 mm to 0.60 mm. Models with a voxel-specific carrying capacity (CC and MC-

CC models) reduced local level error, panel (f), from greater than 19.92% error (RD and MC models) to less than 14.94% error (CC and MC-CC models).

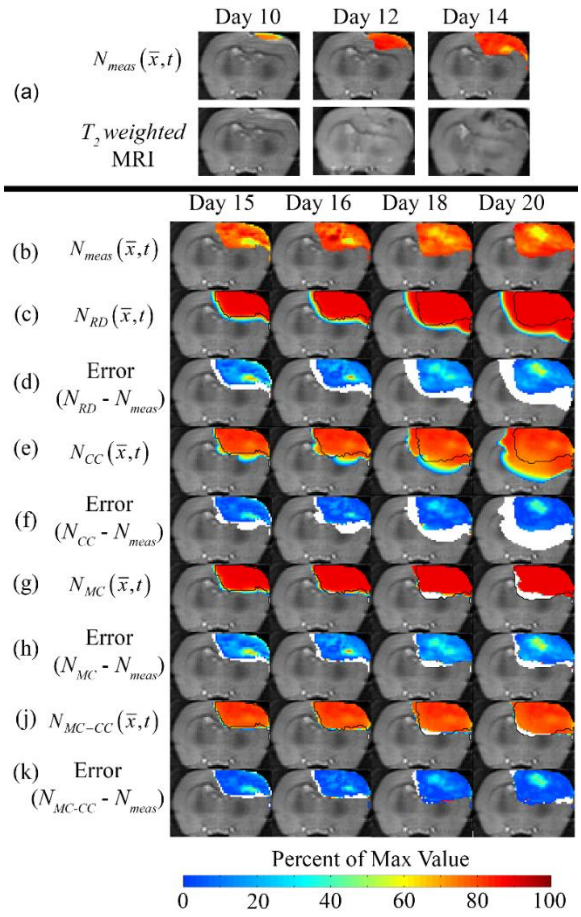

Figure 4.6. Comparison of the RD, CC, MC, and MC-CC model predictions for rat 1. Panel (a) shows the data used for parameter estimation ($N_{meas}(\bar{x},t)$) and the T_2-weighted MRI on days 10, 12, and 14. Rows (b – k) show $N_{meas}(\bar{x},t)$, $N_{RD}(\bar{x},t)$, $N_{CC}(\bar{x},t)$, $N_{MC}(\bar{x},t)$, $N_{MC-CC}(\bar{x},t)$, and the percent error between $N_{meas}(\bar{x},t)$ and the model predictions at days 15, 16, 18, and 20, respectively. The black outlines on rows (c, e, g, j) represent the boundaries of $N_{meas}(\bar{x},t)$, whereas the white space on rows (d, f, h, k) represent areas where $N_{meas}(\bar{x},t)$ was equal to zero. The RD model, rows (c – d), overestimates tumor size and fails to depict low cellularity regions within the tumor. The CC model, rows (e – f), also overestimates tumor size but it has reduced errors in cellularity. The MC model, rows (g – h), has reduced error in tumor size but has higher error compared to the CC model. Both the global and local errors are reduced in the MC-CC model, rows (j – k), compared to the RD model.

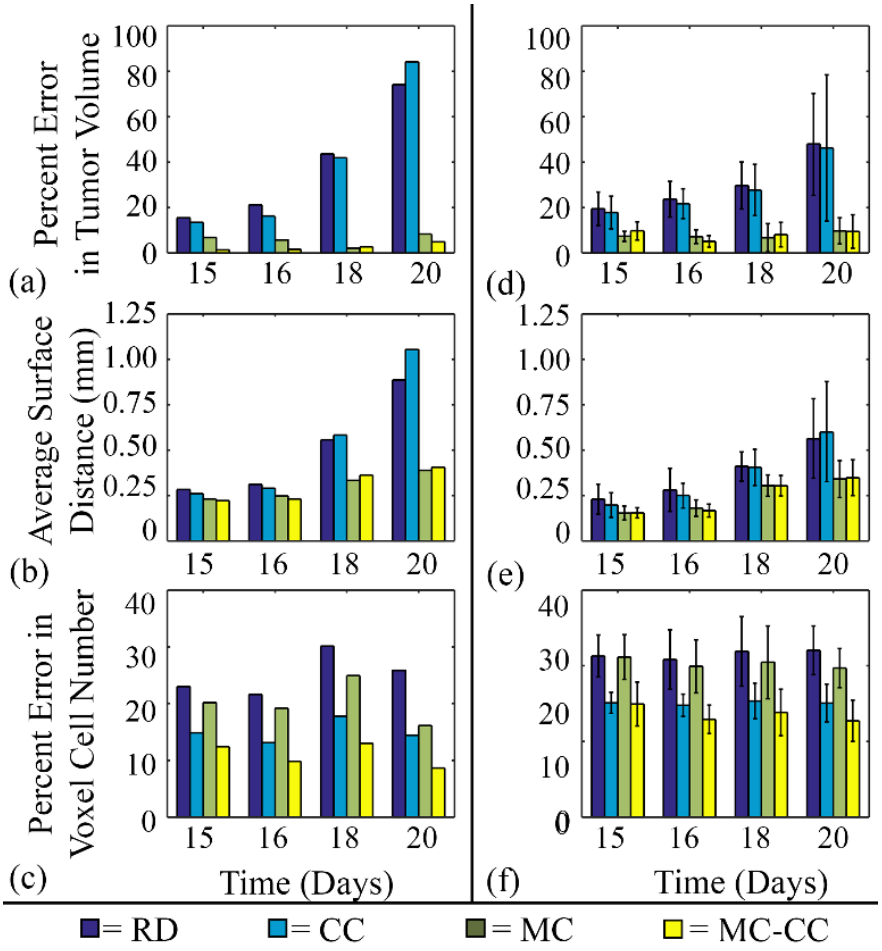

Figure 4.7. Global and local error results for all models. Percent error in tumor volume, panels (a,d), the average surface distance, panels (b,e), and the percent error in voxel cell number, panels (c,f), are shown for rat 1, panels (a – c), and all rats, panels (d – f). For rat 1, increased global level error, panels (a – b) is observed for the RD and CC models compared to the MC and MC-CC models. Similarly, increased local error is observed, panel (c), for the RD and MC models compared to the CC and MC-CC models. Similar results were observed for the cohort. The mean and 95% confidence interval are shown in panels (d – f). Increased error was observed in tumor volume, panel (d), for the RD and CC models (greater than 16%) compared to the MC and MC-CC models (less than 10%). Elevated average surface distances, panel (e), were also observed for the RD and CC models. Less than 12% error was observed at the local level, panel (f), for the CC and MC-CC models.

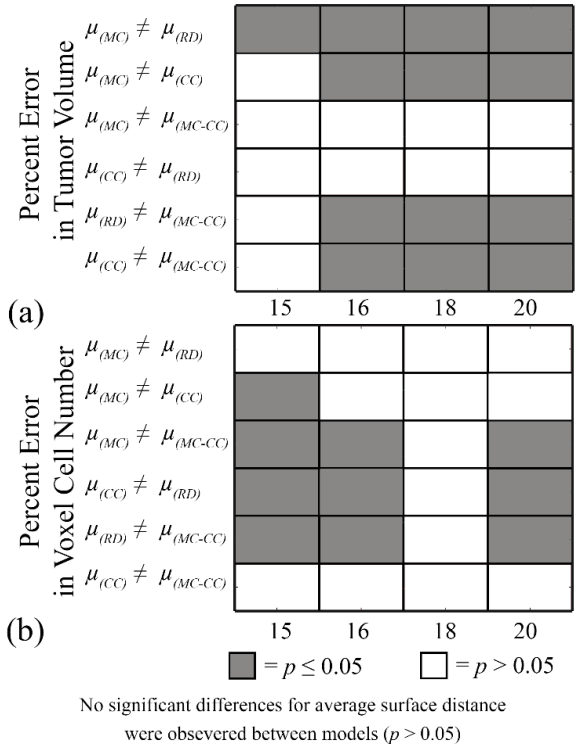

Figure 4.8. Results of the pairwise tests between model errors. Tukey's honest significant difference test was used to the null hypothesis that the mean of model A and model B (i.e., $\mu_{(MA)} = \mu_{(MB)}$) were equal. The alternative hypothesis is that means were not equal. Gray boxes represent statistically significant (i.e., $p < 0.05$) results at days 15, 16, 18, and 20 where the alternative hypothesis was accepted (vertical axis). The MC and MC-CC models resulted in a statistically significant decrease in percent error in tumor volume, panel (a), when compared to the RD and CC models. Similarly, the CC and MC-CC models had statistically significant decreases in local error, panel (b), at days 15, 16, and 20. No significant differences for the ASD was observed between models ($p > 0.05$) at any of the prediction time points.

Figure 4.8 shows the results of the pairwise testing following statistically significant ANOVA results ($p < 0.05$). Panel (a) shows that the MC and MC-CC models resulted in statistically significant (gray boxes) decrease in error in tumor volume at days 16-20 when compared to the RD and CC models (p ranged from 4.0×10^{-5} to 0.013). The MC model also had

a significant decrease in error in tumor volume at day 15 compared to the RD model (p = 0.018). Panel (b) shows statistically significant reductions in local error were observed for the CC and MC-CC models on days 15, 16 and 20 (p ranged from 2.5×10^{-4} to 0.043) when compared to the RD model. The ANOVA analysis indicated no significant differences between model values of ASD (p ranged from 0.168 to 0.429), therefore no pairwise comparisons were presented.

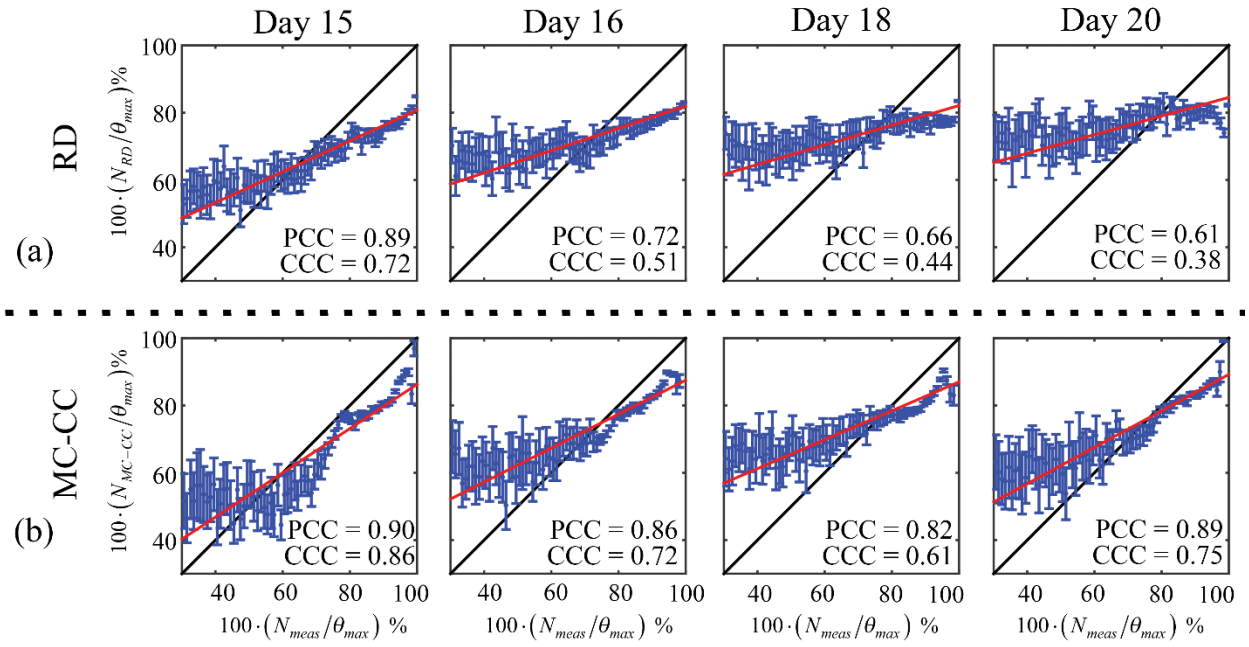

Figure 4.9. Comparison of model and measured voxel cell number for the RD and MC-CC models. Cell number as a percentage of the maximum carrying capacity for the RD, panel (a), and the MC-CC, panel(b), are plotted against the measured cell number as a percentage of the maximum carrying capacity on days 15, 16, 18, and 20. The blue dots represent the mean $N_{model}(\bar{x},t)$ and 95% confidence interval for a given $N_{meas}(\bar{x},t)$. The black line lines represent the line of unity, while the red lines represent the results of linear regression. The PCC and CCC for each model is reported within the plot. Both the RD and MC-CC showed a decreased level of agreement (CCC) and correlation (PCC) from day 15 to 20. The MC-CC model, however, had an increased level of agreement (at day 20; $CCC_{(MC\text{-}CC)}$ = 0.75 vs. CCC_{RD} = 0.38) and correlation (at day 20; $PCC_{(MC\text{-}CC)}$ = 0.89 vs. PCC_{RD} = 0.61) at all time points.

Figure 4.9 shows the PCC and CCC results for the RD and MC-CC models. Panel (a) shows a reduction in correlation and agreement between $N_{RD}(\bar{x},t)$ and $N_{meas}(\bar{x},t)$ from day 15 (PCC = 0.89, CCC = 0.72) to 20 (PCC = 0.61, CCC = 0.38). Panel (b) also shows decreased correlation and agreement between $N_{MC-CC}(\bar{x},t)$ and $N_{meas}(\bar{x},t)$ from day 15 (PCC = 0.90, CCC = 0.86) to 20 (PCC = 0.89, CCC = 0.75). The MC-CC model resulted in an increased level of agreement and correlation at all time points compared to the RD model. Most notably the MC-CC model showed higher agreement (closer to the line of unity) in between 80% and 90% of the carrying capacity. Table 4.1 reports the results of the linear regression (red lines in Figure 4.9).

Table 4.1. Linear Regression Results

Day	RD		MC-CC	
	Slope	Intercept	Slope	Intercept
15	0.469	34.9	0.545	27.0
16	0.331	48.8	0.394	42.6
18	0.292	52.9	0.334	49.3
20	0.277	56.9	0.413	41.8

4.7 Discussion

The results of the model analysis showed that global error can be significantly improved by coupling local tissue stress to tumor cell diffusion and that local error can be improved by fitting

for a voxel-specific carrying capacity. Global error analysis showed that the mechanically coupled models (MC, MC-CC) were significantly more accurate in describing tumor volume than the RD and CC model. Generally, global level error for the mechanically (MC, MC-CC) remained relatively constant from days 15 – 20 compared to the non-mechanically coupled models (RD, CC) which grew from day 15 to day 20. This suggests that the mechanically coupled model could potentially provide better global level predictions past day 20 compared to the non-mechanically coupled models. The local level analysis showed that incorporating a voxel-specific carrying capacity (CC, MC-CC) reduced local level error compared to when a global value was used (RD, MC). The MC-CC model benefits from both a reduced global level error (lower error in tumor volume, lower ASD) provided by the MC component of the model and reduced local level error (less error in local cell number) provided by the CC component of the model. Additionally, a strong level of agreement and correlation, compared to the RD model, was observed between the MC-CC model and measured cell number at the voxel-level.

Mechanical forces play a critical role in the growth of tumors [147,159] and the interaction with these forces needs to be considered in the development of accurate mathematical models. In this work, we incorporated the inhibitory role of local mechanical stress on gross tumor growth [109]. Without mechanical coupling, error in predicted tumor volume worsens over time (increasing approximately three-fold from day 15 to 20). The results of this model analysis, suggested that incorporating a mechanically coupled D is critical to accurately predicting gross tumor growth. It results in significant decreases in global level error (percent error in tumor

volume) when compared to the RD model. Furthermore, the gross inhibitory effect of local tissue stress observed modeled here accurately describes *in vivo* C6 glioma growth.

One of the limitations of this current study, is that the shear modulus was uniquely assigned to only a few identifiable regions. While this current approach still results in reduced global level errors due to inhibitory effect of the MC model [147], a more tissue-specific approach could potentially more accurately describe glioma morphology [168]. More accurate assignment of these tissue-specific properties (*via*, for example, high spatial resolution imaging data) after tumor implantation [169] may improve the predictions of future tumor morphology.

Mathematically modeling cell interactions at the local level is a large field [12,162,170–173] with complexity ranging from a single equation to models with several coupled equations. However, parameterizing these models in a subject/tumor-specific approach often would require highly invasive measurements to accurately capture the *in vivo* behavior. In this work, a simple alteration of the RD model to include a voxel-specific carrying capacity resulted in reduced local level errors. For the RD and MC models θ is based on voxel dimension and average tumor cell size. In the CC model the voxel-specific $\theta(\overline{x})$ is, in essence, a snapshot of the cumulative effects of both physical restrictions and environmental limitations. The analysis of the CC model suggests that it is significantly better at describing *in vivo* C6 glioma behavior. The CC model allows for changes in existing low cell-density regions to be more accurately described (Figure 4.4). Furthermore, the CC model is significantly more accurate in capturing the cell number distribution (Figure 4.5, panel (e)) observed *in vivo*. The CC model does, however, fail to capture expanding

low cellularity regions as seen in Figure 4.6 which is one of the main limitations to this model. Since $\theta(\bar{x})$ is temporally constant, which if it is a function of physical and environmental limitations may not be accurate, higher error may be observed in future predictions if necrotic regions develop. The CC model provides improved local level error for voxels where $N_{meas}(\bar{x},t)$ remains close to $\theta(\bar{x})$ over time. However, in voxels where $N_{meas}(\bar{x},t)$ is decreasing overtime (potentially to necrosis) we would have worsening error as $N_{meas}(\bar{x},t)$ continues to decrease. One potential solution is to develop a more complicated and explicit relationship between θ and physical limitations (vasculature space [151,162], edema [121], non-tumor cells [108]) and environmental limitations (availability of glucose and oxygen [12], acidity [108]) that could be evolved temporally as these conditions change. However, it is important to note that such modifications would likely require additional model assumptions and parameters that need additional data sources to define. A second limitation of the CC model is that it requires two sets of voxel-specific parameters ($k(\bar{x})$ and $\theta(\bar{x})$) and two global parameters (D for white and gray matter) which may be challenging to accurately estimate in a data limited situation.

The combined model, MC-CC, provides the best description of the *in vivo* C6 glioma growth by reducing both global and local level errors. The MC-CC model also shows a very high level of agreement and correlation to the *in vivo* observed cell number. Furthermore, statistically significant differences between the RD and MC-CC model were observed for both the global and local level metrics. As is, this model could be used as an accurate individualized control against which novel treatments or treatment schedules could be evaluated. Alternatively, this model may

provide a strong foundation upon which models describing response to radiotherapy or chemotherapy could be built.

4.8 Conclusion

The standard RD model poorly predicts the spatio-temporal evolution of *in vivo* C6 glioma growth in rats resulting in high global and local level errors. It is difficult to compare across the results in Figures 4.6d, 4.6f, 4.6h, 4.6k, and 4.7 without coming to the conclusion that mechanically coupling local tissue stress to tumor cell movement is a fundamental requirement towards accurate tumor growth models. While more subtle, Figure 4.7f demonstrates that a voxel-specific carrying capacity is likely a necessary ingredient for improving local predictions of the cellular heterogeneity within tumors. Lastly, while we have captured these important effects, the lack of prediction of specific tumor-to-tissue infiltrative shape as expressed by the average surface distance awaits further investigation. Nevertheless, when the two modifications proposed herein are combined, the MC-CC model, we see that future tumor growth can be accurately predicted on a rat-specific basis. The MC-CC model provides a more complete description of *in vivo* C6 glioma growth in rats compared to the standard RD model.

4.9 Acknowledgements

The authors thank Dr. Zou Yue for performing the animal surgeries and Dr. Daniel C. Colvin for assistance with the image registration. This work was supported through funding from

the National Cancer Institute R01CA138599, R21CA169387, U01CA174706, R25CA092043, from the National Institute of Neurological Disorders and Stroke R01NS049251 and the Vanderbilt-Ingram Cancer Center Support Grant (NIH P30CA68485). We thank the Kleberg Foundation for the generous support of our institute's imaging program. ECR holds a Career Award from the BWF.

CHAPTER 5

BIOPHYSICAL MODELING OF *IN VIVO* GLIOMA GROWTH FOLLOWING WHOLE BRAIN RADIOTHERAPY

Aim 3: Develop a subject-specific model incorporating the effects of whole brain radiation therapy.

5.1 Introduction and Contribution of Study

This study focused on the development and evaluation of individualized biophysical models of glioma growth following radiotherapy. The models discussed within this chapter extend the mechanically coupled voxel-specific reaction diffusion model developed and evaluated in Chapter 4. Based on experimental tumor volume measurements, it was hypothesized that the standard linear quadratic model may inadequately capture the reduced post-radiotherapy growth rate and that an additional term altering tumor proliferation would be needed. This work investigated the ability of three models (i.e., instantaneous death, reduced proliferation, combined instantaneous death and reduced proliferation) to describe post-radiotherapy growth as well as predict post-radiotherapy growth. This work demonstrated that at the low dose (20 Gy) all three models provided low error fits to the *in vivo* tumor growth data, while at the higher dose (40 Gy) the combined death and reduced proliferation model had the lowest error. Similarly, the combined model had improved tumor volume predictions for the 20 Gy group, whereas all three models poorly predicted future tumor growth for the 40 Gy group. This was a novel study where post-

radiotherapy models describing tumor growth was compared to several imaging time points. Furthermore, the predictions of the models were directly compared to histological sections obtained after the final imaging session. The results of this study motivate the development of an improved model of radiotherapy response at high doses and represent an initial step towards model-based optimization of individualized radiotherapy plans. This manuscript is in preparation for submission to the *International Journal of Radiation Oncology Biology Physics*.

5.2 Abstract

Individualized biophysical models of response to radiotherapy that can accurately characterize tumor response would dramatically assist in the design and optimization of individual radiotherapy plans. Patient-specific radiotherapy dose plans and schedules could help prolong patient survival and reduce damage to normal tissue. Towards this goal, we have begun investigating a set of biophysical models based upon a mechanically coupled reaction diffusion model which describes post-radiotherapy tumor growth. Post-radiotherapy response is modeled using a cell death model (M_d), a reduced proliferation rate model (M_p), and cell death and reduced proliferation model (M_{dp}). To evaluate the how well the models fit and predict tumor growth, rats (n = 12) with C6 gliomas were imaged with diffusion-weighted magnetic resonance imaging (DW-MRI) and contrast enhanced MRI (CE-MRI) at seven time points over two weeks. Rats received either 20 or 40 Gy between the third and fourth imaging time point. DW-MRI was used to estimate tumor cell number within enhancing regions in CE-MRI data. Model parameters were first

estimated from the complete time course to test the accuracy and precision of the models fit to the data. We then used a subset of the measurements to evaluate how well the post-radiotherapy models can predict future tumor growth. Error was then assessed between the model estimated and observed tumor growth at the global (error in tumor volume, average surface distance) and local levels (error in voxel cell number). The M_{dp} model had the lowest fit error in tumor volume (less than 12%) for both the 20 and 40 Gy group compared to other models. Average voxel-level error ranged from 14 to 22% for all three model fits to the data for both treatment groups. The M_{dp} model also had low error in tumor volume predictions (less than 16%) for the 20 Gy group, while high error in tumor volume was observed for the 40 Gy group (greater than 22%). Higher voxel level error was observed for tumor growth predictions from the 40 Gy group (ranging from 17% to 24%) compared to the 20 Gy group (ranging from 13-19%).The results of this study indicate that while the M_{dp} model can accurately fit tumor volume measurements for both treatment groups, the M_{dp} model may provide lower error predictions for low radiation doses.

5.3 Introduction

Radiotherapy forms a crucial component of the standard-of-care (SOC) of several cancers treating over 52% of all cancer patients [86]. For glioblastoma multiforme patients, radiotherapy is typically administered following surgical resection to target the residual and inoperable cancer tissue [87]. Unfortunately, with the current SOC therapy nearly all glioblastoma patients have progressive disease 7 to 10 months following adjuvant treatment [2]. A current limitation in the

SOC for glioblastoma patients is that while dose plans account for variations in tumor size and location they do not account for the variations in response to radiotherapy between patients and within a patient's tumor. This limitation may result in inadequately treating an individual tumor or unnecessarily irradiating large volumes of normal brain tissue. The quality of radiotherapy received may be improved through biophysical models of tumor growth and response. Biophysical models which can be individualized on a patient-specific [16] basic could be used to develop and optimize novel radiotherapy plans to maximize tumor death and minimize exposure to healthy tissue. Several groups have studied including patient-specific imaging information into biophysical models of tumor growth [19,20,26–28,63,73,114,151], and recently these models have begun to include response to radiotherapy.

Response to radiation therapy is commonly modeled using the linear quadratic (LQ) model, Eq. (5.1):

$$p(survival) = \exp(-\alpha \cdot dose - \beta \cdot dose^2) \ , \tag{5.1}$$

where the probability of survival is a function of radiosensitivity parameters α and β and dose. A common biological interpretation of the LQ model posits that the linear portion of the LQ model describes cells that receive lethal lesions (i.e., non-repairable) after a single hit, while the quadratic portion represents cells that have potentially lethal lesions (i.e., repairable lesions) following a single hit [81]. Cells that receive potentially lethal lesions may either successfully repair damage (viable cells) or unsuccessfully repair lesions (non-viable cells). The LQ model (and variations of

it) is fundamental to the design of therapy dose schedules, calculating lethality for different dose or fraction plans, and comparing the efficacy of different dose schedules [174,175]. For example, the radiosensitivity parameters for the target and non-target tissue can be used to determine the dose and dose schedule that minimizes damage to healthy tissue while controlling tumor growth.

The LQ model has recently been incorporated into several mathematical models of radiotherapy response and planning [119–123,176] that use medical imaging data (MRI, computed tomography, positron emission tomography) to initialize and constrain patient-specific tumor simulations [16]. Medical imaging information is used to determine tumor size, tumor position, and estimate patient-specific model parameters. One such model by Rockne *et al* [119,120] utilizes post-contrast T_1 weighted MRI and T_2 weighted MRI data acquired prior to the start of treatment to estimate untreated tumor growth kinetics (*i.e.*, tumor cell diffusion coefficient and tumor cell proliferation rate). Tumor cell death is then modeled using the LQ model for cell survival. For a given α and β, the optimal dose and dose delivery schedule can be determined and the effects on tumor growth simulated. Alternatively, a post-radiotherapy imaging time point can be used to determine a patient's radiosensitivity (α and β). Since Rockne *et al's* approach includes data at the conclusion of radiotherapy to estimate a patient's radiosensitivity this model cannot be used to adapt radiotherapy during the course of treatment. More recently, Corwin *et al* [122] expanded upon Rockne *et al*'s model to demonstrate a proof-of-concept approach to developing individualized intensity-modulated radiation therapy plans. Tumor volumes, growth kinetics, and radiosensitivity parameters estimated from patient data were used in a simulation to determine the

optimal radiation therapy plan. The simulated optimized plans had a decreased exposure to normal tissue and increased time to progression by 21% to 105% compare to the simulated SOC. An alternative approach discussed in Bondiau *et al* [124] focused on reducing the ambiguity in irradiation margins by simulating the non-detectable spread of glioblastoma growth. Bondiau *et al*'s model indicated that the conventional 2 cm margins may result in greater than 53% of the irradiated volume being healthy tissue while inadequately irradiating up to 15% of the total tumor volume. While these current patient-specific radiotherapy models demonstrate the potential value modeling has to clinical radiation therapy, the accuracy and precision of these modeling approaches need to be validated with *in vivo* experiments. Towards this end, *in vivo* imaging measurements and histological sections are used in this study to assess the model fit and prediction error of three models of response to radiotherapy.

In this work, the effects of radiotherapy are modeled as cell death immediately after radiation therapy, a reduction of proliferation rate post-radiotherapy, and the combination of cell death and reduced proliferation rate. The cell death, or M_d, model is related to the classic LQ model resulting in immediate cell death; that is, following irradiation some fraction of the cells lose their clonogenic survival eventually resulting in predominantly apoptosis or necrosis. The M_d model assumes that the effect of radiotherapy (i.e., cell death) occurs over a relatively short period. The reduced proliferation model, or M_p, model assumes that consequences of irradiation predominantly results in a reduced net proliferation of tumor cells. A dose dependent reduction in proliferation rate has been observed in the C6 line [177] and may be the result of cell cycle arrests [178] or

senescence. The M_p model, however, assumes that the effect of radiotherapy (i.e., reduced proliferation) is a long term alteration of growth kinetics. The combined, or M_{dp}, model incorporates the effects of both reduced proliferation and cell death to model post-radiotherapy growth providing a balance between the short and long term effects of radiotherapy.

In this contribution, we evaluate the ability of the M_d, M_p, and M_{dp} models to predict the *in vivo* spatio-temporal development of C6 glioma growth following radiation therapy. DW-MRI and CE-MRI data acquired before and after radiotherapy are used to estimate rat-specific model parameters. The rat-specific model parameters are then used to simulate the post-treatment spatial-temporal tumor evolution. The model fit error of the M_d, M_p, and M_{dp} models is evaluated by assessing the error between the simulated and measured cell density at the post-radiotherapy time points. The simulated tumor growth is then also compared to post-mortem histological analysis. The prediction error of the M_d, M_p, and M_{dp} models is evaluated by simulating future tumor growth using model parameters estimated from a subset of the imaging time points and assessing the error between simulated and measured cell density.

5.4 Methods

5.4.1 Biophysical Models of Tumor Growth

In this study, tumor cell growth is modeled using a reaction diffusion type which describes the change in the distribution and number of tumor cells due to the random movement of tumor

cells (diffusion; first term on the right hand side of Eq. (5.2)), the proliferation of cells (reaction, second term on the right hand side) , and the death of cells due to radiotherapy (third term on right hand side):

$$\frac{\partial N(\bar{x},t)}{\partial t} = \nabla \bullet \left[\theta_{max} D(\bar{x},t) \nabla \left(\frac{N(\bar{x},t)}{\theta(\bar{x})} \right) \right] + k_p(\bar{x}) \cdot RT_p(t) \cdot N(\bar{x},t) \left(1 - \frac{N(\bar{x},t)}{\theta(\bar{x})} \right) - RT_d(t) \cdot N(\bar{x},t) \left(1 - \frac{N(\bar{x},t)}{\theta(\bar{x})} \right), \quad (5.2)$$

where the number of tumor cells at three-dimensional position $\bar{x}$ and time t is $N(\bar{x},t)$, the mechanically coupled tumor cell diffusion coefficient is $D(\bar{x},t)$, the voxel-specific carrying capacity is represented by $\theta(\bar{x})$, $k_p(\bar{x})$ is a voxel-specific proliferation rate, $RT_p(t)$ is a post-radiotherapy proliferation function, and $RT_d(t)$ is a post-radiotherapy death function. $D(\bar{x},t)$ is mechanically coupled to local tissue stress [147,163], Eq. (5.3):

$$D(\bar{x},t) = D_0 \cdot e^{-\lambda_1 \cdot \sigma_{vm}(\bar{x},t)}, \quad (5.3)$$

where D_0 is the tumor cell diffusion coefficient in the absence of mechanical properties, λ_1 is an empirically derived stress-tumor cell diffusion coupling constant, and $\sigma_{vm}(\bar{x},t)$ is the von Mises stress. As a result, as local tissue stress increases tumor cell movement will be inhibited by a decrease in $D(\bar{x},t)$. $\sigma_{vm}(\bar{x},t)$, is first determined by calculating the tissue displacement ($\vec{u}$) caused by the expanding tumor using a linear elastic isotropic mechanical equilibrium equation, Eq. (5.4):

$$\nabla \cdot G\nabla\vec{u} + \nabla \frac{G}{1-2\nu}\left(\nabla \cdot \vec{u}\right) - \lambda_2 \nabla N(\bar{x},t) = 0 \ , \tag{5.4}$$

where G is the shear modulus, ν is Poisson's ratio, and λ_2 represents a tumor cell force coupling constant. The gradient of $\vec{u}$ is then calculated to obtain the shear and normal strains. Eq. (4.4), shows the normal (ε_{xx}) and shear (ε_{xy} and ε_{xz}) strains calculated from the displacement map in the x-direction (u_x):

$$\begin{bmatrix} \varepsilon_{xx} \\ \varepsilon_{xy} \\ \varepsilon_{xz} \end{bmatrix} = \begin{bmatrix} \partial u_x/\partial x \\ \partial u_x/\partial y \\ \partial u_x/\partial z \end{bmatrix} , \tag{5.5}$$

similar calculations are repeated in the y- and z-directions. The principal normal stresses are then calculated using Eq. (4.5) :

$$\begin{bmatrix} \sigma_{xx} \\ \sigma_{yy} \\ \sigma_{zz} \end{bmatrix} = \left(\frac{2G\nu}{1-2\nu}\right)\left(\varepsilon_{xx} + \varepsilon_{yy} + \varepsilon_{zz}\right) + 2G \begin{bmatrix} \varepsilon_{xx} \\ \varepsilon_{yy} \\ \varepsilon_{zz} \end{bmatrix} . \tag{5.6}$$

The principal shear stresses are calculated using Eq. (4.6):

$$\begin{bmatrix} \sigma_{xy} \\ \sigma_{xz} \\ \sigma_{yz} \end{bmatrix} = G \begin{bmatrix} \varepsilon_{xy} \\ \varepsilon_{xz} \\ \varepsilon_{yz} \end{bmatrix} . \tag{5.7}$$

The principal normal and shear stresses that are used to calculate $\sigma_{vm}(\bar{x},t)$ using Eq. (5.8):

$$\sigma_{vm} = \left[\frac{1}{2} \left(\begin{array}{c} \left(\sigma_{xx} - \sigma_{yy}\right)^2 + \left(\sigma_{xx} - \sigma_{zz}\right)^2 + \left(\sigma_{zz} - \sigma_{yy}\right)^2 \\ + 6\left(\sigma_{xy}2 + \sigma_{yz}2 + \sigma_{xz}2\right) \end{array} \right) \right]^{1/2} . \quad (5.8)$$

The reduced post-radiotherapy proliferation function, $RT_p(t)$, is represented by a piecewise function, Eq. (5.9):

$$RT_p(t) = \begin{cases} k_{p,rt} & t \geq t_{rt} \\ 1 & t < t_{rt} \end{cases} , \quad (5.9)$$

where $k_{p,rt}$ is a reduced proliferation rate, and t_{rt} is the time that radiotherapy started. The post-radiotherapy proliferation function results in a decreased overall proliferation rate that may arise due to a reduced number of actively proliferating cells, slowed proliferation rate due to temporary blocks in cell-cycle, and/or senescence. Similarly, the post-radiotherapy death function $RT_d(t)$, is also represented by a piecewise function, Eq. (5.10):

$$RT_d(t) = \begin{cases} k_{d,rt} & t = t_{rt} \\ 0 & t \neq t_{rt} \end{cases} , \quad (5.10)$$

where $k_{d,rt}$ is the post-radiotherapy death rate. The post-radiotherapy death function represents cell death that occurs relatively shortly after radiotherapy, potentially due to the activation of the apoptosis pathway by the DNA damage response mechanism or early mitotic deaths due to misrepair of DNA damage.

Both untreated and post-treatment tumor growth is modeled using Eq. (5.2). Untreated tumor growth is modeled (or the M_{ut} model) by setting $k_{p,rt}$ equal to 1 and $k_{d,rt}$ equal to 0. Post-treatment tumor growth is modeled using three variations of Eq. (5.2) which characterize the effect of radiotherapy as instantaneous death (M_d: $k_{d,rt} > 0$, $k_{p,rt} = 1$), reduced tumor cell proliferation (M_p: $0 < k_{p,rt} < 1$, $k_{d,rt} = 0$), and both instantaneous death and reduced tumor cell proliferation (M_{dp}: $0 < k_{p,rt} < 1$, $k_{d,rt} > 0$). Measurements from DW-MRI are used to provide estimates of $N(\bar{x},t)$ at several time points before and after radiotherapy [72,74]. Pre-treatment measurements of $N(\bar{x},t)$ are used to solve an inverse problem of the M_{ut} model to return estimates of D_0, $\theta(\bar{x})$, and $k_p(\bar{x})$. Similarly, post-treatment measurements of $N(\bar{x},t)$ are used to solve a set of inverse problems for the M_d, M_p, and M_{dp} models to return estimates of $k_{d,rt}$ (M_d and M_{dp} models) and $k_{p,rt}$ (M_p and M_{dp} models). The simulated distribution of tumor cells for the different models are $N_{ut}(\bar{x},t)$ for the M_{ut} model, $N_d(\bar{x},t)$ for the M_d model, $N_p(\bar{x},t)$ for the M_p model, and $N_{dp}(\bar{x},t)$ for the M_{dp} model. The finite difference method was used to solve Eq. (5.2) using a three dimension in space (Δx = 250 μm, Δy = 250 μm, Δz = 1000 μm) and fully explicit in time (time step = 0.01 days) simulation. The finite difference simulation was written in Matlab (Mathworks, Natick, MA) and $N(\bar{x},t)$ had no diffusive flux at the brain tissue boundaries. (Appendices A and C provide further details on the finite difference implementation of Eq. (5.2) and Eq. (5.4).)

5.4.2 In Vivo Experiments

The experimental procedures were approved by the Vanderbilt University Institutional Animal Care and Use Committee. Rats were anesthetized with 2% isoflurane in 98% oxygen for all imaging, surgical, and irradiation procedures. Twelve Female Wistar rats (mean ± 95% confidence interval, 257 ± 9 g) were anesthetized and inoculated intracranially with C6 glioma cells (1×10^5) *via* stereotaxic injection on day 0. On day 8, permanent jugular catheters were placed in each rat for injection of an MRI contrast agents. Rats were then imaged on days 10 (t_1), 12 (t_2), and 14 (t_3) with MRI prior to receiving radiotherapy on day 14.5 (t_{rt}). Following radiotherapy, rats were imaged with MRI an additional four times on days 16.5 (t_4), 18.5 (t_5), 20.5 (t_6), and 22.5 (t_7). During each MRI procedure, rat body temperature was maintained near 37° C by a flow of warm air directed over the animal and respiration was monitored using a pneumatic pillow.

MR imaging experiments were performed on a 9.4 T horizontal-bore magnet (Agilent, Santa Clara, CA, USA) using a 38 mm diameter Litz quadrature coil (Doty Scientific, Columbia, SC, USA) at the Vanderbilt University Institute of Imaging Science. MR images were acquired over a $32 \times 32 \times 16$ mm^3 field of view sampled with a $128 \times 128 \times 16$ matrix. At the beginning of the second through the final imaging session, a mutual information based rigid registration algorithm [74,134] was used at the scanner to register the current imaging time point to the initial imaging session (day 10). (Appendix B provides further details on the image registration process.)

DW-MRI data was acquired using a pulsed fast spin echo diffusion sequence with three orthogonal diffusion encoding directions with *b*-values of 150, 500, and 1000 s/mm^2, Δ/δ = 25 ms/2 ms, and 16 averaged excitations. The DW-MRI data was then used to estimate the *apparent* diffusion coefficient (ADC) on a voxel basis using standard methods [135]. The ADC was used to estimated $N(\bar{x},t)$ [65,66,72] using Eq. (5.11) at all imaging time points:

$$N\left(\bar{x},t\right)=\theta_{max}\left(\frac{ADC_w-ADC\left(\bar{x},t\right)}{ADC_w-ADC_{min}}\right), \tag{5.11}$$

where θ_{max} represents the tumor cell carrying capacity for an imaging voxel, *ADCw* is the ADC of free water at 37° C (2.5 × 10^{-3} mm^2/s) [135], $ADC(\bar{x},t)$ is the ADC value at position $\bar{x}$ and time *t*, and ADC_{min} is the minimum ADC value which corresponds to the voxel with the largest number of cells. θ_{max} represents the physical limitation to the number of cells that can fit within an imaging voxel assuming spherical tumor cells with a packing density of 0.7405 [136] and an average cell volume of 908 μm^3 [137].

Tissue T_1 was estimated using an inversion-recovery snapshot experiment with *TR*/*TE* = 5000/3 ms, *TI* (inversion time) = (8 *TI*s logarithmically spaced between 200 - 4000 ms), and two averaged excitations. A spoiled gradient echo sequence with *TR*/*TE* = 45/1.4 ms, two averaged excitations, and a flip angle = 20° was used for the CE-MRI experiment. For the CE-MRI experiment, images were collected before and then following the injection of a 200 μL bolus (0.05 mmol kg^{-1}) of gadolinium-diethylenetriamine pentaacetic acid (Gado-DTPA^{TM}, BioPhysics Assay Laboratory, Worcester, MA) through the jugular catheter.

Rats received radiotherapy following their third imaging time point on day 14.5 (t_{rt}). Rats were irradiated with 20 Gy (n = 5) or 40 Gy (n = 8) with a Therapax DXT 300 x-ray machine (Pantak Inc., East Haven, CT, USA) delivering 2.13 Gy/min. During the irradiation, protocol rats were shielded with lead blocks to minimize exposure outside of the brain.

5.4.3 Tumor and Tissue Segmentation

T_1 maps and CE-MRI data were used to segment brain tissue and identify regions of interest. T_1 maps were used to identify specific white and gray matter regions (i.e., cortex, corpus callosum, hippocampus, thalamus, and putamen). Tumor regions-of-interest (ROIs) were identified using the difference between pre-contrast and post-contrast CE-MRI data. The measured tumor cell distribution at each time point, $N_{meas}(\bar{x},t)$, was then calculated within these tumor ROIs using the ADC measurements and Eq. (5.11).

5.4.4 Parameter Estimation and Forward Evaluation

Figure 5.1 summarizes the parameter optimization and forward evaluation methods. In the following text and figures, the notation $t_a \rightarrow t_c$ is used to indicate time points t_a, t_c, and all time points between t_a and t_c. First, pre-treatment data ($N_{meas}(\bar{x},t_1 \rightarrow t_3)$) are used to estimate model parameters (D_0, $k_p(\bar{x})$, and $\theta(\bar{x})$), step (1) in panel (a), by minimizing the error between $N_{meas}(\bar{x},t_2 \rightarrow t_3)$ and $N_{ut}(\bar{x},t_2 \rightarrow t_3)$. A second optimization then occurs using post-treatment data t_4 through t_n ($t_n = t_7$ when all time points are used; $t_n < t_7$ when a subset of the total points are

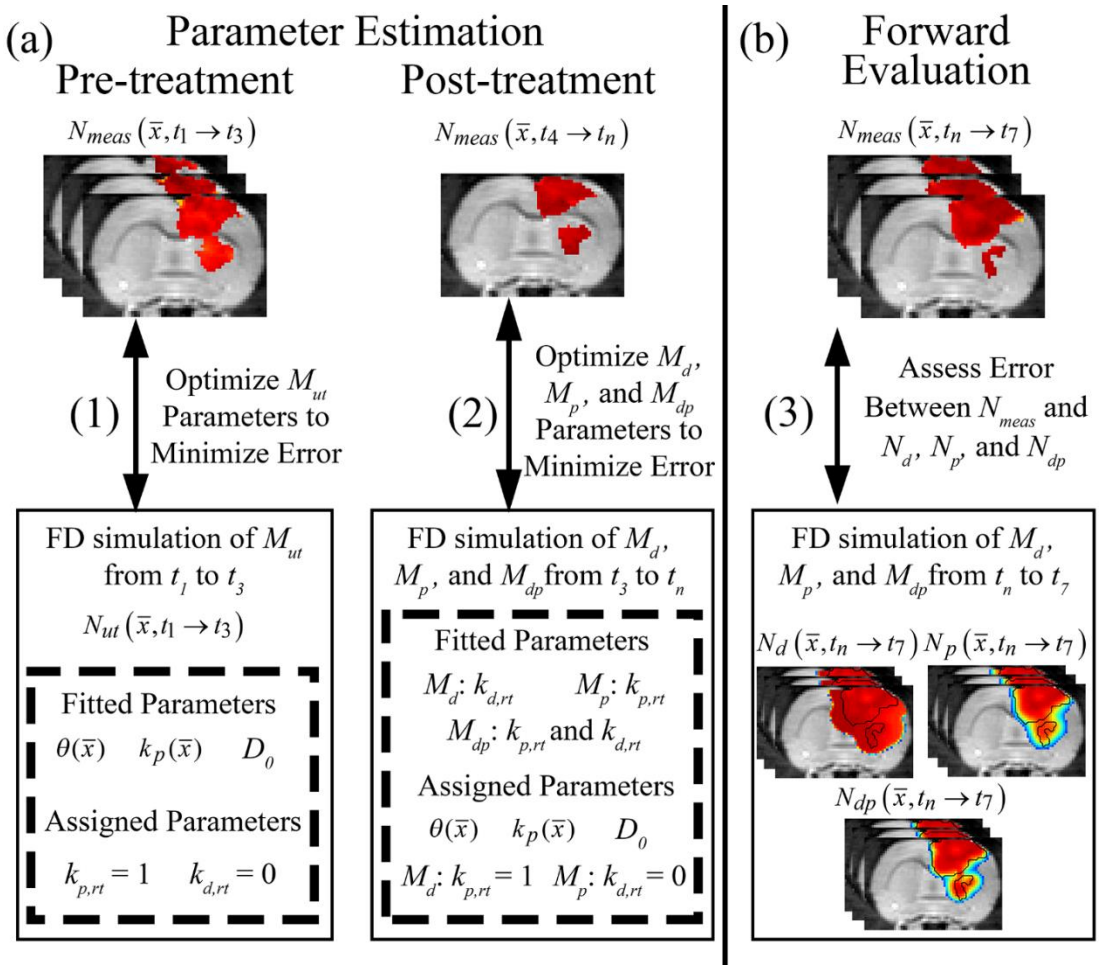

Figure 5.1. Parameter optimization and forward evaluation approach. Panel (a) shows the parameter estimation process for the pre-treatment and post-treatment models. Step (1): M_{ut} parameters ($k_p(\bar{x})$, $\theta(\bar{x})$, D_0) are estimated by minimizing the error between $N_{meas}(\bar{x}, t_2 \rightarrow t_3)$ and $N_{ut}(\bar{x}, t_2 \rightarrow t_3)$. Step (2): the post-treatment model parameters ($k_{p,rt}$ and $k_{d,rt}$) are estimated by minimizing the error between $N_{meas}(\bar{x}, t_4 \rightarrow t_n)$ and $N_{model}(\bar{x}, t_4 \rightarrow t_n)$. Step (3): Tumor growth is then simulated from t_n to t_7. Error is then assessed between $N_{meas}(\bar{x}, t_n \rightarrow t_7)$ and the post-treatment models $N_{model}(\bar{x}, t_n \rightarrow t_7)$.

used). The post-treatment optimization minimizes the error between $N_{meas}(\bar{x}, t_4 \rightarrow t_n)$ and the post-treatment models (e.g., $N_d(\bar{x}, t_4 \rightarrow t_n)$) to estimate $k_{p,rt}$ and $k_{d,rt}$. For the case when t_n is equal to t_7, error is assessed at the global and local levels between measured and model predicted N from

t_4 to t_7. When a subset of the total data is used (i.e., $\underline{t_n} < t_7$) the pre- and post-treatment parameters are then used in a final simulation of the post-treatment models from t_n to t_7, step (3) in panel (b). The simulated post-treatment data (i.e., $N_d(\bar{x}, t_n \rightarrow t_7)$, $N_p(\bar{x}, t_n \rightarrow t_7)$, and $N_{dp}(\bar{x}, t_n \rightarrow t_7)$) is compared to $N_{meas}(\bar{x}, t_n \rightarrow t_7)$ at the local and global levels.

A Levenberg-Marquardt weighted least squares optimization is used to estimate model parameters from $N_{meas}(\bar{x}, t)$. The optimal model parameters were determined when the objective function, Eq. (5.12), was minimized:

$$\sum_{t=t_i}^{t=t_f} \left(\left(\sum_{\bar{x}=1}^{\bar{x}_i=n} \left(N_{meas}(\bar{x}, t) \right) \right)^{-1} \cdot \left(\sum_{\bar{x}=1}^{\bar{x}=n} \left(N_{model}(\bar{x}, t) - N_{meas}(\bar{x}, t) \right)^2 \right) \right), \qquad (5.12)$$

where t_i is the initial time point used for optimization, t_f is the final time point used for optimization, and $N_{model}(\bar{x}, t)$ is the model value of $N(\bar{x}, t)$ using the current model parameter set. For M_{ut} t_i is equal to t_2 and t_f is equal to t_3, while t_i is equal to t_4 and t_f is equal to t_n for the M_d, M_p, and M_{dp} models. Prior to the start of the parameter optimization, a 3 × 3 Gaussian filter was applied to $N_{meas}(\bar{x}, t)$ to reduce the effects of noise within voxels. All parameters were constrained to non-negative values. $k_p(\bar{x})$ and $\theta(\bar{x})$ were estimated voxel-wise within the tumor ROI and assigned 0 (for $k_p(\bar{x})$) or the maximum value (for $\theta(\bar{x})$) elsewhere. Single values of D_0, $k_{p,rt}$, and $k_{d,rt}$ were estimated for all tumor cells.

After the optimization of both the pre-treatment and post-treatment model parameters, these values were then used in a FD simulation initialized at t_4 and "grown" to t_7. The simulated

tumor growth (N_d, N_p, and N_{dp}). Was then sampled at time points corresponding to the experimentally acquired imaging time points. As the tumor expanded into regions where $k_p(\bar{x})$ was not estimated, $k_p(\bar{x})$ was assigned using a local average of available non-zero *k's* within a 3 × 3 × 3 kernel.

5.4.5 Error Analysis

Error between the model (N_d, N_p, and N_{dp}) and measured (N_{meas}) tumor growth was assessed at a global level (percent error in tumor volume, average surface distance, normalized root mean square error) and local level (percent error in average cell number). To evaluate how well the model describes the data, we assessed error between the M_d, M_p, and M_{dp} models and the data at days t_4 through t_7. To evaluate how well the model predictions match measured data, we assessed error between the M_d, M_p, and M_{dp} models and the data from the final time point used in optimization, t_n, to t_7. The percent error in tumor volume was determined by calculating the percent difference between the model estimates of tumor volume and the measured tumor volume. The average surface distance (ASD) reports the average minimum distance between a voxel on the surface of the model tumor volume and a voxel on the surface of the measured tumor volume. The ASD is a measure of the agreement between model and measured ROI geometries. The normalized root mean square error (nRMS error) is used to assess the cumulative error in model tumor volume descriptions. At the local level, the percent difference in $N_{model}(\bar{x},t)$ and $N_{meas}(\bar{x},t)$ was calculated at the voxel level. All results are reported as the mean and 95% confidence interval

when appropriate. A 1-way analysis of variance (ANOVA) was used to evaluate the differences in global and local errors between the M_d, M_p, and M_{dp} within treatment groups. Tukey's honest significant difference test was then used for pair-wise comparisons. A p value less than 0.05 was considered significant.

5.4.6 Histological Validation

Error between the model (N_d, N_p, and N_{dp}) and measured (N_{meas}) tumor growth was assessed at a global level (percent error in tumor volume, average surface distance, normalized root mean square error) and local level (percent error in average cell number). To evaluate how well the model describes the data, we assessed error between the M_d, M_p, and M_{dp} models and the data at days t_4 through t_7. To evaluate how well the model predictions match measured data, we assessed error between the M_d, M_p, and M_{dp} models and the data from the final time point used in optimization, t_n, to t_7. The percent error in tumor volume was determined by calculating the percent difference between the model estimates of tumor volume and the measured tumor volume. The average surface distance (ASD) reports the average minimum distance between a voxel on the surface of the model tumor volume and a voxel on the surface of the measured tumor volume. The ASD is a measure of the agreement between model and measured ROI geometries. The normalized root mean square error (nRMS error) is used to assess the cumulative error in model tumor volume descriptions. At the local level, the percent difference in $N_{model}(\bar{x},t)$ and $N_{meas}(\bar{x},t)$ was calculated at the voxel level. All results are reported as the mean and 95% confidence interval

when appropriate. A 1-way analysis of variance (ANOVA) was used to evaluate the differences in global and local errors between the M_d, M_p, and M_{dp} within treatment groups. Tukey's honest significant difference test was then used for pair-wise comparisons. A p value less than 0.05 was considered significant.

5.5 Results

5.5.1 Experimental Measurements

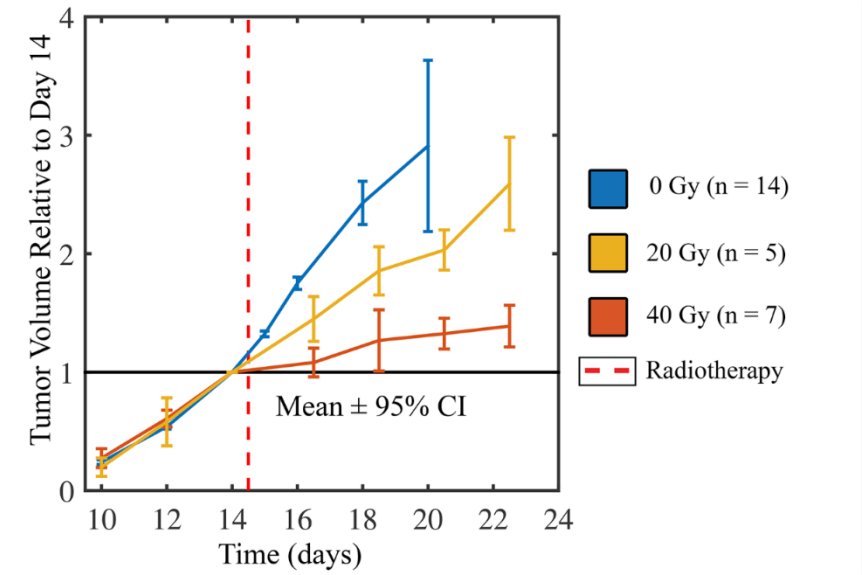

Figure 5.2. Measured tumor volume for untreated and treated rats. The mean and 95% confidence interval of tumor volume measurements relative to day 14 are shown for untreated rats (blue lines), rats receiving 20 Gy (yellow line), and rats receiving 40 Gy (orange line). The time of radiotherapy is indicated with a red dashed line. Both the 20 and 40 Gy rats have reduced tumor growth following radiotherapy.

Figure 5.2 shows the average tumor volume time course for the untreated and treated (20 Gy, 40 Gy) rats. Rapid tumor growth is observed in the untreated group which has an average doubling time of 3.8 ± 1.3 days. A reduced growth rate is observed following radiotherapy for the 20 Gy rat which has an average doubling time of 6.4 ± 1.0 days. The 40 Gy group had the lowest growth rate resulting in an average doubling time of 21.8 ± 8.4 days.

5.5.2 Model Fit Error

Figures 5.3-5.9 and Tables 5.1-5.2 show the results of the model analysis for rats receiving radiotherapy. Figure 5.3 shows the central slice for a representative rat from the 20 Gy group. The data used to estimate model parameters ($N_{meas}(\bar{x}, t_1 \rightarrow t_7)$) are shown in rows (a) and (c), while the model distributions of cell number ($N_{model}(\bar{x}, t_4 \rightarrow t_7)$) are shown for the M_d, M_p, and M_{dp} models, respectively, in rows (c, f, h). The error between the measured and model estimates of N are shown in rows (e, g, i). The M_d model (row (d)) overestimates tumor size (greater than 21% error) on t_7 compared to the M_p and M_{dp} models (less than 12% error, rows (f, h)). The M_p and M_{dp} model had statistically significant lower voxel-wise error at t_4 (7.56 ± 0.94% and 9.18 ± 1.36%, respectively) compared to the M_d model (17.24 ± 3.02%). The average voxel-wise error was below 15% for all three models on t_5 and t_6, while on t_7 the M_d model had statistically significant lower error (14.40 ± 1.95%) compared to the M_p and M_{dp} models (23.18 ± 2.72% and 22.04 ± 2.80%, respectively). All models fail to capture the developing low cell density region on days t_4 through t_7 (row (c), resulting in high error (greater than 50%) in these regions (rows (e, h, i)).

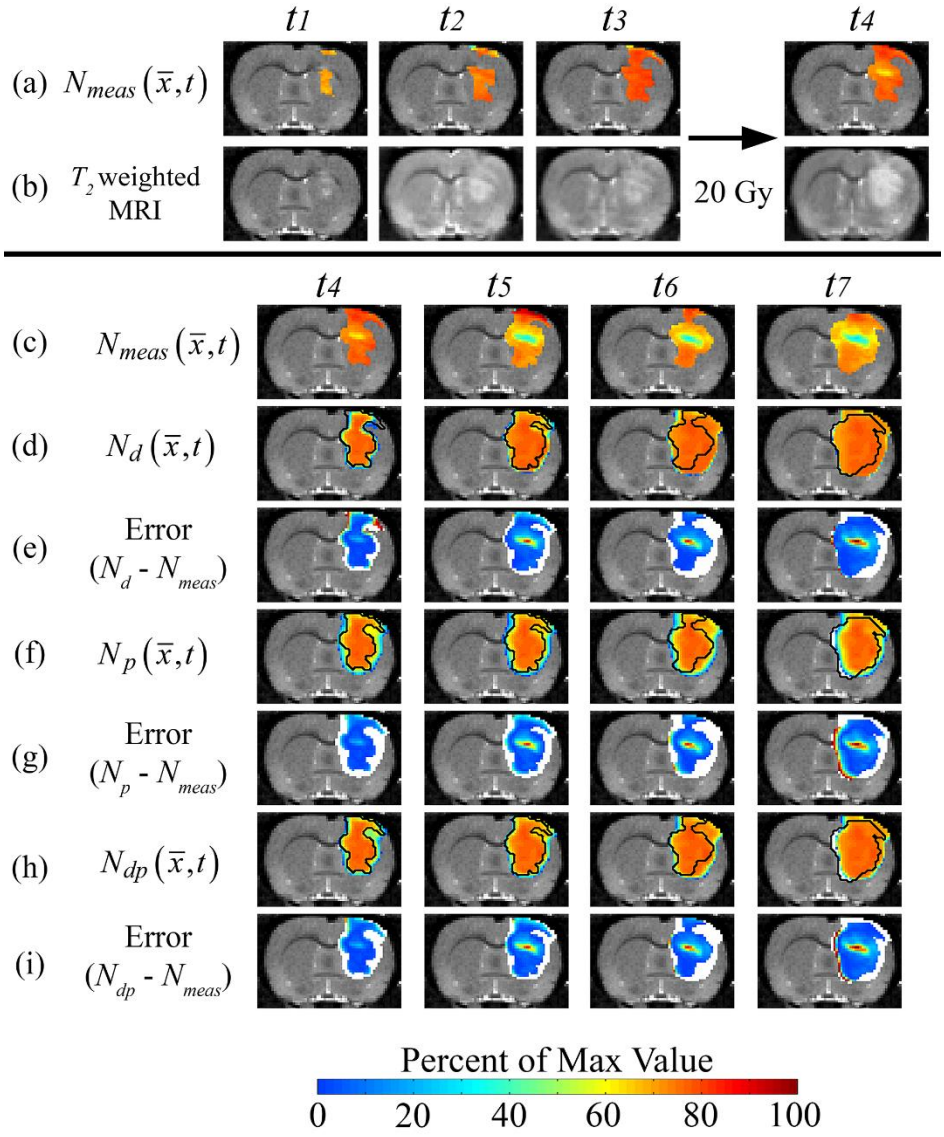

Figure 5.3. Comparison of M_d, M_p, and M_{dp} descriptions of tumor growth for a rat receiving 20 Gy. Row (a) shows $N_{meas}(\bar{x},t)$ before (t_1, t_2, and t_3) and after radiotherapy (t_4), while row (b) displays T_2-weighted MRI data for a representative rat from the 20 Gy group. Rows (a, c) show the data used for parameter estimation, $N_{meas}(\bar{x},t)$. Rows (d, f, h) show $N_{model}(\bar{x},t)$ at the post-treatment time points while rows (e, h, i) show the percent error between $N_{meas}(\bar{x},t)$ and $N_{model}(\bar{x},t)$.The black lines in rows (d, f, h) represent the boundaries of $N_{meas}(\bar{x},t)$ while the white space in rows (e, h, i) represent areas where $N_{meas}(\bar{x},t)$ was equal to zero. Increased overestimation of the tumor size was observed for the M_d and M_{dp} models at t_6 and t_7 compared to the M_p model. All three models had high error (rows (e, h, i)) in low cell density areas observed in $N_{meas}(\bar{x},t)$ (row (c)).

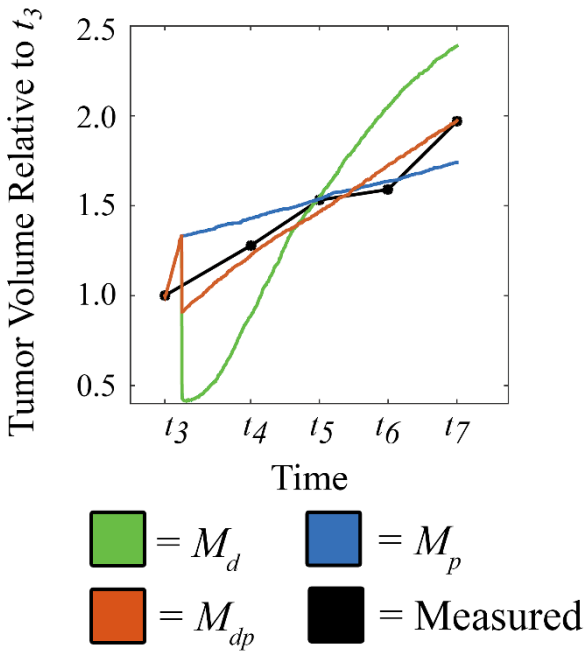

Figure 5.4. Example model fits for a rat receiving 20 Gy. Tumor volume relative to pre-treatment tumor volume (t_3) is shown from t_3 to t_7 for the M_d model (green line), the M_p model (blue line), the M_{dp} model (orange line), and measured values (black line). Both the M_d and M_{dp} models result in a shrinking of the tumor volume following radiotherapy. The M_p and M_{dp} models both had reduced growth rates, while the M_d mad had a rapid regrowth.

Figure 5.4 shows the measured (black lines) and model estimates (M_d-green line, M_p-blue line, M_{dp}-orange line) of tumor volume at days t_3 through t_7 for the same representative 20 Gy rat. The M_d and M_{dp} models both reduce the tumor volume following radiotherapy, underestimating tumor volume on days t_4 and t_5. As there is no death term in the M_p model it results in an overestimate of tumor volume on days t_4 and t_5. Higher model error (nRMS error) was observed for the M_d model (0.187) compared to the M_p and M_{dp} model (0.071 and 0.040, respectively).

Figure 5.5 compares the central imaging slice to histological sections (H&E, Ki-67) from the same representative 20 Gy rat. Low cell density regions in $N_{meas}(\bar{x}, t_7)$, panel (a), are also

present in the H&E slice (panel (b), inset A), while a second low density region (panel (b), inset B) is not visible in this imaging slice. A high level of positive stained *Ki-67* cells (73.95 ± 4.56 %) are observed throughout the tumor region.

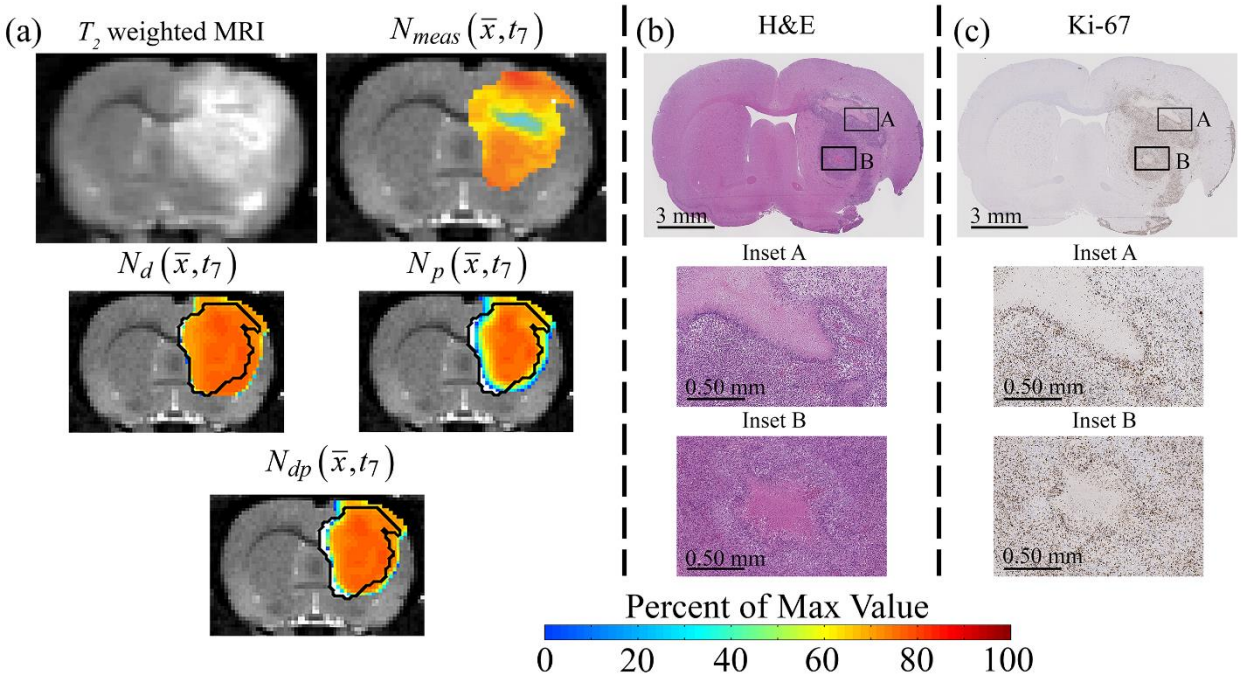

Figure 5.5. Measured and model estimates of cell number compared to histological sections for a rat receiving 20 Gy. Column (a) shows a T_2 weighted MR image, the tumor cell number map estimated from DW-MRI data, and the simulated tumor growth from the three models (M_d, M_p, and M_{dp}). Column (b) shows an H&E stained tissue section acquired near this imaging slice with insets A and B indicating areas of low cell density. Similarly, column (c) shows a Ki-67 stained tissue section. In panel (c), positive staining (brown) was seen through the tumor with the exception of the low cell density regions (insets A and B). The low cell density regions in $N_{meas}(\bar{x},t_7)$ are present in inset A from the H&E slide. Although, $N_{meas}(\bar{x},t_7)$ does not show the low cell density region in inset B.

Figure 5.6 shows $N_{meas}(\bar{x},t_1 \rightarrow t_7)$ and $N_{model}(\bar{x},t_4 \rightarrow t_7)$ at the central slice for a representative rat receiving a dose of 40 Gy. The M_d model results in an increased overestimation

of tumor size (greater than 92%, row (d)) compared to the M_p and M_{dp} models (less than 5%, rows (f, h)). On day t_4, the M_d and M_{dp} models underestimate the tumor size resulting in high voxel level

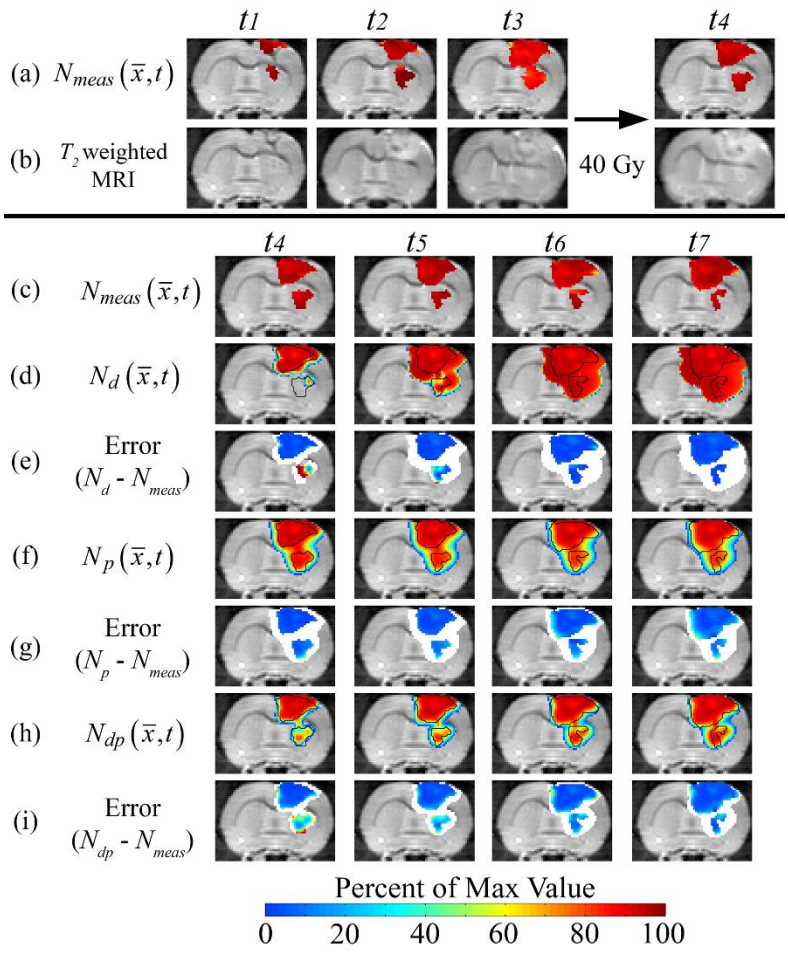

Figure 5.6. Comparison of M_d, M_p, and M_{dp} descriptions of tumor growth for a rat receiving 40 Gy. Row (a) shows $N_{meas}(\bar{x},t)$ before (t_1, t_2, and t_3) and after radiotherapy (t_4), while row (b) shows T_2-weighted images for a representative rat from the 40 Gy group. Rows (a, c) show the data used for parameter estimation, $N_{meas}(\bar{x},t)$. Rows (d, f, h) show $N_{model}(\bar{x},t)$ at the post-treatment time points while rows (e, h, i) show the percent error between $N_{meas}(\bar{x},t)$ and $N_{model}(\bar{x},t)$. The black lines in rows (d, f, h) represent the boundaries of $N_{meas}(\bar{x},t)$ while the white space in rows (e, h, i) represent areas where $N_{meas}(\bar{x},t)$ was equal to zero. The M_d model resulted in overestimation of tumor size on days t_5 through t_7 (row (d)). The M_p and M_{dp} models more closely matched the tumor shape and size at all time points (rows (f, h)).

error (40.42 ± 3.67% and 29.33 ± 2.57%, respectively). The average voxel-wise error for the M_d model, however, was less than 19% on days t_5 through t_7. The M_p model had statistically significant lower voxel-wise error on day t_4 (15.99 ± 2.60%) which increased at the later time points (greater than 20%). The M_{dp} model also had greater than 20% error at the voxel level on days t_5 through t_7.

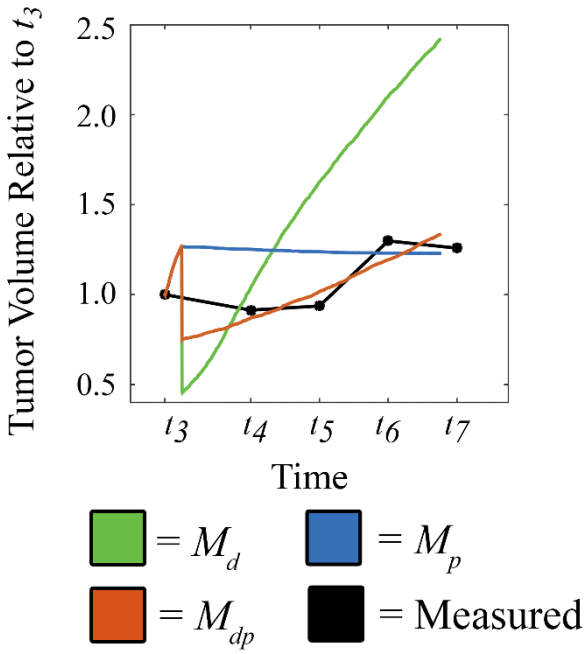

Figure 5.7. Example model fits for a rat receiving 40 Gy. Tumor volume relative to pre-treatment tumor volume (t_3) is shown from t_3 to t_7 for the M_d model (green line), the M_p model (blue line), the M_{dp} model (orange line), and measured values (black line). The M_{dp} model best fits the tumor volume time course, while the M_d model results in an overestimation of tumor size from t_5 through t_7. The M_p model predicts no tumor growth following radiotherapy.

Figure 5.7 shows the measured (black lines) and model estimates (M_d-green line, M_p-blue line, M_{dp}-orange line) of tumor volume at days t_3 through t_7 for the same representative 40 Gy rat. The M_d model had the higher total error (nRMS error = 0.626) compared to the M_{dp} and M_p models

error = 0.063 and 0.182, respectively). The optimal $k_{p,rt}$ for the M_p model was 0 resulting in essentially no tumor growth following radiotherapy. The M_d and M_{dp} models both capture the decrease in tumor volume following radiotherapy, while the M_{dp} model better captures the regrowth (t_5 through t_7, nRMS error = 0.063) compared to the M_d and M_{dp} models.

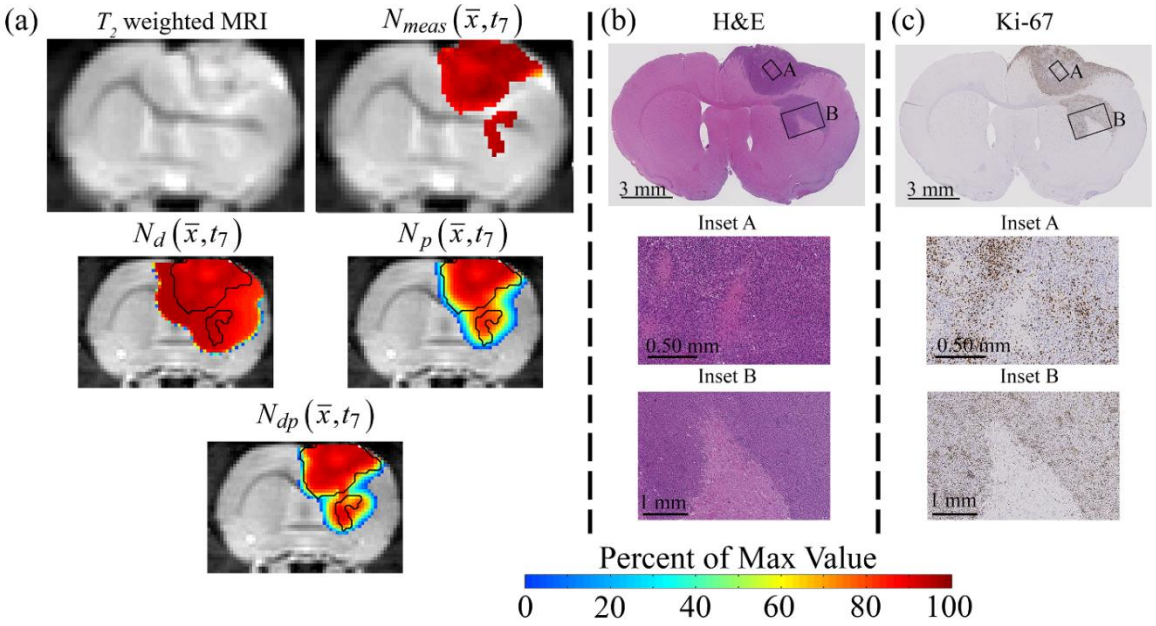

Figure 5.8. Measured and model estimates of cell number compared to histological sections for a rat receiving 40 Gy. Column (a) shows a T_2 weighted MR image, the tumor cell number map estimated from DW-MRI data, and the simulated tumor growth from the three models (M_d, M_p, and M_{dp}). Column (b) shows an H&E stained tissue section acquired near this imaging slice with insets A and B indicating areas of high cell density. Very few areas of low cell density (column b, inset A) were observed throughout the tumor. Similarly, column (c) shows a Ki-67 stained tissue section in which clusters of proliferating cells were observed throughout the tumor.

Figure 5.8 compares $N_{meas}(\bar{x},t_7)$ and $N_{model}(\bar{x},t_7)$ (panel (a)) to H&E (panel (b)) and Ki-67 (panel (c)) stained sections for the same representative 40 Gy rat. An average cell density

of 6336 ± 334 cells/mm^2 was observed across for in the Ki-67 stained sections. High cell density is observed in both inset A and B. Although there are a few low cell density regions (inset A) that appear throughout the tumor. Lower positive Ki-67 stained cells (64.53 ± 2.90%) were observed compared to the 20 Gy rat (Figure 5.5).

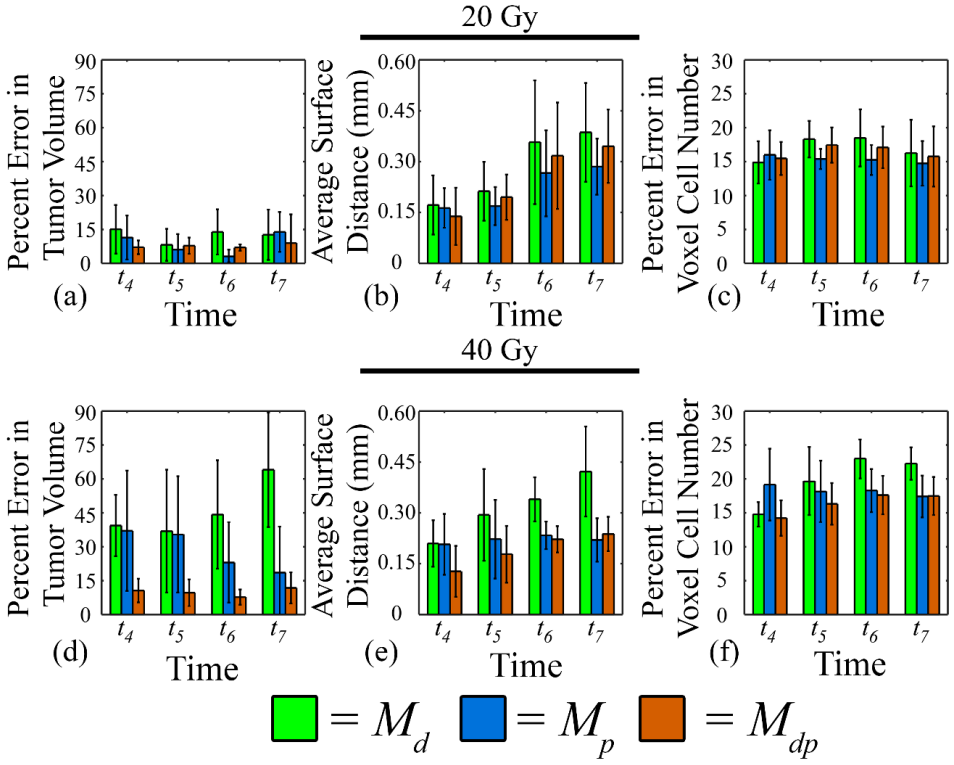

Figure 5.9. Global and local error results for model descriptions for the 20 and 40 Gy groups. Results for the 20 Gy (panels (a - c)) and 40 Gy (panels (d - f)) groups are shown at all post-radiotherapy time points. Global level error is assessed by the percent error in tumor volume (panels (a, d)) and the average surface distance (panels (b, e)), while local level error was assessed by calculating the percent error in voxel cell number (panels (c, f)). The mean and 95% confidence interval is reported in each plot. Generally, high global level errors were observed for the M_d model (green bars) for both treatment groups, while the M_{dp} (orange bars) model resulted in low global level errors. All three models resulted in low local level errors for the 20 Gy group (panel (c)), while the M_d and M_{dp} models had lower error for the 40 Gy group (panel (f)).

Figure 5.9 presents the percent error in tumor volume, the average surface distance, and the percent error in voxel cell number for both the 20 Gy rats (panels (a-c)) and the 40 Gy rats (panels (d-f)). (Table 5.1 reports the significant differences observed for the data presented in Figure 5.9.) For the 20 Gy group, the M_d (green bars) and M_p (blue bars) have less than 16% error in tumor volume (panel (a)) at all time points, while the M_{dp} model error was less than 9% error in tumor volume. The ASD increased over time from 0.14 mm to 0.38 mm (panel (b)). The M_p model had the lowest voxel-level error (panel (c), ranging from 14.74% to 15.99%) compared to the M_d and M_{dp} models (ranging from 14.88% to 18.50%). For the 40 Gy group, high error in tumor volume (panel (d)) was observed for the M_d model (greater than 36%) and the M_p model (greater than 18%) compared to the M_{dp} model less than 12% at all time points. Low ASD (panel (e)) was observed for the M_p and M_{dp} models (less than 0.24 m) compared to the M_d model (less than 0.43 mm). Similarly, higher voxel level error (panel (f)) was observed for the M_d model (14.77% to 22.25%) compared to the M_p model (17.40% to 19.15%) and M_{dp} model (14.22% to 17.62%).

Table 5.1 reports the statistically significant ($p < 0.05$) differences observed following pairwise comparisons. For the 20 Gy group, the M_d model had significantly increased error in tumor volume relative to the M_p model at day t_6, while no other significant differences were observed. For the 40 Gy group, the M_d model had statistically significant increased error in tumor volume and voxel cell number at t_7 compared to the M_p and M_{dp} models. The M_d model also had increased ASD compared to the M_p and M_{dp} models on days t_6 and t_7. No significant differences were observed between the M_p and M_{dp} models.

Table 5.1. Results of the pairwise comparison for model fitting error of the M_d, M_p, and M_{dp} models.

	Model Comparisons	Percent Error in Tumor Volume	Average Surface Distance	Percent Error in Voxel Cell Number
20 Gy	$M_d \neq M_p$	t_6	NS	NS
	$M_d \neq M_{dp}$	NS	NS	NS
	$M_p \neq M_{dp}$	NS	NS	NS
40 Gy	$M_d \neq M_p$	t_7	t_6, t_7	t_7
	$M_d \neq M_{dp}$	t_6, t_7	t_6, t_7	t_6, t_7
	$M_p \neq M_{dp}$	NS	NS	NS

Time points listed had significant differences between the means of the two models ($p < 0.05$). Non-significant differences were marked NS.

Table 5.2 reports the mean and 95% confidence interval for the nRMS error for all three models for both dose groups. The M_{dp} model resulted in the lowest nRMS error for both the 20 and 40 Gy groups, while the M_d model had the highest nRMS error. No significant differences were observed for the 20 Gy group. The M_{dp} model, however, was significantly lower than the M_d model for the 40 Gy group. The M_d model also resulted in significantly higher error for the 40 Gy group compared to the 20 Gy group.

Table 5.2. nRMS error for M_d, M_p, and M_{dp} model descriptions of tumor growth.

	Model	Mean ± 95% confidence interval
20 Gy	M_d	0.109 ± 0.057
	M_p	0.085 ± 0.047
	M_{dp}	0.074 ± 0.046
40 Gy	M_d	$0.467 \pm 0.181^{+}$
	M_p	0.272 ± 0.192
	M_{dp}	$0.101 \pm 0.051^{*}$

* = Significant differences ($p = 0.05$) between M_d and M_{dp}
+ = Significant differences ($p = 0.05$) between treatment groups.

5.5.3 Histology

Figures 5.10-5.12 and Tables 5.3-5.4 report the results of the histological validation for the 20 and 40 Gy rats. Figure 5.10 shows the M_p (panels (a – c)) and M_d (panels (d – f)) model parameters versus percent positive Ki-67 stained cells for the 20 Gy group, the 40 Gy group, and combined. For the 20 Gy group (panels (a, d)), low correlation ($r < 0.33$, $p > 0.67$) was observed for $k_{p,rt}$ and $k_{d,rt}$ to Ki-67 staining. For the 40 Gy group (panels (b, e)), high correlation ($r = -0.89$ and $r = 0.93$, $p < 0.11$) was observed for $k_{p,rt}$ and $k_{d,rt}$ to Ki-67 staining. When combined, the 20 Gy and 40 Gy rats (panel (c, f)) had low correlation ($r = 0.06$ and $r = -0.09$, $p > 0.84$) between model parameters and Ki-67 staining.

Figure 5.11 shows the M_{dp} parameters $k_{p,rt}$ and $k_{d,rt}$ versus percent positive stained Ki-67 cells for the 20 Gy (panels (a, d)), 40 Gy (panels (b, e)), and combined (panels (c, f)). For the 20 Gy group, low correlation ($r = 0.15$, $p = 0.85$) was observed between $k_{p,rt}$ and positive Ki-67 staining (panel (a)). The 40 Gy rats, however, had a higher level of correlation ($r = 0.73$, $p = 0.27$) between $k_{p,rt}$ and Ki-67 (panel (b)). When combined, the 20 and 40 Gy rats (panel (c)) had low overall correlation ($r = 0.24$, $p = 0.56$) between $k_{p,rt}$ and Ki-67. A high level of correlation was observed between $k_{d,rt}$ and Ki-67 was observed ($r = -0.95$ and $r = -0.96$, $p < 0.05$) for the 20 Gy and 40 Gy groups (panels (d-e)), although low correlation ($r = -0.48$, $p = 0.23$) was observed for the combined groups (panel (f)). The highest level of correlation ($r = -0.96$, $p = 0.037$) was observed between the 40 Gy estimates of $k_{d,rt}$ and Ki-67 (panel (e)). Figure 5.12 shows measured

ADC for both the 20 and 40 Gy rats versus the measured cells per mm^2. A modest inverse relationship was observed between ADC and cell density (r = -0.52, p = 0.19).

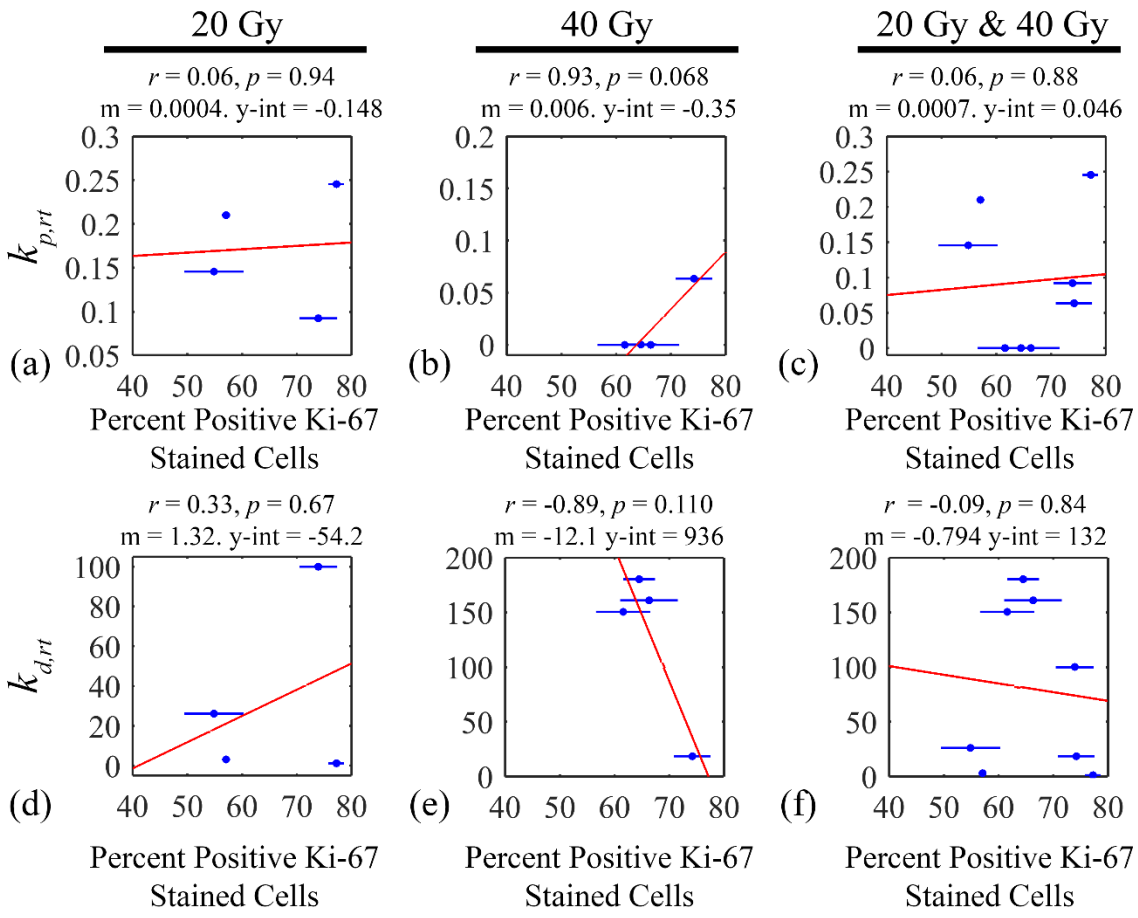

Figure 5.10. M_p and M_d model parameters comparison to Ki-67 staining. $k_{p,rt}$ (panels (a - c)) and $k_{d,rt}$ (panels (d - f)) were compared to the percent positive Ki-67 stained cells. The blue data points represent the mean and 95% confidence interval for Ki-67 measurements over several tissue slides, while the red line represents the linear fit to the data points. The results of linear regression, correlation, and p value are reported above each plot. Low correlation (r < 0.06, p > 0.88) was observed between $k_{p,rt}$ and Ki-67 for the 20 Gy (panel (a)) and combined group (panel (c)). Similarly, low correlation (r < 0.33, p > 0.67) was observed between $k_{d,rt}$ and Ki-67 for the 20 Gy (panel (d)) and combined group (panel (f)). High correlation (r > 0.89, p < 0.110), however, was observed for both $k_{p,rt}$ (panel (b)) and $k_{d,rt}$ (panel (e)) to Ki-67 for the 40 Gy group.

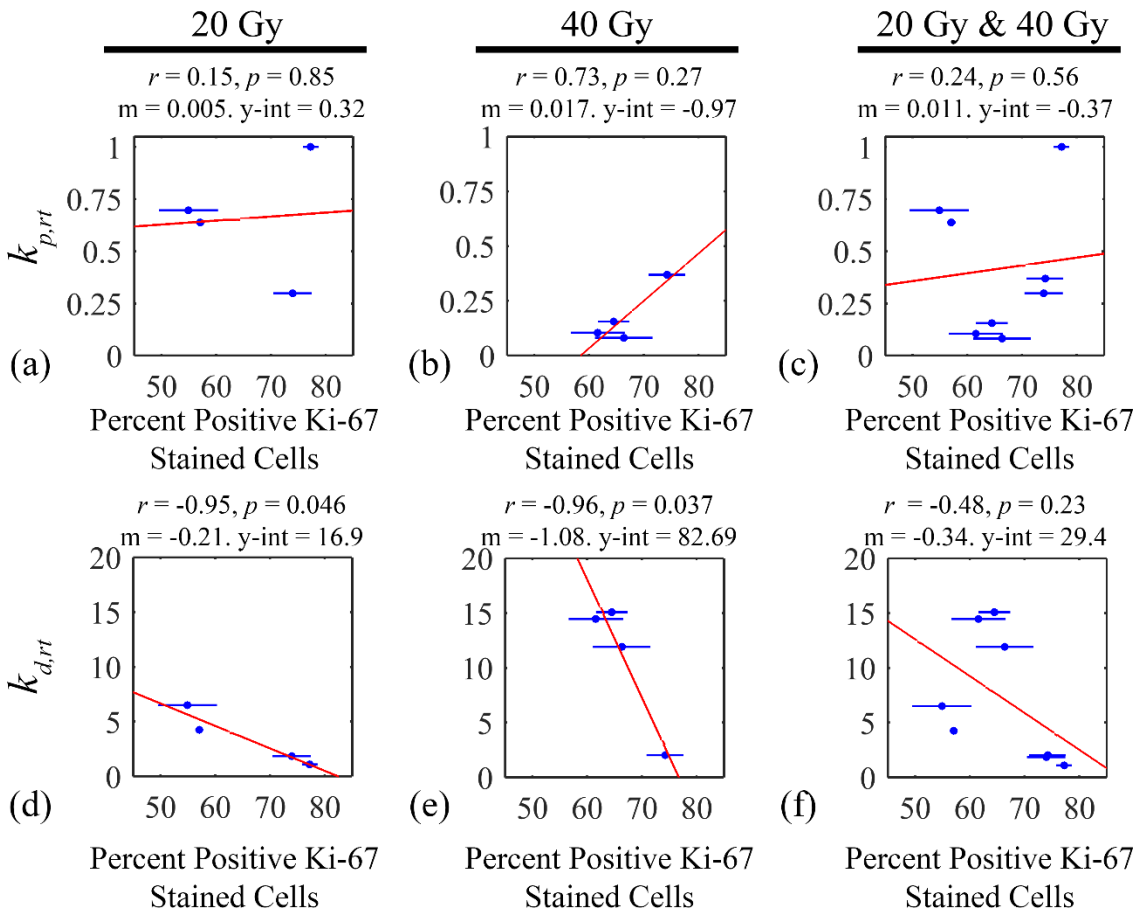

Figure 5.11. M_{dp} model parameters comparison to Ki-67 staining. $k_{p,rt}$ (panels (a - c)) and $k_{d,rt}$ (panels (d - f)) were compared to the percent positive Ki-67 stained cells. The blue data points represent the mean and 95% confidence interval for Ki-67 measurements over several tissue slides, while the red line represents the linear fit to the data points. The results of linear regression, correlation, and p value are reported above each plot. Low correlation was ($r < 0.24$) observed between $k_{p,rt}$ and Ki-67 for the 20 Gy (panel (a)) and combined group (panel (b)). Statistically significant correlation ($r = -0.95$ and $r = -0.96$, $p < 0.05$) was observed for both the 20 and 40 Gy estimates of $k_{d,rt}$ and Ki-67 staining (panels (d - e)). Poor correlation ($r = -0.48$) was observed for the combined group (panel (f)).

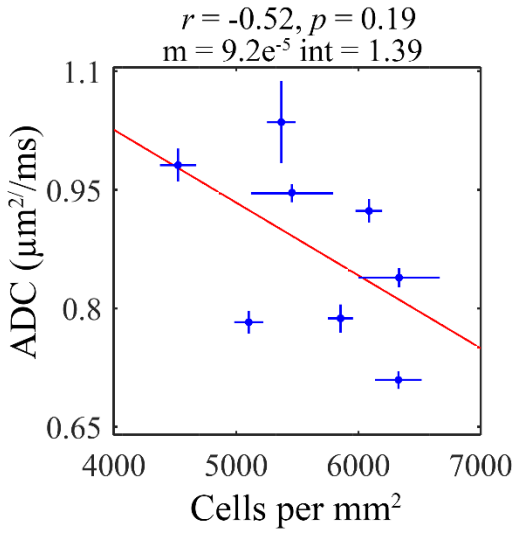

Figure 5.12. Comparison of ADC and cells per tissue area. The above plot shows the mean and 95% confidence interval (blue points) for the measured ADC (vertical axis) and cells per mm^2 (horizontal axis) for both the 20 Gy and 40 Gy animals. The red line represents the linear fit to the data points. The results of linear regression, the correlation coefficient, and *p* value are shown above the plot. ADC generally has an inverse relationship to cell density (r = -0.52) although it is not statistically significant (p = 0.19).

Table 5.3 reports summary histology statistics (cells/mm^2, percent positive Ki-67 stained cells) and ADC for the 20 Gy and 40 Gy rats. Statistically significant ($p < 0.05$) lower cell density was observed for the 20 Gy rats compared to the 40 Gy rats. The 20 Gy rats also had an increased ADC compared to the 40 Gy rats. Fewer proliferating cells were observed on average in the 40 Gy group versus the 20 Gy group. Table 5.4 reports the summary statistics for the estimated model parameters for the 20 Gy and 40 Gy rats. The 20 Gy rats had statistically significant decreased $k_{d,rt}$ compared to the 40 Gy rats for the M_d model. No significant differences were observed between the 20 Gy and 40 Gy rats for $k_{d,rt}$ estimated for the M_{dp} model. The 20 Gy rats also had statistically significant increased $k_{p,rt}$ for both the M_p and M_{dp} models compared to the 40 Gy rats. $k_{p,rt}$ estimated

for the M_p model had a strong inverse relationship to measured doubling time for the 20 Gy group (r = -0.80, p = 0.03) but not the 40 Gy group (r = -0.64, p = 0.12). $k_{p,rt}$ estimated for the M_{dp} model also had a strong inverse relationship to measured doubling time for the 20 Gy (r = -0.82, p = 0.09) and 40 Gy (r = -0.87, p = 0.02) groups.

Table 5.3. Summary statistics for histology and ADC.

	Cells/mm^2	*Apparent* Diffusion Coefficient (μm^2/ms)	Percent Positive Ki-67 Stained Cells
20 Gy	5066 ± 184.8*	0.955 ± 0.017*	68.9 ± 2.92*
40 Gy	5388 ± 111.4*	0.821 ± 0.008 *	59.01 ± 5.03*

Mean ± 95% confidence interval
* = Significant differences (p = 0.05) between dose groups.

Table 5.4. Summary statistics for estimated model parameters.

	M_d $k_{d,rt}$	M_p $k_{p,rt}$	M_{dp} $k_{d,rt}$	M_{dp} $k_{p,rt}$
20 Gy	29.61 ± 45.17*	0.168 ± 0.067*	4.173 ± 4.192	0.685 ± 0.285*
40 Gy	113.1 ± 64.49*	0.045 ± 0.052 *	8.248 ± 5.786	0.283 ± 0.102*

Mean ± 95% confidence interval
* = Significant differences (p = 0.05) between dose groups.

5.5.4 Prediction Error

Figures 5.13-5.14 and Tables 5.5-5.6 report the analysis of the prediction error of the M_d, M_p, and M_{dp} models for the 20 and 40 Gy rats. Figure 5.13 shows example model fits for a representative 20 Gy rat (panels (a - c)) and a 40 Gy rat (panels (d - f)). For the 20 Gy rat, when only day t_4 is used to estimate the post-radiotherapy parameters, the predicted M_d and M_{dp} tumor volumes overlap (panel (a)), while M_p predicts no future tumor growth. As more time points are included, M_p begins to predict an increase in tumor volume (panels (b - c)), while the predicted M_{dp} volume approaches the measured tumor volume. When t_4 through t_6 was used the nRMS error was lower for the M_{dp} model (0.024) compared to the M_d and M_p models (0.216 and 0.194, respectively). For the 40 Gy rat, due to the decrease in tumor volume on t_4 and t_5 the M_p model predicts the same tumor volume for all three approaches (panels (d - f)). For this dose, the M_p model has the lowest nRMS (less than 0.142) error for all parameter estimation approaches. The M_d model poorly predicts future tumor growth regardless of the number of time points used (nRMS error greater than 0.720). As more points are included in the parameter optimization, the M_{dp} model becomes less similar to the M_d model and becomes a combination of the M_p and M_d model resulting in a low nRMS error when all three time points are used (0.104).

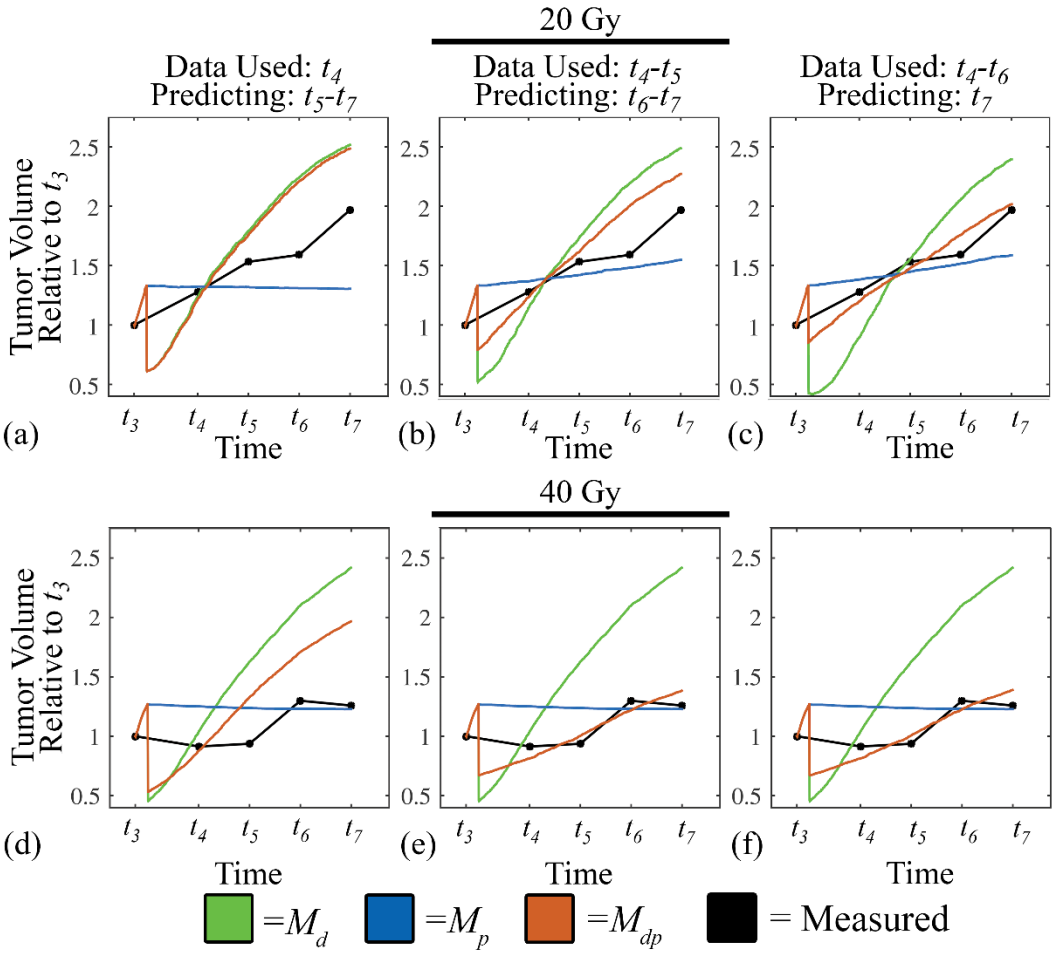

Figure 5.13. Example model fits for tumor growth predictions. Tumor volume relative to pre-treatment tumor volume (t_3) is shown from t_3 to t_7 for the M_d model (green line), the M_p model (blue line),the M_{dp} model (orange line), and measured values (black line) for a representative 20 Gy (panels (a - c)) and 40 Gy rat (panels (d - f)). Model predictions are shown using one (panels (a, d)), two (panels (b, e)), and three (panels (c, f)) post-treatment time points to estimate model parameters. More time points are needed for the M_{dp} model to accurately capture post-radiotherapy tumor growth kinetics. Similarly, more than one-time point is needed for the M_p model to accurately predict volume growth for the 20 Gy rat (panels (b - c)), while for the 40 Gy rat the M_p model predicts no tumor growth regardless of the number of data points used.

Figure 5.14 shows the percent error in tumor volume, average surface distance, and percent error in voxel cell number for predictions made using one, two, and three post-radiotherapy time

points to estimate model parameters. (Table 5.5 summarizes the significant differences observed for the data presented in Figure 5.14.) Error between the predicted and measured tumor growth was assessed at time points not used to estimate model parameters or $t_{np,d}$, where n is the number of time points used to estimate parameters and d is the predicted time point. For the 20 Gy rats, no significant difference in error in tumor volume (panel (a)) were observed between models for all time points. Error in tumor volume ranged from 10.50% to 33.48% when one post-radiotherapy time point was used, 7.74% to 21.24% when two post-radiotherapy time points were used, and 12.23% to 18.87% when three post-radiotherapy time points were used. Similarly, no significant differences in ASD (panel (b)) were observed between models, with ASD ranging from 0.11 mm to 0.40 mm for all prediction time points. The M_p model did, however, have a statistically significantly lower error in voxel cell number (14.07 ± 2.43%, panel (c)) compared to the M_d model on $t_{1p,5}$ (18.79 ± 3.29%,). Error in voxel cell number ranged from 13.86% to 18.79% for all predictions. For the 40 Gy rats, several significant differences in error in tumor volume (panel (d)) were observed between models at the prediction time points. Specifically, the M_p and M_{dp} had statistically significant lower error in tumor volume (ranging from 20.20% to 68.63%) compared to the M_d model (45.52% to 76.77%). Similarly, the M_p and M_{dp} model also had statistically significant lower ASD (ranging from 0.22 mm to 0.41 mm), panel (e)) compared to the M_d model (0.31 mm to 0.46 mm). The M_p also had significant lower error at the voxel-level (ranging from 17.23% to 18.42%, panel (f)) compared to the M_d model (ranging from 21.76% to 24.08%).

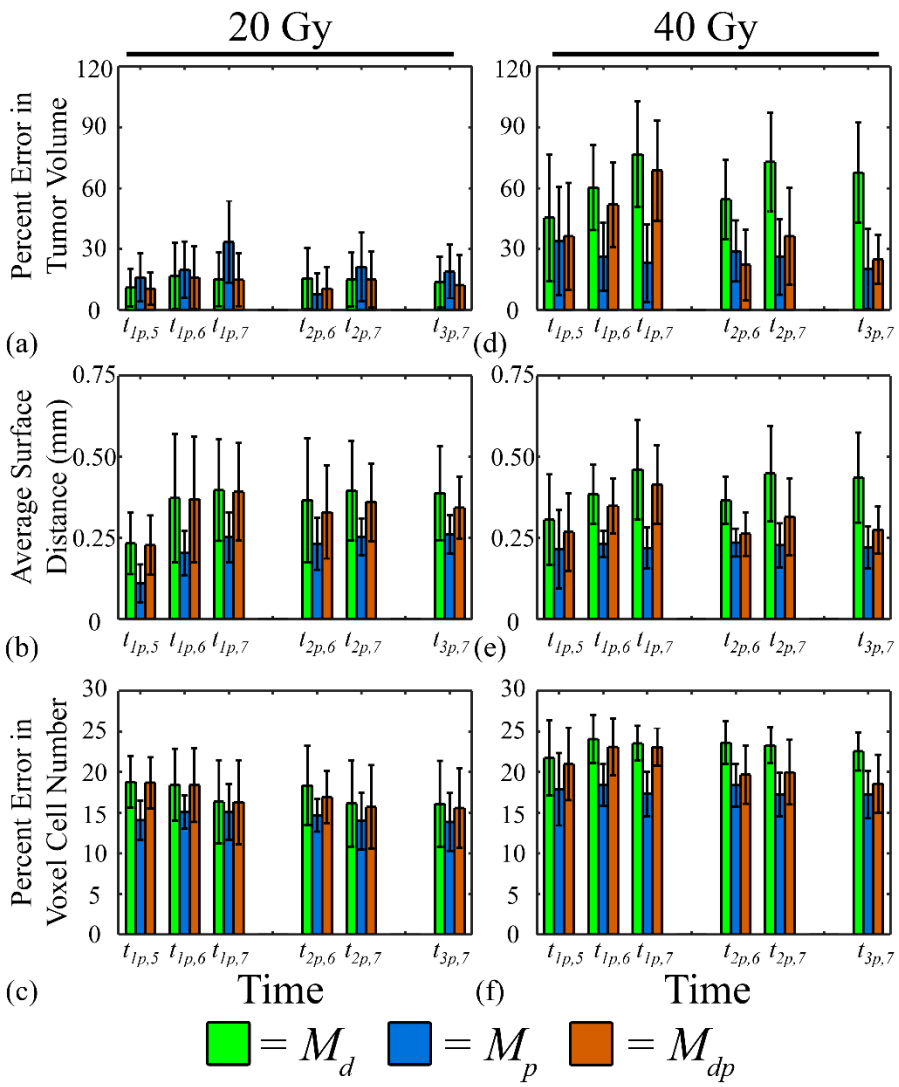

Figure 5.14. Global and local error results for model predictions for the 20 and 40 Gy groups. Results for the 20 Gy (panels (a - c)) and 40 Gy (panels (d - f)) groups are shown at all prediction time points. Global level error is assessed by the percent error in tumor volume (panels (a, d)) and the average surface distance (panels (b, e)), while local level error was assessed by calculating the percent error in voxel cell number (panels (c, f)). The mean and 95% confidence interval is reported in each plot. Error between the predicted and measured tumor growth was assessed at time points not used in the parameter estimation $t_{np,d}$, where n is equal to the number of time points used to estimate parameters and d is the predicted time point. Generally, low global and local level errors was observed for the M_{dp} models for both the 20 and 40 Gy case (orange bars). The M_d model had increased error in tumor volume for 40 Gy rats (green bars, panel(d)) compared to the 20 Gy rats (panel (a)). The M_p and M_{dp} models (blue and orange bars, respectively) both had statistically significant lower global and local errors for the 40 Gy group.

Table 5.5 summarizes the significant differences observed through pair-wise comparisons for prediction volumes. No significant difference was observed for volume error or ASD for the 20 Gy group. The M_p model, however, had a significantly lower voxel level error at $t_{1p,2}$. For the 40 Gy group, the M_p and M_{dp} models had significantly lower error in tumor volume and ASD at several time points. The M_p model also had significantly lower voxel level error than models M_d and M_{dp} at all time points except $t_{1p,1}$. No significant differences were observed between the M_p and M_{dp} models.

Table 5.5. Results of the pairwise comparison for prediction error of the M_d, M_p, and M_{dp} models.

	Model Comparisons	Percent Error in Tumor Volume	Average Surface Distance	Percent Error in Voxel Cell Number
20 Gy	$M_d \neq M_p$	NS	NS	$t_{1p,6}$
	$M_d \neq M_{dp}$	NS	NS	NS
	$M_p \neq M_{dp}$	NS	NS	NS
40 Gy	$M_d \neq M_p$	$t_{1p,6}$, $t_{1p,7}$, $t_{2p,7}$, $t_{3p,7}$	$t_{1p,6}$, $t_{1p,7}$, $t_{2p,6}$, $t_{2p,7}$, $t_{3p,7}$	$t_{1p,6}$, $t_{1p,7}$, $t_{2p,6}$, $t_{2p,7}$, $t_{3p,7}$
	$M_d \neq M_{dp}$	$t_{2p,6}$, $t_{2p,7}$, $t_{3p,7}$	$t_{2p,6}$, $t_{3p,7}$	NS
	$M_p \neq M_{dp}$	NS	NS	NS

Time points listed had significant differences between the means of the two models ($p < 0.05$). Non-significant differences were marked NS.

Table 5.6 reports the nRMS error for the prediction time courses evaluated from t_n to t_7. For the 20 Gy group, no significant differences were observed between models regardless of the number of data points used in parameter estimation. The 40 Gy group, however, saw significantly decreased nRMS error for the M_p model compared to the M_d model when one, two, and three time

points were used to estimate model parameters. The M_{dp} also showed reduced nRMS error compared to the M_d model when two and three time points were used for parameter estimation. The M_d model also had significantly increased error for the 40 Gy compared to the 20 Gy group.

Table 5.6. nRMS error for prediction time courses.

	Model	Data used: t_4	Data used: t_4, t_5	Data used: t_4, t_5, t_6
20 Gy	M_d	0.140 ± 0.085	0.153 ± 0.099	0.137 ± 0.126
	M_p	0.227 ± 0.135	0.157 ± 0.127	0.189 ± 0.134
	M_{dp}	0.136 ± 0.079	0.142 ± 0.074	0.122 ± 0.148
40 Gy	M_d	0.616 ± 0.212^{+}	0.644 ± 0.211^{+}	0.677 ± 0.246^{+}
	M_p	0.276 ± 0.181*	0.279 ± 0.163*	0.202 ± 0.197*
	M_{dp}	0.537 ± 0.200^{+}	0.302 ± 0.196*	0.248 ± 0.120*

Mean ± 95% confidence interval
* = Significant differences (p = 0.05) between model listed and M_d model.
+ = Significant differences (p = 0.05) between treatment groups.

5.6 Discussion

The analysis of the model fit error of the M_d, M_p, and M_{dp} models indicated that at 20 Gy all three models described tumor growth post-radiotherapy equally well, with the M_{dp} model having the lowest nRMS error. At 40 Gy the M_{dp} model had statistically significant lower model fit error (low percent error in tumor volume and low percent error in voxel cell number) compared to the M_d model, while no significant differences were observed between M_p and M_{dp}.. The cell death parameter ($k_{d,rt}$) estimated for the M_{dp} model also had a strong and statistically significant

inverse correlation to the percent positive Ki-67 stained cells for both the 20 and 40 Gy groups, while $k_{p,rt}$ had a weaker relationship with Ki-67 staining. The analysis of the prediction error of the M_d, M_p, and M_{dp} models demonstrated that all three models can accurately predict future tumor growth for the 20 Gy case with the M_{dp} model having the lowest overall error. When applied to the 40 Gy rats, however, the M_d, M_p, and M_{dp} models poorly predicted future tumor growth although the M_p and M_{dp} models had significantly lower error compared to the M_d model. The analysis of the model fit and prediction error of the M_d, M_p, and M_{dp} models suggest that the M_{dp} may provide the best characterization of *in vivo* C6 glioma growth regardless of dose received.

The cell death or M_d model of post-radiotherapy growth is a variation of the classic LQ model. Previous implementations of the LQ model [120,179–181] typically characterize radiotherapy response following standard-of-care dose-fractionation plans at smaller dose per fraction (less than 2 Gy). In this work, instead of assigning the death rate as the fraction of cells that die due to radiotherapy [120] we fit for an uniform death rate. The $k_{d,rt}$ scaled by the logistic term results in spatially varying cell death with preferential killing at the periphery of the tumor compared to the interior. This term is biologically relevant as cells in the interior of the tumor may inhabit a hypoxic environment or have reduced or no proliferation due to cell crowding and lack of resources [182,183]. The varied response between the 20 and 40 Gy group suggests that the M_d model may be more valid at low doses where post-radiotherapy growth kinetics (e.g., doubling time, $k_{p,rt}$) more closely match the untreated growth kinetics (Figure 5.2). Similarly, validity of applying the LQ model to at high doses is debated [184,185].

The M_p model, in general, provided better model descriptions and predictions compared to the M_d model. Based on the reduced doubling time observed following radiotherapy (Figure 5.2), it was hypothesized that this model may be able to better describe the post-radiotherapy growth kinetics. However, examination of the model fits (Figures 5.4, 5.7, and 5.13) show in cases where the tumor volume is lower than the volume at t_{rt} the optimal $k_{p,rt}$ causes no change in tumor volume resulting in high error when the current volume is less than volume at t_{rt} and low errors when the current volume is approximately equal to the volume at t_{rt}. While low error was observed in tumor volume predictions, this model is inappropriately applied when the data used for fitting indicates a decrease in tumor volume relative to the post-radiotherapy time points. This model may potentially provide good short term predictions when tumor volume post-radiotherapy is greater than the tumor volume at t_{rt}; however, it is not recommended if tumor volume decreases.

Based off of the M_d and M_p analysis it was evident that combination of these two effects may potentially characterize post-radiotherapy tumor growth. The death component captures the immediate effects (cell death/shrinking of tumor) while the proliferation components contributes to the longer term alteration of tumor growth kinetics [177,186]. While more time points are needed to capture the death and regrowth kinetics, this model can provide accurate descriptions of *in vivo* glioma growth. The low model fit error (low error in tumor volume, ASD, and voxel cell number) and low prediction error of the M_{dp} model for both 20 Gy and 40 Gy rats suggest that it may be the most appropriate model to select for modeling response at either dose. Furthermore, model parameters ($k_{p,rt}$ and $k_{d,rt}$) appeared to be dose specific suggesting that a more explicit

relationship between dose and $k_{p,rt}$ and $k_{d,rt}$ may exist. Comparison of model parameters to histological staining indicated a strong inverse relationship between $k_{d,rt}$ and the percent positive stained Ki-67 cells and a weak relationship between $k_{p,rt}$ and Ki-67 staining. The strong histological correlation to $k_{d,rt}$ suggests that it may provide some insight into the underlying tumor biology post-radiotherapy.

There are several limitations to this current approach. One limitation is that the imaging measurements from CE-MRI may potentially indicate false volume increases or decreases following radiotherapy [62,187]. Pseudoprogression is often a result of increased inflammation, edema, and vessel permeability and can be challenging to distinguish from actual progression and is an active area of research [188–191]. A second limitation of this study is that the first post-radiotherapy imaging time point is 48 hours after treatment. An additional imaging time point within 48 hours of radiotherapy could potentially eliminate some of the ambiguity in the spatio-temporal evolution of the tumor immediately following treatment. A third limitation is that there is a lack of histology for untreated rats to which the treated groups can be compared, as well as a lack of histology at the time of treatment. However, the dose dependent decreases in Ki-67 have been observed by others [186]. In addition to obtained Ki-67 stained sections, an additional tissue section should be stained with pH2AX to assess DNA damage following radiotherapy to compare dose efficacy and dose dependent DNA damage [192]. A fourth limitation is the use of single fraction whole brain radiotherapy. Radiotherapy is more commonly delivered in small doses over several fractions using a more focal dose (conformal, intensity modulated radiotherapy,

stereotactic radiosurgery) to minimize normal tissue damage. Fractionated plans would also increase survival rate [193] potentially allowing for longer imaging and modeling studies to investigate radiotherapy response. Another limitation is the use of ADC to estimate tumor cellularity. There is modest correlation between ADC and cellularity as seen in Figure 5.12, however, the significance of this correlation is effected by the low number of animals used in the calculation. Furthermore, future studies with higher SNR or spatial resolution could be used to further align the *in vivo* and *ex vivo* data potentially reducing some of the error in these comparisons. However, we acknowledge that this relation is only a first order approximation and additional approaches to estimate cellularity should be investigated.

The models developed and analyzed within this study are an encouraging step towards the development of individualized radiotherapy plans. Further refinement of this model to include an explicit relationship between model parameters ($k_{p,rt}$ and $k_{d,rt}$) and dose would make the model more relevant to clinical care. Future work should utilize fractionated radiotherapy plans to more realistically match the standard of care for glioblastoma patients.

5.7 Conclusion

At low doses post-radiotherapy growth can be accurately described using a cell death model, a reduced proliferation model, or a combination of the cell death and reduced proliferation model. Furthermore, the cell death model and the combined model can accurately predict future tumor growth with low global and local level errors. At higher doses, the combined model most

accurately describes post-radiotherapy growth with low error in tumor volume, average surface distance, and voxel cell number, while the other models poorly describe tumor response at high doses. All models, however, had high prediction error at large doses. Overall, the combined model provides a more complete characterization of the post-radiotherapy growth kinetics, although further model development is needed to accurately predict tumor growth following large dose radiotherapy.

5.8 Acknowledgements

The authors thank Dr. Zou Yue for performing the animal surgeries and Dr. Daniel C. Colvin for assistance with the image registration. The authors also thank Drs. Michael L. Freeman and Sekhar R. Konjeti for assistance and usage of the x-ray machine.

CHAPTER 6

SYNOPSIS AND FUTURE DIRECTIONS

6.1 Summary

Prognosis for glioblastoma multiforme patients is quite poor. Patient response to chemotherapy or radiotherapy is often varied due to heterogeneity between patients and within individual tumors [3,4], with patients typically suffering recurrence 7 to 10 months from the conclusion of adjuvant therapy [2]. Furthermore, treatment options for patients with recurring tumor are usually selected on an individual basis as no current options have shown improved survival for all patients. Mathematical modeling that incorporate patient-specific information could, however, address these challenges by assisting in the selection of treatment options for individual patients, predicting response or progression earlier in the course of a treatment, or designing radiotherapy (or chemotherapy) regimens options optimized for the individual. Currently, however, there is a paucity of mathematical models that 1) have been validated to a patient or subjects own measurements, and 2) can be individualized using non-invasive measurements [16]. Towards this end, the goal of this dissertation was to develop biophysical models of *in vivo* glioma growth which can be individualized on a subject-to-subject basis using non-invasive imaging methods so that the accuracy and precision of tumor growth predictions can be compared directly to imaging and histology measurements.

In Aim 1, the model parameter estimation and forward evaluation methodology was developed and applied to the standard reaction diffusion model in a set of *in silico* and *in vivo* experiments. First, an *in silico* tumor set was used to develop an approach to accurately estimate model parameters from a subset of the total data and then use those model parameters to accurately predict the remaining subset of data. This approach was then applied to an *in vivo* model of glioma to assess the validity of using the standard reaction diffusion model to predict future tumor growth. Importantly, this work detailed the means to accurately estimate model parameters and demonstrated that the reaction diffusion model poorly characterizes *in vivo* glioma growth as observed through *in vivo* imaging data. This was the first investigation to test the accuracy and precision of the reaction diffusion equation's ability to predict the spatio-temporal evolution of an individual subject's tumor.

In Aim 2, the shortcomings of the reaction diffusion guided the development of three novel models aimed at improving the *in vivo* characterization of gliomas growth at both the global and local levels. First, a model incorporating a voxel-specific carrying capacity (CC) was developed and implemented to improve predictions of cell number at the local level. The second model developed and implemented incorporated a mechanically coupled (MC) tumor diffusion component to improve the description of tumor size and shape at the global level. Finally, the third model developed and implemented was a combination of the first two (MC-CC). The three models were then assessed using tumor measurements obtained from magnetic resonance imaging of rats with C6 gliomas. This work analyzed the ability of the three models to accurately describe

(i.e., how well does the model fit the data) and predict (i.e., how well does it describe future growth) *in vivo* glioma growth in rats. This work highlighted that the incorporation of a voxel-specific carrying capacity can significantly reduce local level errors compared to the standard reaction diffusion method and that a mechanically coupled diffusion coefficient can significantly improve predictions of future tumor volume. Importantly, it was shown that the combined MC-CC model can accurately predict future tumor volume and voxel cell number up to 6 days from the last day used for parameter estimation. The combined MC-CC model was a novel contribution to the tumor modeling literature that can be parameterized readily from imaging data.

In Aim 3, the effects of radiotherapy were incorporated into a novel expansion of the MC-CC model and applied to an *in vivo* dataset of rats receiving whole brain radiotherapy. In this study, three new models were developed and investigated that included the death of cells following radiotherapy, a reduced proliferation rate following radiotherapy, and a combination of both cell death and reduced proliferation. This work analyzed the ability of the three models to accurately describe and predict *in vivo* glioma growth in rats receiving either 20 Gy or 40 Gy. Importantly it was shown that at low doses all models provided equally accurate descriptions of *in vivo* glioma growth and could predict future tumor growth with low error. Of the models analyzed, however, the combined cell death and reduced proliferation model had the lowest error at 20 Gy. Furthermore, for the 40 Gy group it was also demonstrated that the combined model resulted in the lowest description and prediction error. This was a novel study that utilized imaging data to determine subject-specific response parameters and then used those data to forecast future tumor

status which could then be directly compared to future cell distributions and proliferation data estimated from *in vivo* imaging and histology.

Together, these studies show the feasibility of using medical imaging data to individually parameterize biophysical models of glioma growth to provide accurate and precise predictions of future tumor growth. Furthermore, these studies address a current gap in subject-specific modeling by developing the means to accurately determine model parameters from imaging data, detailing an approach to predict future tumor growth, and assessing the validity of several models of glioma growth to experimental measurements. Additionally, these studies begin to indicate the clinical viability of subject-specific models through the development and validation of a subject-specific model of radiotherapy response.

6.2 Limitations

The image driven biophysical models developed in this work have successful demonstrated the predictive and descriptive capabilities modeling can attain. There are, however, several limitations to the current implementation. One concern is regarding the identification of tumor regions and the estimation of tumor cellularity. First, imaging measurements from contrast-enhanced magnetic resonance imaging (CE-MRI) may be susceptible to falsely indicating volume increases or decreases following radiotherapy [62,187]. This is also a significant challenge in the clinical care of glioblastoma patients [194] where it is unclear if increased tumor volume observed in CE-MRI is active tumor growth or local tissue reaction (e.g., increased inflammation, edema,

or vessel permeability [62]) to treatment. Several groups are investigating ways to distinguish true and false tumor growth using imaging measurements such as DW-MRI [195], diffusion tensor imaging MRI [189], dynamic susceptibility enhanced MRI [196,197] , and MR spectroscopy [198] amongst others. The design of future experiments should include the acquisition of fixed tissue from a cohort of animals at each imaging time point to evaluate model error directly to histology measurements at those time points.

A second limitation is that there is ambiguity in changes in ADC measurements and the biological origin of that change. In this study, ADC determined from a standard pulsed gradient spin echo experiment is used to estimate cellularity. This is based off of assumptions that as cellularity increases there will be increased barriers for water diffusion resulting in a decrease in ADC. Several groups have observed strong correlations between ADC and histology estimates of cellularity and extracellular volume [65,67–69], although cellularity is not the sole factor contribution to a tissue's ADC. While an increase in cellularity would result in a decrease in ADC, there are also other biological factors (e.g., increase in cell size, increase in tissue tortuosity, decrease in cell permeability) that may have influenced the change in ADC. Future implementations of this modeling framework may need to incorporate additional imaging measurements [75,134,199] to reduce the ambiguity in the contributions to changes in ADC.

A third limitation is that for Aims 1 and 2 there were no histology data available for comparisons to model predictions. A challenge in the studies performed in these Aims is that not all rats survived to the conclusion of the study. Several rats died unexpectedly prior to the

conclusion of the study making histology impossible or unreliable at those time points. This limitation, however, was addressed in Aim 3 where histology was available for comparison to model predictions.

A fourth limitation of the models evaluated within these studies is the poor characterization of low cell density or necrotic tumor regions. While models including a voxel-specific carrying capacity reduce prediction error in these regions, they are only good if those regions exist in the data used for parameter estimation. Furthermore, necrosis and factors associated with necrosis (i.e., hypoxia) can influence both the overall growth of the tumor [143,200,201] and clinical outcome [182,202]. Models that incorporate a more biologically realistic description of cell proliferation, cell death, or the spatial variability in viability within a tumor [183,203] may be able to predict the development of these necrotic regions. Identification of these regions may help in the design or selection of patient therapies or help predict patient prognosis. A barrier to the implementation of models that characterize the temporal and spatial variation of cell proliferation and death on a subject-specific basis is that many of the parameters can only be measured through invasive means. However, novel model implementations of cell proliferation and death that utilize medical imaging measurements have the potential to provide individualized tumor models.

A final limitation is in the design of the radiotherapy study, which used a single dose whole brain radiotherapy versus a fractionated focal treatment schedule. Patients with glioblastoma typically receive a radiotherapy dose of 60 Gy divided into 30 fractions [2]. While 30 fractions of radiotherapy may be logistically impractical in a murine study, 2-5 fractions of a lower total dose

would improve rodent survival and provide a closer analogue to the effects of radiotherapy observed clinically [193,204]. Radiotherapy is typically given in low doses over multiple fractions to maximize the damage in tumor tissue while minimizing damage in healthy tissue. Low-dose fractionated radiotherapy also allows cells that were less sensitive to the initial radiotherapy session (e.g., cells that are in the S phase of the cell cycle, cells in hypoxic environment) to be targeted at a later time when they may be more responsive (e.g., redistribution of cells to the G2 or mitosis phase of the cell cycle, or reoxygenation of hypoxic cells) [82]. Incorporating the effects of varied cellular radiosensitivity throughout fractionated radiotherapy into subject-specific models may provide a more complete picture of a tumor's radiobiology.

6.3 Future Directions and Recommendations

There are several promising avenues for future research that can address some of the limitations and challenges of this study. One such area is the improvement of the assignment of model parameters. Tumor cellularity is currently the primary tumor characteristic that is used in development of subject-specific models in this study. As there is some ambiguity between the change in ADC and the origin of that change, alternative approaches to assigning tumor cellularity should be investigated in future model development. Similarly, tissue mechanical properties used in the mechanically coupled reaction diffusion model were assigned to five well-characterized tissues from the literature and applied to locations identified within a T_1 map. Assigning tissue mechanical properties from literature values limited this implementation to five different tissues.

Future studies should investigate alternative means to assign a more comprehensive set of tissue properties either directly from imaging data [139,169] or by developing a mechanical property atlas to which individual brains can be registered to.

Another future direction for research is the inclusion of additional imaging measurements which provide further characterization of the tumor into novel biophysical models. Imaging measurements not included in this current study can provide 3D quantification of properties regarding tumor vasculature (e.g., location of vessels [205], vessel volume fraction [56,131], perfusion [56,131], permeability [56,131]) and tumor metabolism (e.g., glucose [206,207], oxygen [133]), that are relevant to tumor growth. For example, imaging measurements of a tumor's vasculature could be used to initialize and constrain models of angiogenesis and vessel regression. Similarly, incorporation of measurements relating to tumor metabolism can provide an initial snapshot of a tumor's environmental conditions, which then can be evolved spatially and temporally using a mathematical model of nutrient delivery and consumptions. Models of tumor metabolism can then be used to also provide a more biologically realistic description of cellular proliferation and death. There are several modeling approaches described in the literature regarding tumor induced angiogenesis [14,15,156] and nutrient utilization [12,99,107], although the existing approaches may need to be adapted for subject-specific applications. We previously performed a preliminary study of a biophysical model of tumor growth consisting of three coupled partial differential equations describing the time dependent changes in tumor cell number, endothelial cell number, and glucose concentration. In addition, glucose concentration was used

to update tumor cell proliferation each iteration. The initial evaluation of this model in one rat showed promising predictions of common glioma characteristics (e.g., highly vascularized and highly proliferating periphery, necrotic interior). However, more work is needed to determine how to completely parameterize the model on an individual basis and validate model results in additional animals. Details of this preliminary study are reported in Appendix D.

A third direction for future investigation is to develop models that incorporate the effects of fractionated radiotherapy and evaluating the model in other cell lines of varying radiosensitivity and radiobiology. As previously mentioned, fractionated radiotherapy is the standard of care for glioblastoma patients and including the unique radiobiology characteristics of fractionated therapy into a subject-specific model may result in a powerful clinical tool. Specifically, modeling the spatial-temporal evolution of responsive cells and resistant cells throughout the course of fractionated radiotherapy may provide insight into the ideal dose and frequency of radiotherapy. Optimized plans could then be evaluated in a murine model in and compared to the response of a cohort receiving a non-optimized radiotherapy plan. Secondly, the radiotherapy model should also be evaluated in cell lines with varied radiobiology (e.g., 9L, F98, U87) [178,208]. Evaluation of radiotherapy models with different cell lines would demonstrate the flexibility of the model characterization of post-radiotherapy tumor growth and demonstrate the potential to model the varied response observed in clinical cases.

6.4 Conclusion

Mathematical models of tumor growth could lead to an advancement in the clinical care of glioblastoma patients through the personalization of their therapy. The models evaluated within this dissertation demonstrate the potential predictive abilities of subject-specific biophysical models. More specifically, it has been shown that the incorporation of a mechanically coupled tumor cell diffusion coefficient and a voxel-specific carrying capacity into a biophysical model of glioma growth can result in the accurate prediction of tumor volume and the distribution of cells within that tumor. Furthermore, subject-specific models of radiotherapy can accurately describe and predict response to radiotherapy at low doses.

APPENDIX A

FINITE DIFFERENCE METHOD FOR THE REACTION DIFFUSION EQUATION

Eq. (A.1) displays the standard reaction diffusion equation which describes the spatial-temporal evolution of tumor cells number and distribution due to and the random movement of tumor cells (diffusion, first term on the right hand side) and the proliferation of cells (reaction, second term on the right hand side):

$$\frac{\partial N(\bar{x},t)}{\partial t} = \nabla \bullet \left(D(\bar{x}) \nabla N(\bar{x},t) \right) + k(\bar{x}) N(\bar{x},t) \left(1 - \frac{N(\bar{x},t)}{\theta} \right), \tag{A.1}$$

where $N(\bar{x},t)$ is the number of tumor cells at three-dimensional position $\bar{x}$ and time *t*, $D(\bar{x})$ is the tumor cell diffusion coefficient at position $\bar{x}$, $k(\bar{x})$ is the net tumor cell proliferation at position $\bar{x}$, and θ is the tumor cell carrying capacity. Eq. (A.1) is solved using a three dimension in space, fully explicit finite difference in time simulation written in Matlab (Mathworks, Natick, MA). The finite difference approximation for the 1D case (say, the *y*-direction) is shown in Eq. (A.2):

$$\begin{aligned} \frac{N(y)^{l+1} - N(y)^{l}}{\Delta t} &= \left(\frac{N(y+1)^{l} - N(y-1)^{l}}{2 \cdot \Delta y} \right) \cdot \left(\frac{D(y+1) - D(y-1)}{2 \cdot \Delta y} \right) \\ &+ D(y) \cdot \left(\frac{N(y+1)^{l} - 2 \cdot N(y)^{l} + N(y-1)^{l}}{\Delta y^{2}} \right) + k(y) N(y)^{l} \left(1 - \frac{N(y)^{l}}{\theta} \right) \end{aligned}, \tag{A.2}$$

where $N(y)^{l+1}$ is the number of tumor cells at the future simulation time point ($l + 1$), $N(y)^{l}$ is the number of tumor cells at the current simulation time point (l), Δt is the simulation time step, and Δy is the grid spacing in the y-direction. For the 3D case, the first and second terms on the right hand side of the equation are repeated in the *x*-direction and *z*-direction, while the third term is just evaluated once at position x, y, z. The simulation has no diffusive flux of tumor cells at the boundaries (Neumann type boundary condition, $\partial N(y)/\partial y = 0$). For the 1D scenario, the first term on the right hand side of Eq. (A.2) is zero due to the boundary condition, while the second diffusion term can be rewritten in terms of $N(y)^{l}$ and $N(y+1)^{l}$ using the boundary condition shown in Eq. (A.3):

$$\frac{N(y+1)^{l} - N(y-1)^{l}}{2\Delta y} = 0 \Rightarrow N(y+1)^{l} = N(y-1)^{l}. \tag{A.3}$$

Inserting Eq. (A.3) into Eq. (A.2) results in the finite difference approximation of the standard reaction diffusion model for a boundary node, Eq. (A.4):

$$\frac{N(y)^{l+1} - N(y)^{l}}{\Delta t} = D(y) \cdot \left(\frac{2 \cdot N(y+1)^{l} - 2 \cdot N(y)^{l}}{\Delta y^{2}} \right) + k(y) N(y)^{l} \left(1 - \frac{N(y)^{l}}{\theta} \right). \tag{A.4}$$

APPENDIX B

IMAGE REGISTRATION

Supplemental Information from:

Hormuth DA, Weis JA, Barnes SL, Miga MI, Rericha EC, Quaranta V, Yankeelov TE. "Predicting in vivo glioma growth with the reaction diffusion equation constrained by quantitative magnetic resonance imaging data". *Physical Biology*. 2015; 12(4)

An intensity based mutual information rigid registration algorithm was used to obtain consistent imaging volumes between the initial imaging session and all subsequent imaging sessions. At the beginning of each imaging session a 3D gradient echo image (*TR*/*TE* = 20/3 ms, FOV = 45 × 45 × 45 mm^3, matrix = 256 × 256 × 128, NEX = 2) was collected (please see Figure A.1). The 3D images collected on subsequent imaging time points were registered to the initial 3D image on Day 0 (Figures A.2 and A.3). This registration provides the translation and rotation matrices to align the animal's position to that obtained at the initial imaging session. These translations and rotations are then applied to the coordinates of Day 0's T_1 weighted and DW-MRI images to obtain the same imaging volume at the current imaging session.

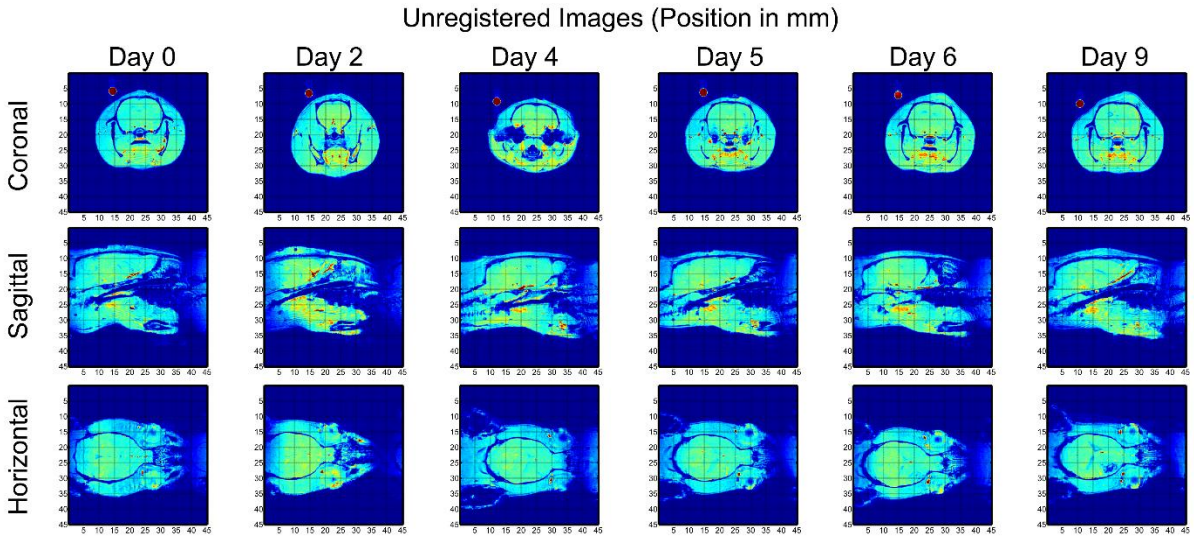

Figure B.1. Unregistered 3D gradient echo. Unregistered 3D gradient echo images are showed for one rat at several imaging time points. The top, middle, and bottom rows represent the coronal, sagittal, and horizontal views, respectively. Note that each imaging session has (sometimes substantial) variation in the positioning of the rat within the scanner.

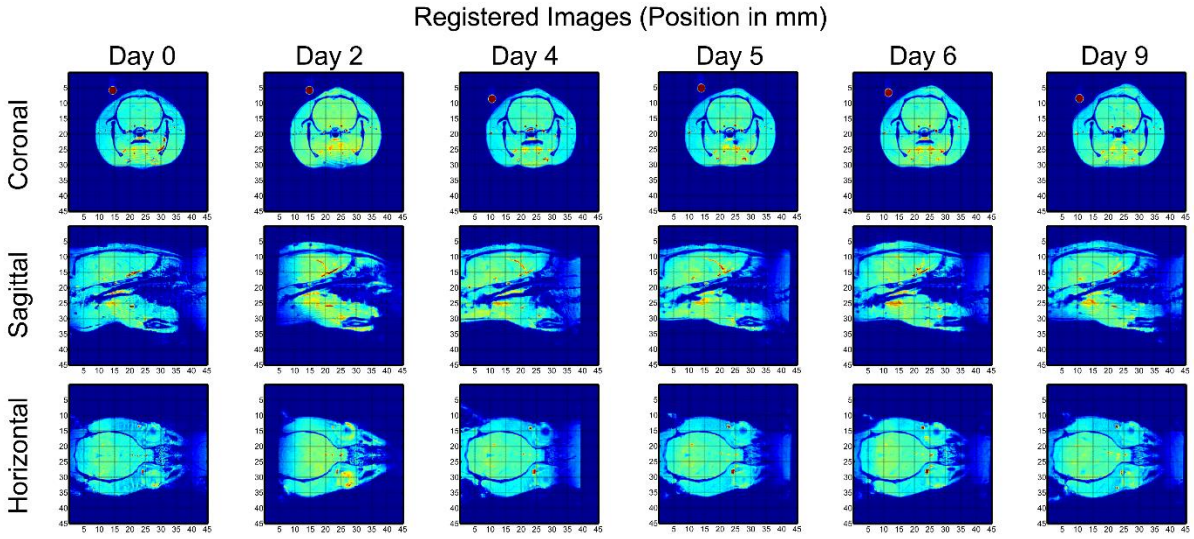

Figure B.2. Registered 3D gradient echo. The registered 3D gradient echo images are shown for one rat at several imaging time points. The top, middle, and bottom rows represent the coronal, sagittal, and horizontal views, respectively. Observe that the alignment of the anatomy from day 0 to day 9 is now quite good with error on the order of the largest imaging voxel (0.352 mm).

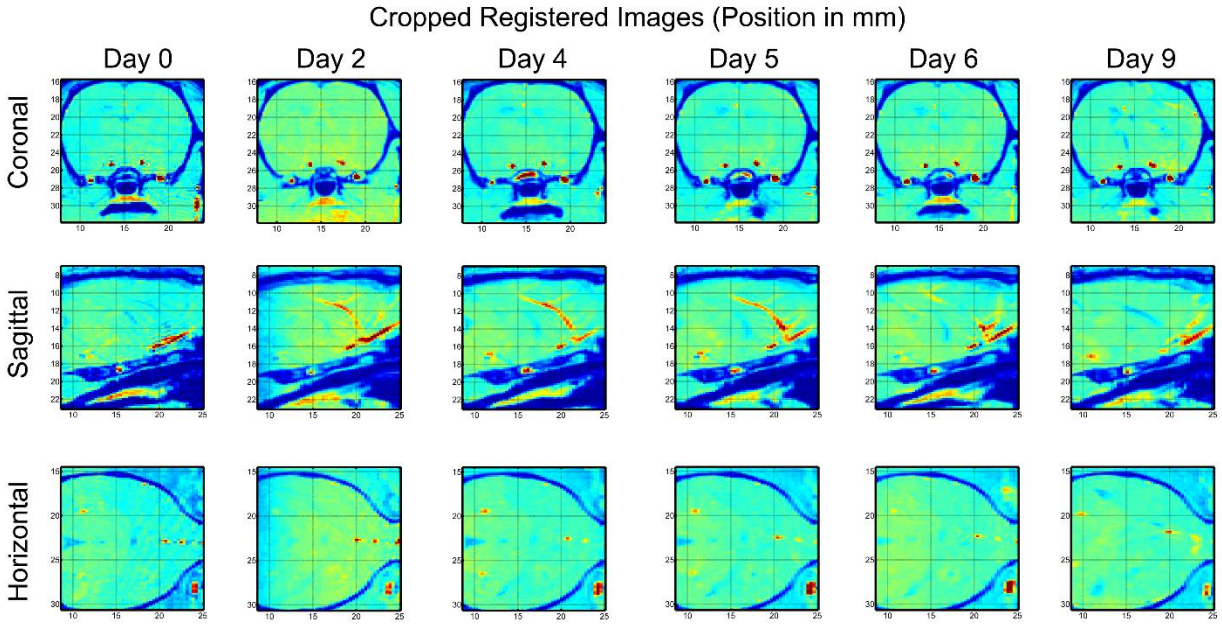

Figure B.3. Cropped registered 3D gradient echo. Cropped versions of the images presented in Supplementary Figure 2 are shown here. It is evident that the registration are quite good as features across days can be compared by their relationship to the gridding overlain for illustrative purposes.

APPENDIX C

FINITE DIFFERENCE APPROXIMATION OF LINEAR ELASTIC ISOTROPIC MECHANICAL EQUILIBRIUM EQUATION

Tissue displacement, $\vec{u}$, is solved for each iteration using the linear elastic isotropic mechanical equilibrium equation:

$$\nabla \cdot G\nabla\vec{u} + \nabla\frac{G}{1-2\nu}\cdot\left(\nabla\cdot\vec{u}\right) - \lambda\nabla N = 0\,, \tag{C.1}$$

where G is the shear modulus, ν is Poisson's ratio, λ represents a tumor cell force coupling constant, and N is the number of tumor cells. Eq. (C.2) through Eq. (C.6) show the expansion of the first term on the left hand side of Eq. (C.1) into its vector components. We first rewrite $\vec{u}$ in terms of its x-, y-, and z-displacement (u_x, u_y, and u_z, respectively), Eq. (C.2):

$$\nabla \cdot G\nabla\vec{u} = \nabla \cdot G\nabla\begin{bmatrix} u_x \\ u_y \\ u_z \end{bmatrix} \tag{C.2}$$

We then calculate the gradient of $\vec{u}$, Eq. (C.3):

$$\nabla \cdot G \begin{bmatrix} \partial u_x / \partial x & \partial u_y / \partial x & \partial u_z / \partial x \\ \partial u_x / \partial y & \partial u_y / \partial y & \partial u_z / \partial y \\ \partial u_x / \partial z & \partial u_y / \partial z & \partial u_z / \partial z \end{bmatrix}, \tag{C.3}$$

and then calculate the divergence of $G\nabla\vec{u}$ using the product rule for derivatives, Eqs. (C.4) and (C.5):

$$\begin{bmatrix} \frac{\partial G}{\partial x} & \frac{\partial G}{\partial y} & \frac{\partial G}{\partial z} \end{bmatrix} \cdot \begin{bmatrix} \partial u_x / \partial x & \partial u_y / \partial x & \partial u_z / \partial x \\ \partial u_x / \partial y & \partial u_y / \partial y & \partial u_z / \partial y \\ \partial u_x / \partial z & \partial u_y / \partial z & \partial u_z / \partial z \end{bmatrix} + G \begin{bmatrix} \frac{\partial}{\partial x} & \frac{\partial}{\partial y} & \frac{\partial}{\partial z} \end{bmatrix} \cdot \begin{bmatrix} \partial u_x / \partial x & \partial u_y / \partial x & \partial u_z / \partial x \\ \partial u_x / \partial y & \partial u_y / \partial y & \partial u_z / \partial y \\ \partial u_x / \partial z & \partial u_y / \partial z & \partial u_z / \partial z \end{bmatrix} \tag{C.4}$$

$$\begin{aligned} &\left(\frac{\partial G}{\partial x}\frac{\partial u_x}{\partial x} + \frac{\partial G}{\partial y}\frac{\partial u_x}{\partial y} + \frac{\partial G}{\partial z}\frac{\partial u_x}{\partial z}\right)\hat{i} + \left(\frac{\partial G}{\partial x}\frac{\partial u_y}{\partial x} + \frac{\partial G}{\partial y}\frac{\partial u_y}{\partial y} + \frac{\partial G}{\partial z}\frac{\partial u_y}{\partial z}\right)\hat{j} + \left(\frac{\partial G}{\partial x}\frac{\partial u_z}{\partial x} + \frac{\partial G}{\partial y}\frac{\partial u_z}{\partial y} + \frac{\partial G}{\partial z}\frac{\partial u_z}{\partial z}\right)\hat{k} \\ &G\left(\frac{\partial^2 u_x}{\partial x^2} + \frac{\partial^2 u_x}{\partial y^2} + \frac{\partial^2 u_x}{\partial z^2}\right)\hat{i} + G\left(\frac{\partial^2 u_y}{\partial x^2} + \frac{\partial^2 u_y}{\partial y^2} + \frac{\partial^2 u_y}{\partial z^2}\right)\hat{j} + G\left(\frac{\partial^2 u_z}{\partial x^2} + \frac{\partial^2 u_z}{\partial y^2} + \frac{\partial^2 u_z}{\partial z^2}\right)\hat{k} \end{aligned} \tag{C.5}$$

Eq. (C.6) shows the final vector notation for Eq. (C.2).

$$\begin{aligned} &\left(\frac{\partial G}{\partial x}\frac{\partial u_x}{\partial x} + \frac{\partial G}{\partial y}\frac{\partial u_x}{\partial y} + \frac{\partial G}{\partial z}\frac{\partial u_x}{\partial z} + G\left(\frac{\partial^2 u_x}{\partial x^2} + \frac{\partial^2 u_x}{\partial y^2} + \frac{\partial^2 u_x}{\partial z^2}\right)\right)\hat{i} + \\ &\left(\frac{\partial G}{\partial x}\frac{\partial u_y}{\partial x} + \frac{\partial G}{\partial y}\frac{\partial u_y}{\partial y} + \frac{\partial G}{\partial z}\frac{\partial u_y}{\partial z} + G\left(\frac{\partial^2 u_y}{\partial x^2} + \frac{\partial^2 u_y}{\partial y^2} + \frac{\partial^2 u_y}{\partial z^2}\right)\right)\hat{j} + \\ &\left(\frac{\partial G}{\partial x}\frac{\partial u_z}{\partial x} + \frac{\partial G}{\partial y}\frac{\partial u_z}{\partial y} + \frac{\partial G}{\partial z}\frac{\partial u_z}{\partial z} + G\left(\frac{\partial^2 u_z}{\partial x^2} + \frac{\partial^2 u_z}{\partial y^2} + \frac{\partial^2 u_z}{\partial z^2}\right)\right)k \end{aligned} \tag{C.6}$$

Eq. (C.7) through Eq. (C.10) show the expansion of the second term on the left hand side of Eq. (C.1) into its vector components. We first rewrite $\vec{u}$ in terms of its *x*-,*y*-, and *z*-displacement (u_x, u_y, and u_z, respectively), Eq. (C.7). We then calculate the divergence of $\vec{u}$, Eq. (C.8),

$$\frac{1}{1-2\nu}\nabla G\nabla\cdot\vec{u}=\frac{1}{1-2\nu}\nabla G\nabla\cdot\begin{bmatrix}u_x\\u_y\\u_z\end{bmatrix}. \tag{C.7}$$

We then calculate the divergence of $\vec{u}$, Eq. (C.8),

$$\nabla G\left[\frac{\partial u_x}{\partial x}+\frac{\partial u_y}{\partial y}+\frac{\partial u_z}{\partial z}\right], \tag{C.8}$$

and then calculate the gradient of $G\nabla\cdot\vec{u}$ using the product rule for derivatives, Eq. (C.9):

$$\begin{aligned}&\frac{\partial G}{\partial x}\left(\frac{\partial u_x}{\partial x}+\frac{\partial u_y}{\partial y}+\frac{\partial u_z}{\partial z}\right)\hat{i}+\frac{\partial G}{\partial y}\left(\frac{\partial u_x}{\partial x}+\frac{\partial u_y}{\partial y}+\frac{\partial u_z}{\partial z}\right)\hat{j}+\frac{\partial G}{\partial y}\left(\frac{\partial u_x}{\partial x}+\frac{\partial u_y}{\partial y}+\frac{\partial u_z}{\partial z}\right)\hat{k}+\\&G\left(\frac{\partial^2 u_x}{\partial x^2}+\frac{\partial^2 u_y}{\partial x\partial y}+\frac{\partial^2 u_z}{\partial x\partial z}\right)\hat{i}+G\left(\frac{\partial^2 u_x}{\partial y\partial x}+\frac{\partial^2 u_y}{\partial y^2}+\frac{\partial^2 u_z}{\partial y\partial z}\right)\hat{j}+G\left(\frac{\partial^2 u_x}{\partial z\partial x}+\frac{\partial^2 u_y}{\partial z\partial y}+\frac{\partial^2 u_z}{\partial z^2}\right)\hat{k}\end{aligned}. \tag{C.9}$$

Eq. (C.10) shows the final vector notation for Eq. (C.7)

$$\left(\frac{\partial G}{\partial x}\left(\frac{\partial u_X}{\partial x}+\frac{\partial u_Y}{\partial y}+\frac{\partial u_Z}{\partial z}\right)+G\left(\frac{\partial^2 u_X}{\partial x^2}+\frac{\partial^2 u_Y}{\partial x\partial y}+\frac{\partial^2 u_Z}{\partial x\partial z}\right)\right)\hat{i}+$$
$$\left(\frac{\partial G}{\partial y}\left(\frac{\partial u_X}{\partial x}+\frac{\partial u_Y}{\partial y}+\frac{\partial u_Z}{\partial z}\right)+G\left(\frac{\partial^2 u_X}{\partial y\partial x}+\frac{\partial^2 u_Y}{\partial y^2}+\frac{\partial^2 u_Z}{\partial y\partial z}\right)\right)\hat{j}+$$
$$\left(\frac{\partial G}{\partial y}\left(\frac{\partial u_X}{\partial x}+\frac{\partial u_Y}{\partial y}+\frac{\partial u_Z}{\partial z}\right)+G\left(\frac{\partial^2 u_X}{\partial z\partial x}+\frac{\partial^2 u_Y}{\partial z\partial y}+\frac{\partial^2 u_Z}{\partial z^2}\right)\right)\hat{k} \quad . \tag{C.10}$$

Eq. (C.11) shows the expansion of the final term on the left hand side of Eq. (C.1).

$$\lambda\nabla N=\lambda\left(\frac{\partial N}{\partial x}\hat{i}+\frac{\partial N}{\partial y}\hat{j}+\frac{\partial N}{\partial z}\hat{k}\right) \tag{C.11}$$

The finite difference approximation of Eq. (C.1) is shown for the *x*-direction ($\hat{i}$ components in Eq. (C.6), Eq. (C.10), and Eq. (C.11)) in Eq. (C.12):

$$G_X(x)\left(\frac{1}{2\Delta x}\right)\left(U_X(x+1)-U_X(x-1)\right)+G_Y(x)\left(\frac{1}{2\Delta y}\right)\left(U_X(y+1)-U_X(y-1)\right)+G_Z(x)\left(\frac{1}{2\Delta z}\right)\left(U_X(z+1)-U_X(z-1)\right)+$$
$$G(x)\left(\frac{1}{\Delta x^2}\right)\left(U_X(x+1)-2\cdot U_X(x)+U_X(x-1)\right)+G(x)\left(\frac{1}{\Delta y^2}\right)\left(U_X(y+1)-2\cdot U_X(y)+U_X(y-1)\right)+$$
$$G(x)\left(\frac{1}{\Delta z^2}\right)\left(U_X(z+1)-2\cdot U_X(z)+U_X(z-1)\right)+\left(\frac{1}{1-2\nu}\right)\left(G_X(x)\left(\frac{1}{2\Delta x}\right)\left(U_X(x+1)-U_X(x-1)\right)\right)+$$
$$\left(\frac{1}{1-2\nu}\right)\left[G_Y(x)\left(\frac{1}{2\Delta y}\right)\left(U_Y(y+1)-U_Y(y-1)\right)+G_Z(x)\left(\frac{1}{2\Delta z}\right)\left(U_Z(z+1)-U_Z(z-1)\right)\right]+$$
$$G(x)\left(\frac{1}{1-2\nu}\right)\left[\left(\frac{1}{\Delta x^2}\right)\left(U_X(x+1)-2\cdot U_X(x)+U_X(x-1)\right)\right]+$$
$$G(x)\left(\frac{1}{1-2\nu}\right)\left(\frac{1}{4\Delta x\Delta y}\right)\left(U_Y(x+1,y+1)-U_Y(x+1,y-1)-U_Y(x-1,y+1)+U_Y(x-1,y-1)\right)+$$
$$G(x)\left(\frac{1}{1-2\nu}\right)\left(\frac{1}{4\Delta x\Delta z}\right)\left(U_Z(x+1,z+1)-U_Z(x+1,z-1)-U_Z(x-1,z+1)+U_Z(x-1,z-1)\right)$$
$$-\lambda\left(\frac{1}{2\Delta x}\right)\left(N(x+1)-N(x-1)\right) \quad , \tag{C.12}$$

where G_x G_y, and G_z represent the derivative of G in the x-, y-, and z- directions, *respectively*, U_x, U_y, and U_z are the 3D matrices of the displacement in the x-, y-, and z-directions. In this approximation U_x, U_y, and U_z are unknown. Eq. (C.12) is grouped by each displacement term to determine coefficients for each displacement term. Eq. (C.13) shows an example of this grouping for U_x(x).

$$\left(-2\cdot G(x)\left(\frac{1}{\Delta x^2}+\frac{1}{\Delta y^2}+\frac{1}{\Delta z^2}+\frac{1}{(1-2\nu)\cdot\Delta x^2}\right)\right)U_x \tag{C.13}$$

The coefficients are also determined for the y-direction and z-direction versions of Eq. (C.12) to build a square $3n \times 3n$ coefficient matrix M, where n is the number of nodes in the simulation. Rows 1 through n of M represent coefficients for the x-direction, rows $n + 1$ through $2n$ of M represent the coefficients for the y-direction, and $2n + 1$ through $3n$ of M represent the coefficients for the z-direction. The finite difference approximation of Eq. (C.1) can then be written (and solved) in the matrix form shown in Eq. (C.14):

$$[M]\begin{Bmatrix}u_x\\u_y\\u_z\end{Bmatrix}=\lambda\begin{Bmatrix}\partial N/\partial x\\\partial N/\partial y\\\partial N/\partial z\end{Bmatrix}+\begin{Bmatrix}BC_x\\BC_y\\BC_z\end{Bmatrix}, \tag{C.14}$$

where BC_x, BC_y, and and BC_z represent the boundary conditions in the x-, y-, and z-directions, respectively. In the finite difference simulation, we assumed tissue displacement in the direction of the boundary was zero, while displacement in the other orthogonal directions were unknown.

Eq. (C.14) was solved using LU decomposition. Eq. (C.15) details the composition of each component in Eq. (C.14):

$$\begin{bmatrix} M_{x,1,1} & \dots & M_{x,1,n} & \dots & M_{x,1,2n} & \dots & M_{x,1,3n} \\ \dots & \dots & \dots & \dots & \dots & \dots & \dots \\ M_{x,n,1} & \dots & M_{x,n,n} & \dots & M_{x,n,2n} & \dots & M_{x,n,3n} \\ M_{y,1,1} & \dots & M_{y,1,n} & \dots & M_{y,1,2n} & \dots & M_{y,1,3n} \\ \dots & \dots & \dots & \dots & \dots & \dots & \dots \\ M_{y,n,1} & \dots & M_{y,n,n} & \dots & M_{y,n,2n} & \dots & M_{y,n,3n} \\ M_{z,1,1} & \dots & M_{z,1,n} & \dots & M_{z,1,2n} & \dots & M_{z,1,3n} \\ \dots & \dots & \dots & \dots & \dots & \dots & \dots \\ M_{z,n,1} & \dots & M_{z,n,n} & \dots & M_{z,n,2n} & \dots & M_{z,n,3n} \end{bmatrix} \begin{Bmatrix} u_{x,1} \\ \dots \\ u_{x,n} \\ u_{y,1} \\ \dots \\ u_{y,n} \\ u_{z,1} \\ \dots \\ u_{z,n} \end{Bmatrix} = \lambda \begin{Bmatrix} \partial N_1/\partial x \\ \dots \\ \partial N_n/\partial x \\ \partial N_1/\partial y \\ \dots \\ \partial N_n/\partial y \\ \partial N_1/\partial z \\ \dots \\ \partial N_n/\partial z \end{Bmatrix} - \begin{Bmatrix} BC_{x,1} \\ \dots \\ BC_{x,n} \\ BC_{y,1} \\ \dots \\ BC_{y,n} \\ BC_{z,1} \\ \dots \\ BC_{z,n} \end{Bmatrix} \tag{C.15}$$

The first row represents the extracted coefficients from Eq. (C.12) for the finite difference approximation centered about node 1, referring to tissues displacements in the *x*-direction (columns 1 through *n*), *y*-direction (columns $n + 1$ through $2n$), and *z*-direction (columns $2n + 1$ through $3n$). Figure C.1 shows the non-zero components of *M*. *M* is a sparse, banded matrix.

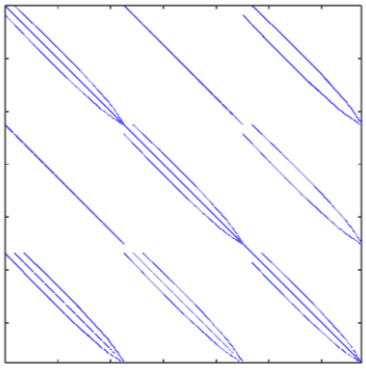

Figure C.1. Visualization of coefficient matrix *M*. *M* is a sparse banded matrix consisting of up to 19 coefficients in each row. For this particularly rat, *M* was 67537 × 67537 with 902289 non-zero coefficients (~2% non-zero entries).

APPENDIX D

IN VIVO IMAGING TO INITIALIZE A BIOPHYSICAL MODEL OF TUMOR GROWTH: PRELIMINARY RESULTS.

Text for Appendix D adapted from:

Hormuth DA, Yankeelov TE. "*In vivo* Imaging to Initialize a Biophysical Model of Tumor Growth: Preliminary Results." *Biomedical Sciences and Engineering Conference (BSEC).* 2013; pages 1-4.

D.1 Abstract

Recent advances in MRI and PET have increased the availability of noninvasive measurements of the molecular, cellular, and physiological characteristics of tumors. It may be possible to incorporate these measurables into realistic biophysical models that can then be used to predict tumor growth and therapy response on an individual basis. Here we incorporate quantitative imaging data acquired during the course of a tumor development in rat model of glioma. Early measurements are used to initialize and constrain a biophysical model to predict tumor status at later time points. The initial results show a promising ability to use early time point data to predict later time point tumor size, cellularity, and distribution.

D.2 Introduction

Mathematical modeling of tumors has a long and rich history [5]**.** However, current models are limited in their practical applicability as they require input data that are extraordinarily difficult

to obtain in an intact organism with any reasonable spatial resolution, especially at multiple time points. Consequently, there has been very little application of such models to clinical questions and virtually no incorporation into clinical trials. However, in recent years there have been dramatic increases in the range and quality of information available from non-invasive imaging methods. In particular, magnetic resonance imaging (MRI) and positron emission tomography (PET) have matured to the point where they can provide noninvasive, quantitative, and 3D characterizations of, for example, blood flow, vessel permeability, blood volume, cellularity, hypoxia, metabolism, and cell proliferation. This rich array of information provides compelling motivation for integrating imaging data into mathematical models of tumor treatment response. Furthermore, repeated measurements can be made without disturbing the system at the time of diagnosis and early in the course of treatment, and these data can be incorporated into models to predict the outcome of the therapy. Imaging allows models to be initialized and constrained with patient specific data, as opposed to models that are driven by data obtained from in vitro assays or groups of animals, which are the almost exclusive approaches for current mathematical modeling studies. Only by parameterizing models by data that are readily accessible and specific to the individual, can they be translated into clinical practice.

We [1-2] and others [3-5] have recently described a series of models (and associated experiments) that are parameterized strictly in terms of imaging data so that the status of a tumor at a future time point can be estimated from imaging data obtained at an earlier time point. In this

contribution, we provide preliminary results indicating that quantitative, non-invasive imaging data acquired early in the tumor life cycle can be used to predict tumor status at later time points.

D.3 Methods

D.3.1. Animal Methods

Male Sprague-Dawley rats (n = 6, 250 g) were anesthetized, given analgesic and inoculated with C6 glioma cells (1 x 10^5 cells) *via* stereotaxic injection. One jugular catheter was placed in each rat within 48 hours of imaging for delivery of the common (clinical approved) contrast agent Magnevist (Bayer, Wayne, New Jersey). All experimental procedures were approved by Vanderbilt University's Institutional Animal Care and Use Committee.

D.3.2. Imaging Data Acquisition

Rats were imaged at using a Varian 4.7-T Inova imaging system (Palo Alto, CA) with diffusion weighted MRI (DW-MRI) and dynamic contrast enhanced MRI (DCE-MRI) on days 9, 10, 11, 13, 15 and 17. Figure D.1 shows example parameter maps obtained from DW-MRI and DCE-MRI data. DW-MRI data was acquired with three *b*-values (50, 300, and 800 s/mm^2) to calculate the *apparent* diffusion coefficient (ADC). A three parameter model (K^{trans}, v_e, and v_p) consisting of plasma and extravascular-extracellular compartments was fit to the DCE-MRI data acquired before and after injection of 200 µl bolus of 0.05 mmol kg^{-1} Magnevist over 5 seconds.

K^{trans} describes the movement of the contrast agent from the vascular compartment (v_p) to the extravascular (v_e) compartments. The post-contrast images were used to define the tumor region of interest. 3D gradient echo images were used to registered images using a rigid registration algorithm. All images were acquired with a voxel size of 250 × 250 × 1000 μm.

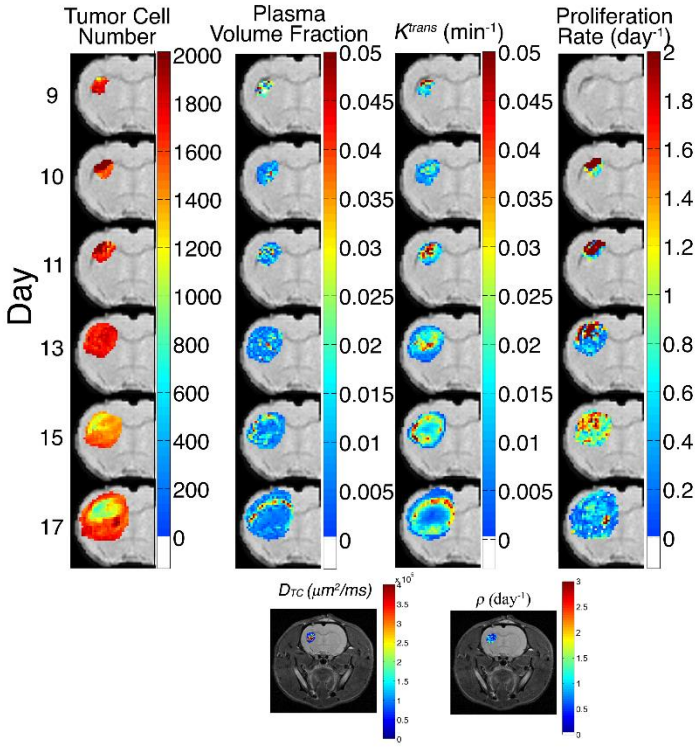

Figure D.1. Example parameter maps obtained from experimentally measured MRI data on days 9, 10, 11, 13, 15, and 17 after tumor inoculation. The first column presents maps of tumor cell number (derived from DW-MRI data), while the middle two columns present the plasma volume fraction and K^{trans} maps derived from DCE-MRI data. The last column displays the proliferation rate map which is derived from sequential DW-MRI data. Finally, the bottom two panels depict the D_{TC} and ρ values calculated via the CIMPLE map (please see text for details). The first three time points provide the data to initialize and constrain the model system, while the last three time points provide the experimental data to which the predicted results are compared.

D.3.3. The Biophysical Model

The imaging data was then incorporated into a model consisting of three coupled partial differential equations describing the time dependent changes in tumor cell number (Eq. (D.1)), endothelial cell number (Eq. (D.2)), and glucose concentration (Eq. (D.3)), which was then solved using the finite difference method.

$$\frac{\partial N_{TC}(\bar{x},t)}{\partial t} = \nabla \bullet [D_{TC} \nabla N_{TC}(\bar{x},t)] + k_{p,TC}(\bar{x},t) N_{TC}(\bar{x},t)\left(1 - \frac{N_{TC}(\bar{x},t)}{\theta}\right) - k_{d,TC}(\bar{x},t) N_{TC}(\bar{x},t) \tag{D.1}$$

$$\frac{\partial N_{EC}(\bar{x},t)}{\partial t} = N_{EC}(\bar{x},t) \cdot (\mu_{ag} \cdot G(\bar{x},t) - \mu_{reg} \cdot R(\bar{x},t))$$

$$G(\bar{x},t) = \begin{cases} 1, & N_{TC}(\bar{x},t) \big/ \theta \geq .25 \\ 0, & else \end{cases} \tag{D.2}$$

$$R(\bar{x},t) = \begin{cases} 1, & N_{TC}(\bar{x},t) \big/ \theta \geq .90 \\ 0, & else \end{cases}$$

$$\frac{\partial C_g(\bar{x},t)}{\partial t} = \nabla \bullet [D_g \nabla C_g(\bar{x},t)] + K^{trans}(\bar{x},t) \cdot C_{g,p} - \frac{C_g(\bar{x},t)}{C_{g,p}}\left(N_{TC}(\bar{x},t) \cdot \gamma_g(\bar{x},t)\right) \tag{D.3}$$

Eq. (D.1) describes the change in tumor cell number (N_{TC}) over time due to random movement of tumor cells (D_{TC} = tumor cell diffusion), proliferation, $k_{p,TC}$, by logistic growth (θ = carrying capacity), and death, $k_{d,TC}$. Outside of the tumor ROI, healthy brain cell numbers are assumed to remain constant until tumor cells invade into those voxels causing a decrease in healthy brain cells equal to increase in tumor cells. Eq. (D.2) describes the change in endothelial cell number (N_{EC})

over time, incorporates a rate of angiogenesis, μ_{ag}, and a rate of regression, μ_{reg}. New vessels are assumed to develop when tumor cells occupy at least 25% of a voxel. Conversely, vessel regression is assumed to occur due to occlusion by growing tumor cells, which may occur when tumor cells occupy at least 90% of its voxel. Eq. (D.3) describes the time dependent change in glucose concentration (C_g) which consists of random movement of glucose, D_g, delivery of glucose by vasculature, ($C_{g,p}$ = average glucose in plasma), and consumption of glucose by both normal brain and tumor cells, γ_g.

D.3.4. Initializing and Running the Biophysical Model

Table D.1. Model Parameter Description and Source

Parameter	Description	Source
N_{TC}	Tumor cell number	DW-MRI [63]
D_{TC}	Tumor cell diffusion coefficient	DW-MRI [25]
$k_{p,TC}$	Tumor cell proliferation rate	DW-MRI [25]
θ	Carrying capacity	Literature [135–137]
$k_{d,TC}$	Tumor cell death rate	Literature [63]
N_{EC}	Endothelial cell number	v_p, DCE-MRI
μ_{ag}	Vessel angiogenesis rate	DCE-MRI
μ_{reg}	Vessel regression rate	DCE-MRI
C_g	Glucose concentration	Literature [210]
D_g	Diffusion coefficient of glucose	Literature [210]
K^{trans}	Delivery rate of glucose	DCE-MRI
$C_{g,p}$	Glucose concentration in plasma	Blood Draw
γ_g	Consumption rate of glucose	Literature [210]
$k_{p,vg}$	Value of k averaged over tumor	DW-MRI [25]
$C_{g,avg}$	Average of C_g over tumor	FDG-PET or literature [211]
k_{death}	Death rate of tumor cells	DW-MRI, Eq.

Table D.1 summarizes how parameters from Eqs. (D.1) - (D.3) were assigned from imaging data, the literature, or estimated. N_{TC} was calculated from ADC maps as previously described [63]. ADC maps were also used to determine D_{TC} and $k_{p,TC}$ following the method by Ellingson *et al* [25]. Average cell volume and $k_{d,TC}$ were assigned from literature [63]. v_p provided N_{EC}, whereas μ_{ag} was calculated from voxels where v_p increased between day 9 and 10 and μ_{reg} was calculated from the voxels where v_p decreased between day 9 and 10. Additionally, calculated changes in N_{EC} were used to assign equal growth and regression in K^{trans} and v_p. The initial distribution of C_g, D_g, $C_{g,p}$, and γ_g were all assigned from the literature [8-9].

Simulations started at day 9 and continued till day 17. From day 9 to 10, only solutions for N_{TC} and N_{EC} were calculated while C_g remained constant. Starting at day 10, solutions for N_{TC}, N_{EC}, and C_g were calculated. Starting from day 10 $k_{p,TC}$ was assigned based on local C_g. When $C_g > C_{g,critical}$ cells proliferated at a rate $k_{p,TC}$ described in Eq. (D.4); whereas, when $C_g < C_{g,critical}$, cells ceased to proliferate ($k_{p,TC} = 0$) and underwent apoptosis at a rate $k_{d,TC}$.

$$k_{p,TC}\left(\bar{x},t\right) = k_{p,avg} \cdot \left(\frac{C_g\left(\bar{x},t\right)}{C_{g,avg}} \right) \tag{D.4}$$

Additionally, tumor cells within a voxel are assumed to consume glucose both aerobically and anaerobically. Therefore γ_g is a weighted sum of aerobic and anaerobic consumption rates which is assigned based on local vascular status. To determine the weights, the maximum and minimum values for v_p were assigned from the imaging data. If a voxel exceeded the maximum value, the

voxel will consume glucose aerobically. Similarly, if the voxel was less than the minimum value, the voxel consumed glucose anaerobically. Consumption rates between the upper and lower limits were assigned using Eq. (D.5):

$$\gamma_g\left(\bar{x},t\right)=\gamma_{g,anaerobic}\cdot\left(1-\frac{v_p\left(\bar{x},t\right)}{v_{p,\max}}\right)+\gamma_{g,aerobic}\cdot\left(\frac{v_p\left(\bar{x},t\right)}{v_{p,\max}}\right) \tag{D.5}$$

where $v_{p,max}$ is the upper limit observed in DCE-MRI data. Eqs. (D.1) and (D.2) were solved using a forward Euler finite difference approximation; while Eq. (D.3) was implemented using the Crank-Nicolson method. All simulations were performed in Matlab R2102a (Natick, MA) with a computation time of 3.5 hour running on an Intel i5 2520M, 2 cores (2.5GHz), 4 threads, and 8 GB of ram.

D.3.5. Comparing Model Predictions to Experimental Data

Agreement between predicted and observed tumor volume and cell number was assessed by the Pearson and concordance correlation coefficients (PCC and CCC, respectively). To assess the sensitivity of the model to noise in the imaging data measurements, a Monte Carlo simulation was performed. Variability in imaging data measurements for ADC, K^{trans}, and v_e were assigned from a previous reproducibility study [212].

D.4 Results

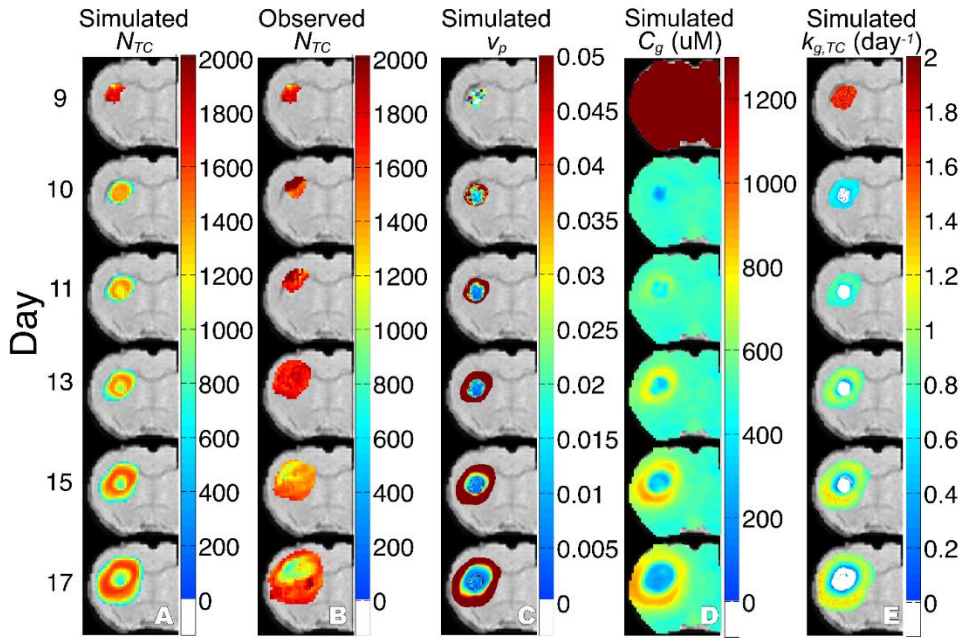

Figure D.2. Simulated and observed model parameters. Simulated columns (A, C-E) and observed tumor cell growth column (B) over 6 imaging time points. As the tumor grows and expands into the brain over time columns (A and B), vascularity column (C), glucose column (D), and proliferation rate column (E) increase on the periphery, while decreasing in the core of the tumor. Observe that, while the exact distribution of tumor cells between the simulated (i.e., predicted) and experimental data do differ, the general features match including the appearance of a necrotic core (see the last panels of columns A and B).

Figure D.2 shows model parameters from the central tumor slice for both simulated (columns A and C-E) and experimental (B) tumor growths at six time points. Simulated tumor growth resulted in asymmetric tumors which developed necrotic cores with increased vascularity on the periphery. Columns A and B show the simulated and observed tumor cell number at six

imaging time points. Both observed and simulated tumors grow asymmetrically and develop necrotic cores. Figure D.3 shows the simulated and observed tumor cell number and volume from

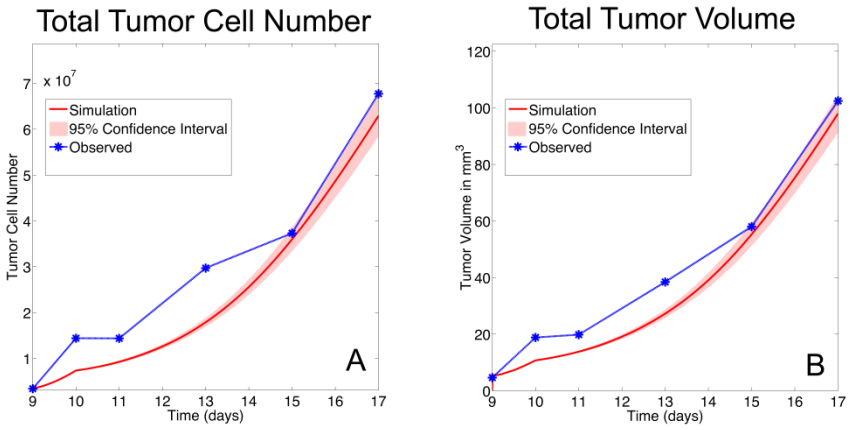

Figure D.3. Simulated and observed tumor cell number and volume. Panel (A) shows simulated tumor cell number (red solid line) and the 95% confidence interval (shaded) from days 9-17. The blue line represents the observed tumor cell number assessed from DW-MRI. 95% Confidence intervals were calculated from a Monte Carlo simulation (N = 50). Panel (B) shows simulated tumor volume (red solid line) and the 95% confidence interval (shaded) from days 9-17. The blue line represents the observed tumor volume calculated from DCE-MRI ROIs.

day 9-17. Additionally, the 95% confidence intervals for the simulated tumor growth includes the values for both tumor cell number and volume at day 17. The linear relationship between simulated and observed cell number and total tumor volume is reflected by PCCs of 0.98 and 0.99, respectively. Similarly, the agreement between simulated and observed cell number and total tumor volume resulted in CCCs of 0.81 and 0.82. Figure D.4 presents a comparison between the predicted and experimentally measured tumor cell number and distribution at day 17. Note that

while there are substantial differences between the two, the gross features of the tumor (including the presence of a necrotic core) are seen in both sets.

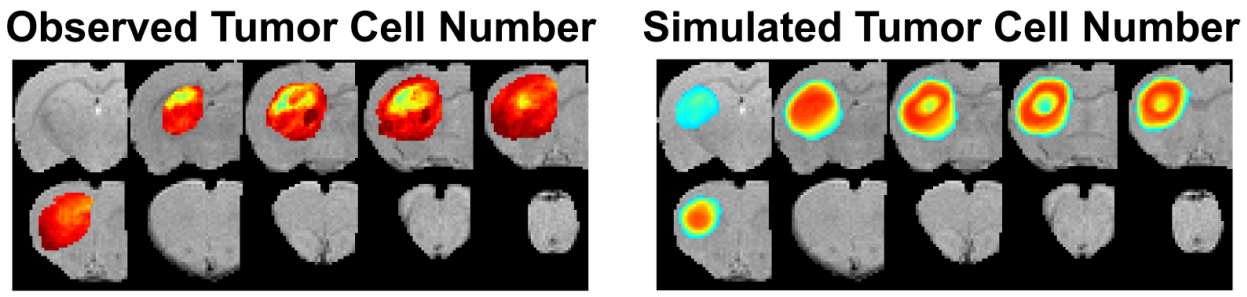

Figure D4. Simulated and observed final tumor volume. The left panels display day 17 measured tumor cell number (as estimated from the DW-MRI data) superimposed on 10 consecutive slices of the rat brain, while the right panels display the predicted tumor cell number for these same slices. Both tumor growths experience similar spread throughout the brain. While the simulated (i.e., predicted) tumor growth is greater than the actual tumor growth (i.e., it covers more slices and is therefore larger), there is a general correspondence between size and spatial distribution of the tumor cells. Note especially the prediction of a necrotic core which matches that seen in the experimental data.

As the tumor expands, new blood vessels are recruited on the periphery and existing vessels collapse within the center resulting in a decrease in available nutrients. These growth patterns result in highly proliferative tumor cells at the periphery, a group of necrotic cells at the center, and a group of slowly proliferating in between, similar to what is seen *in vivo* [213].

D.5 Discussion and Conclusion

The high PCCs suggest a strong linear relationship between predicted and observed values. Importantly, the predicted tumor resulted in a necrotic region which was also observed *in vivo*. Further characterization of this model will include determining the sensitivity of the model to both parameters from imaging data as well as those assumed from the literature. Ongoing work is focused on expanding the model to include oxygen (from quantitative BOLD data) status and the incorporation of competition between healthy brain cells and tumor cells for resources and space. Including these elements will allow for the development of a more realistic description of tumor metabolism which we hypothesize will increase the accuracy of the modeling predictions. Furthermore, this work needs to be applied and evaluated in more animals.

D.6 Acknowledgements

We thank the National Institutes of Health for funding through NCI R01CA138599, NCI R25CA136440, and NCI R21CA169387.

REFERENCES

[1] Institute NC. SEER Stat Fact Sheets: Brain and Other Nervous System Cancer [Internet]. Bethesda, MD; 2015. Available from: http://seer.cancer.gov/statfacts/html/brain.html

[2] Omuro A, LM D. Glioblastoma and other malignant gliomas: A clinical review. *JAMA*. 2013 Nov 6;**310**(17):1842–50.

[3] Moding EJ, Kastan MB, Kirsch DG. Strategies for optimizing the response of cancer and normal tissues to radiation. *Nat Rev Drug Discov*. 2013;**12**(7):526–42.

[4] Fischer H, Hartmann GH, Sturm V, Schwechheimer K, Krauss O, Schackert G, et al. In vitro model for the response to irradiation of different types of human intracranial tumours. *Acta Neurochir (Wien)*. 1987;**85**(1-2):46–9.

[5] Byrne HM. Dissecting cancer through mathematics: from the cell to the animal model. *Nat Rev Cancer*. Nature; 2010;**10**(3):221–30.

[6] Deisboeck TS, Wang Z, Macklin P, Cristini V. Multiscale cancer modeling. *Annu Rev Biomed Eng*. 2011;**13**:127–55.

[7] Marušić M, Bajzer Ž, Freyer JP, Vuk-Pavlović S. Analysis of growth of multicellular tumour spheroids by mathematical models. *Cell Prolif*. 1994;**27**(2):73–94.

[8] Kim B, Chenevert TL, Ross BD. Growth kinetics and treatment response of the intracerebral rat 9L brain tumor model: a quantitative in vivo study using magnetic resonance imaging. *Clin Cancer Res*. 1995;**1**(6):643–50.

[9] Atuegwu NC, Arlinghaus LR, Li X, Welch EB, Chakravarthy BA, Gore JC, et al. Integration of diffusion-weighted MRI data and a simple mathematical model to predict breast tumor cellularity during neoadjuvant chemotherapy. *Magn Reson Med*. 2011;**66**(6):1689–96.

[10] Paulus W, Peiffer J. Intratumoral Histologic Heterogeneity of Gliomas - A Quantitative Study. *Cancer*. 1989;**64**(2):442–7.

[11] Wagner M, Nafe R, Jurcoane A, Pilatus U, Franz K, Rieger J, et al. Heterogeneity in malignant gliomas: a magnetic resonance analysis of spatial distribution of metabolite changes and regional blood volume. *J Neurooncol*. 2011;**103**(3):663–72.

[12] Gerlee P, Anderson ARA. An evolutionary hybrid cellular automaton model of solid tumour growth. *J Theor Biol*. 2007;**246**(4):583–603.

[13] Cai Y, Xu S, Wu J, Long Q. Coupled modelling of tumour angiogenesis, tumour growth and blood perfusion. *J Theor Biol*. 2011;**279**(1):90–101.

[14] Anderson ARA, Chaplain MAJ. Continuous and discrete mathematical models of tumor-induced angiogenesis. *Bull Math Biol*. 1998;**60**(5):857–99.

[15] McDougall SR, Anderson ARA, Chaplain MAJ. Mathematical modelling of dynamic adaptive tumour-induced angiogenesis: Clinical implications and therapeutic targeting strategies. *J Theor Biol*. 2006;**241**(3):564–89.

[16] Yankeelov TE, Atuegwu N, Hormuth DA, Weis JA, Barnes SL, Miga MI, et al. Clinically Relevant Modeling of Tumor Growth and Treatment Response. *Sci Transl Med*. 2013;**5**(187):187ps9–187ps9.

[17] Gore JC, Manning HC, Quarles CC, Waddell KW, Yankeelov TE. Magnetic resonance in the era of molecular imaging of cancer. *Magn Reson Imaging*. 2011;**29**(5):587–600.

[18] Kubota K. From tumor biology to clinical Pet: a review of positron emission tomography (PET) in oncology. *Ann Nucl Med*. 2001;**15**(6):471–86.

[19] Weis JA, Miga MI, Arlinghaus LR, Li X, Chakravarthy AB, Abramson V, et al. A mechanically coupled reaction diffusion model for predicting the response of breast tumors to neoadjuvant chemotherapy. *Phys Med Biol*. 2013;**58**(17):5851–66.

[20] Liu Y, Sadowski SM, Weisbrod AB, Kebebew E, Summers RM, Yao J. Patient specific tumor growth prediction using multimodal images. *Med Image Anal*. 2014;**18**(3):555–66.

[21] Harpold HLP, Alvord ECJ, Swanson KR. The Evolution of Mathematical Modeling of Glioma Proliferation and Invasion. *J Neuropathol Exp Neurol*. 2007;**66**(1).

[22] Swanson KR, Rostomily RC, Alvord EC. A mathematical modelling tool for predicting survival of individual patients following resection of glioblastoma: a proof of principle. *Br J Cancer*. 2008;**98**(1):113–9.

[23] Neal ML, Trister AD, Cloke T, Sodt R, Ahn S, Baldock AL, et al. Discriminating Survival Outcomes in Patients with Glioblastoma Using a Simulation-Based, Patient-Specific Response Metric. *PLoS One*. 2013;**8**(1):e51951.

[24] Jbabdi S, Mandonnet E, Duffau H, Capelle L, Swanson KR, Pélégrini-Issac M, et al. Simulation of anisotropic growth of low-grade gliomas using diffusion tensor imaging. *Magn Reson Med*. 2005;**54**(3):616–24.

[25] Ellingson B, LaViolette P, Rand SD, Malkin MG, Connelly JM, Mueller WM, et al. Spatially quantifying microscopic tumor invasion and proliferation using a voxelwise solution to a glioma growth model and serial diffusion MRI. *Magn Reson Med*. 2011;**65**(4):1131–43.

[26] Hogea C, Davatzikos C, Biros G. An image-driven parameter estimation problem for a reaction diffusion glioma growth model with mass effects. *J Math Biol*. 2008;**56**(6):793–825.

[27] Konukoglu E, Clatz O, Menze BH, Stieltjes B, Weber M-A, Mandonnet E, et al. Image Guided Personalization of Reaction diffusion Type Tumor Growth Models Using Modified Anisotropic Eikonal Equations. Medical Imaging, IEEE Transactions on. 2010. p. 77–95.

[28] Clatz O, Sermesant M, Bondiau P-Y, Delingette H, Warfield SK, Malandain G, et al. Realistic simulation of the 3-D growth of brain tumors in MR images coupling diffusion with biomechanical deformation. Medical Imaging, IEEE Transactions on. 2005. p. 1334–46.

[29] Bondiau P-Y, Clatz O, Sermesant M, Marcy P-Y, Delingette H, Frenay M, et al. Biocomputing: numerical simulation of glioblastoma growth using diffusion tensor imaging. *Phys Med Biol*. 2008;**53**(4):879–93.

[30] Chinot O, Macdonald D, Abrey L, Zahlmann G, Kerloëguen Y, Cloughesy T. Response Assessment Criteria for Glioblastoma: Practical Adaptation and Implementation in Clinical Trials of Antiangiogenic Therapy. *Curr Neurol Neurosci Rep*. 2013;**13**(5):1–11.

[31] Macdonald DR, Cascino TL, Schold SC, Cairncross JG. Response criteria for phase II studies of supratentorial malignant glioma. *J Clin Oncol*. 1990;**8**(7):1277–80.

[32] Galanis E, Buckner JC, Maurer MJ, Sykora R, Castillo R, Ballman K V, et al. Validation of neuroradiologic response assessment in gliomas: Measurement by RECIST, two-dimensional, computer-assisted tumor area, and computer-assisted tumor volume methods. *Neuro Oncol*. 2006;**8**(2):156–65.

[33] Warner E. Breast-Cancer Screening. *N Engl J Med*. 2011;**365**(11):1025–32.

[34] Bertout JA, Patel SA, Simon MC. Hypoxia and Metabolism Series - Timeline The impact of O(2) availability on human cancer. *Nat Rev Cancer*. 2008;**8**(12):967–75.

[35] Morrow M, Waters J, Morris E. MRI for breast cancer screening, diagnosis, and treatment. *Lancet*. 19AD;**378**(9805):1804–11.

[36] Villers A, Lemaitre L, Haffner J, Puech P. Current status of MRI for the diagnosis, staging and prognosis of prostate cancer: implications for focal therapy and active surveillance. *Curr Opin Urol*. 2009;**19**(3).

[37] Law M, Yang S, Wang H, Babb JS, Johnson G, Cha S, et al. Glioma Grading: Sensitivity, Specificity, and Predictive Values of Perfusion MR Imaging and Proton MR Spectroscopic Imaging Compared with Conventional MR Imaging. *Am J Neuroradiol*. 2003;**24**(10):1989–98.

[38] Takayasu K, Furukawa H, Wakao F, Muramatsu Y, Abe H, Terauchi T, et al. CT diagnosis of early hepatocellular carcinoma: sensitivity, findings, and CT-pathologic correlation. *Am*

J Roentgenol. 1995;**164**(4):885–90.

[39] Pappa VI, Hussain HK, Reznek RH, Whelan J, Norton AJ, Wilson AM, et al. Role of image-guided core-needle biopsy in the management of patients with lymphoma. *J Clin Oncol*. 1996;**14**(9):2427–30.

[40] Lewin JS, Nour SG, Duerk JL. Magnetic Resonance Image-Guided Biopsy and Aspiration. *Top Magn Reson Imaging*. 2000;**11**(3).

[41] Berg WA. Image-guided breast biopsy and management of high-risk lesions. *Radiol Clin North Am*. 2004;**42**(5):935–46.

[42] Barone DG, Lawrie TA, Hart MG. Image guided surgery for the resection of brain tumours. *Cochrane database Syst Rev*. 2014;**1**:CD009685.

[43] Yap JT, Carney JPJ, Hall NC, Townsend DW. Image-Guided Cancer Therapy Using PET/CT. *Cancer J*. 2004;**10**(4).

[44] Goldberg SN. Comparison of Techniques for Image-guided Ablation of Focal Liver Tumors. *Radiology*. 2002;**223**(2):304–7.

[45] Lencioni R, Cioni D, Pina C Della, Crocetti L. Hepatocellular carcinoma: new options for image-guided ablation. *J Hepatobiliary Pancreat Sci*. 2010;**17**(4):399–403.

[46] Köhler MO, Mougenot C, Quesson B, Enholm J, Le Bail B, Laurent C, et al. Volumetric HIFU ablation under 3D guidance of rapid MRI thermometry. *Med Phys*. 2009;**36**(8).

[47] Jaffray DA. Image-guided radiotherapy: from current concept to future perspectives. *Nat Rev Clin Oncol*. 2012;**9**(12):688–99.

[48] Zaidi H, Vees H, Wissmeyer M. Molecular PET/CT Imaging-Guided Radiation Therapy Treatment Planning. *Acad Radiol*. 2009;**16**(9):1108–33.

[49] Jaffray D, Kupelian P, Djemil T, Macklis RM. Review of image-guided radiation therapy. *Expert Rev Anticancer Ther*. 2007;**7**(1):89–103.

[50] Wen PY, Macdonald DR, Reardon DA, Cloughesy TF, Sorensen AG, Galanis E, et al. Updated Response Assessment Criteria for High-Grade Gliomas: Response Assessment in Neuro-Oncology Working Group. *J Clin Oncol*. 2010;**28**(11):1963–72.

[51] Therasse P, Arbuck SG, Eisenhauer EA, Wanders J, Kaplan RS, Rubinstein L, et al. New Guidelines to Evaluate the Response to Treatment in Solid Tumors. *J Natl Cancer Inst*. 2000;**92**(3):205–16.

[52] Eisenhauer EA, Therasse P, Bogaerts J, Schwartz LH, Sargent D, Ford R, et al. New response evaluation criteria in solid tumours: Revised RECIST guideline (version 1.1). *Eur J Cancer*. 2016;**45**(2):228–47.

[53] Koh DM, Collins DJ. Diffusion-Weighted MRI in the Body: Applications and Challenges in Oncology. *Am J Roentgenol*. 2007;**188**(6):1622–35.

[54] Moffat BA, Chenevert TL, Lawrence TS, Meyer CR, Johnson TD, Dong Q, et al. Functional diffusion map: A noninvasive MRI biomarker for early stratification of clinical brain tumor response. *Proc Natl Acad Sci U S A*. 2005;**102**(15):5524–9.

[55] Li SP, Padhani AR. Tumor response assessments with diffusion and perfusion MRI. *J Magn Reson Imaging*. 2012;**35**(4):745–63.

[56] Yankeelov TE, Gore JC. Dynamic Contrast Enhanced Magnetic Resonance Imaging in Oncology: Theory, Data Acquisition, Analysis, and Examples. *Curr Med Imaging Rev*. 2009;**3**(2):91–107.

[57] Ting YL, Bendel P. Thin-Section Mr Imaging of Rat-Brain at 4.7 T. *J Magn Reson Imaging*. 1992;**2**(4):393–9.

[58] Dortch RD, Does MD. Quantitative Measurement of T1, T2, T2*, and Proton Density. In: Yankeelov TE, Pickens DR, Price RR, editors. Quantitative MRI in Cancer. CRC Press; 2012. p. 53–65.

[59] Zhou Z, Lu Z-R. Gadolinium-Based Contrast Agents for MR Cancer Imaging. *Wiley Interdiscip Rev Nanomed Nanobiotechnol*. 2013;**5**(1):1–18.

[60] Folkman J, Bach M, Rowe JW, Davidoff F, Lambert P, Hirsch C, et al. Tumor Angiogenesis - Therapeutic Implications. *N Engl J Med*. 1971;**285**(21):1182 – &.

[61] Jain RK. Normalizing Tumor Microenvironment to Treat Cancer: Bench to Bedside to Biomarkers. *J Clin Oncol*. 2013;**31**(17):2205–18.

[62] Hygino da Cruz LC, Rodriguez I, Domingues RC, Gasparetto EL, Sorensen AG. Pseudoprogression and Pseudoresponse: Imaging Challenges in the Assessment of Posttreatment Glioma. *Am J Neuroradiol*. 2011;**32**(11):1978–85.

[63] Atuegwu NC, Gore JC, Yankeelov TE. The integration of quantitative multi-modality imaging data into mathematical models of tumors. *Phys Med Biol*. 2010;**55**(9):2429–49.

[64] Einstein A. Über die von der molekularkinetischen Theorie der Wärme geforderte Bewegung von in ruhenden Flüssigkeiten suspendierten Teilchen. *Ann Phys*. 1905;**322**(8):549–60.

[65] Barnes SL, Sorace AG, Loveless ME, Whisenant JG, Yankeelov TE. Correlation of tumor characteristics derived from DCE-MRI and DW-MRI with histology in murine models of breast cancer. *NMR Biomed*. 2015;

[66] Anderson AW, Xie J, Pizzonia J, Bronen RA, Spencer DD, Gore JC. Effects of cell volume fraction changes on apparent diffusion in human cells. *Magn Reson Imaging*. 2000;**18**(6):689–95.

[67] Guo Y, Cai Y-Q, Cai Z-L, Gao Y-G, An N-Y, Ma L, et al. Differentiation of clinically benign and malignant breast lesions using diffusion-weighted imaging. *J Magn Reson Imaging*. 2002;**16**(2):172–8.

[68] Sugahara T, Korogi Y, Kochi M, Ikushima I, Shigematu Y, Hirai T, et al. Usefulness of diffusion-weighted MRI with echo-planar technique in the evaluation of cellularity in gliomas. *J Magn Reson Imaging*. 1999;**9**(1):53–60.

[69] Humphries PD, Sebire NJ, Siegel MJ, Olsen ØE. Tumors in Pediatric Patients at Diffusion-weighted MR Imaging: Apparent Diffusion Coefficient and Tumor Cellularity. *Radiology*. 2007;**245**(3):848–54.

[70] Latour LL, Svoboda K, Mitra PP, Sotak CH. Time-dependent diffusion of water in a biological model system. *Proc Natl Acad Sci*. 1994;**91**(4):1229–33.

[71] van der Toorn A, Syková E, Dijkhuizen RM, Vořišek I, Vargová L, Škobisová E, et al. Dynamic changes in water ADC, energy metabolism, extracellular space volume, and tortuosity in neonatal rat brain during global ischemia. *Magn Reson Med*. 1996;**36**(1):52–60.

[72] Atuegwu NC, Colvin DC, Loveless ME, Xu L, Gore JC, Yankeelov TE. Incorporation of diffusion-weighted magnetic resonance imaging data into a simple mathematical model of tumor growth. *Phys Med Biol*. 2012;**57**(1):225–40.

[73] Weis JA, Miga MI, Arlinghaus LR, Li X, Abramson V, Chakravarthy AB, et al. Predicting the Response of Breast Cancer to Neoadjuvant Therapy Using a Mechanically Coupled Reaction diffusion Model. *Cancer Res*. 2015;

[74] Hormuth II DA, Weis JA, Barnes SL, Miga MI, Rericha EC, Quaranta V, et al. Predicting in vivo glioma growth with the reaction diffusion equation constrained by quantitative magnetic resonance imaging data. *Phys Biol*. 2015;**12**(4):46006.

[75] Colvin DC, Yankeelov TE, Does MD, Yue Z, Quarles C, Gore JC. New Insights into Tumor Microstructure Using Temporal Diffusion Spectroscopy. *Cancer Res*. 2008;**68**(14):5941–7.

[76] Prise KM, Schettino G, Folkard M, Held KD. New insights on cell death from radiation exposure. *Lancet Oncol*. 2005;**6**(7):520–8.

[77] Wouters BG, Begg AC. Irradiation-induced damage and the DNA damage response. In: Joiner M, van der Kogel A, editors. Basic Clinical Radiobiology. 4th ed. CRC Press; 2009. p. 11–26.

[78] Wouters BG. Cell death after irradiation: how, when and why cells die. In: Joiner MC, van

der Kogel AJ, editors. Basic Clinical Radiobiology. 4th ed. CRC Press; 2009. p. 27–40.

[79] Joiner MC. Quantifying cell kill and cell survival. In: Joiner MC, van der Kogel AJ, editors. Basic Clinical Radiobiology. 4th ed. 4: CRC Press; 2009. p. 41–55.

[80] Douglas BG, Fowler JF. The effect of multiple small doses of x rays on skin reactions in the mouse and a basic interpretation. *Radiat Res*. 1976;**66**(2):401–26.

[81] Curtis SB. Lethal and Potentially Lethal Lesions Induced by Radiation --- A Unified Repair Model. *Radiat Res*. 1986;**106**(2):252–70.

[82] Mitchell G. The rationale for fractionation in radiotherapy. *Clin J Oncol Nurs*. 2013;**17**(4):412–7.

[83] Kallman RF, Dorie MJ. Tumor oxygenation and reoxygenation during radiation theraphy: Their importance in predicting tumor response. *Int J Radiat Oncol*. 1986;**12**(4):681–5.

[84] Bentzen S. Repopulation in radiation oncology: perspectives of clinical research. *Int J Radiat Biol*. 2003;**79**(7):581–5.

[85] Kim JJ, Tannock IF. Repopulation of cancer cells during therapy: an important cause of treatment failure. *Nat Rev Cancer*. 2005;**5**(7):516–25.

[86] Delaney G, Jacob S, Featherstone C, Barton M. The role of radiotherapy in cancer treatment. *Cancer*. 2005;**104**(6):1129–37.

[87] Barani I, Larson D. Radiation Therapy of Glioblastoma. Current Understanding and Treatment of Gliomas SE - 4. 2015. p. 49–73.

[88] Walker MD, Alexander E, Hunt WE, MacCarty CS, Mahaley MS, Mealey J, et al. Evaluation of BCNU and/or radiotherapy in the treatment of anaplastic gliomas. *J Neurosurg*. 1978;**49**(3):333–43.

[89] Hermanto U, Frija EK, Lii MJ, Chang EL, Mahajan A, Woo SY. Intensity-modulated radiotherapy (IMRT) and conventional three-dimensional conformal radiotherapy for high-grade gliomas: Does IMRT increase the integral dose to normal brain? *Int J Radiat Oncol*. 2007;**67**(4):1135–44.

[90] Veldeman L, Madani I, Hulstaert F, De Meerleer G, Mareel M, De Neve W. Evidence behind use of intensity-modulated radiotherapy: a systematic review of comparative clinical studies. *Lancet Oncol*. 2008;**9**(4):367–75.

[91] Sheehan JP, Yen C-P, Lee C-C, Loeffler JS. Cranial Stereotactic Radiosurgery: Current Status of the Initial Paradigm Shifter. *J Clin Oncol*. 2014;**32**(26):2836–46.

[92] Nwokedi EC, DiBiase SJ, Jabbour S, Herman J, Amin P, Chin LS. Gamma Knife Stereotactic Radiosurgery for Patients with Glioblastoma Multiforme. *Neurosurgery*. 2002;**50**(1).

[93] Verellen D, Ridder M De, Linthout N, Tournel K, Soete G, Storme G. Innovations in image-guided radiotherapy. *Nat Rev Cancer*. 2007;**7**(12):949–60.

[94] Iliadis G, Kotoula V, Chatzisotiriou A, Televantou D, Eleftheraki A, Lambaki S, et al. Volumetric and MGMT parameters in glioblastoma patients: Survival analysis. *BMC Cancer*. 2012;**12**(1):3.

[95] Mayneord W V. On a Law of Growth of Jensen's Rat Sarcoma. *Am J Cancer*. 1932;**16**(4):841–6.

[96] Collins VP, Loeffler RK, Tivey H. Observations on growth rates of human tumors. *Am J Roentgenol Radium Ther Nucl Med*. 1956;**76**(5):988–1000.

[97] Gerlee P. The Model Muddle: In Search of Tumor Growth Laws. *Cancer Res*. 2013;**73**(8):2407–11.

[98] Benzekry S, Lamont C, Beheshti A, Tracz A, Ebos JML, Hlatky L, et al. Classical Mathematical Models for Description and Prediction of Experimental Tumor Growth. *PLoS Comput Biol*. 2014;**10**(8):e1003800.

[99] Piotrowska MJ, Angus SD. A quantitative cellular automaton model of in vitro multicellular spheroid tumour growth. *J Theor Biol*. 2009;**258**(2):165–78.

[100] Gevertz JL, Gillies GT, Torquato S. Simulating tumor growth in confined heterogeneous environments. *Phys Biol*. 2008;**5**(3):036010.

[101] Alarcón T, Byrne HM, Maini PK. A cellular automaton model for tumour growth in inhomogeneous environment. *J Theor Biol*. 2003;**225**(2):257–74.

[102] Swanson KR, Alvord EC, Murray JD. A quantitative model for differential motility of gliomas in grey and white matter. *Cell Prolif*. 2000;**33**(5):317–29.

[103] Anderson ARA, Quaranta V. Integrative mathematical oncology. *Nat Rev Cancer*. 2008;**8**(3):227–34.

[104] Frieboes HB, Jin F, Chuang Y-L, Wise SM, Lowengrub JS, Cristini V. Three-dimensional multispecies nonlinear tumor growth-II: Tumor invasion and angiogenesis. *J Theor Biol*. 2010;**264**(4):1254–78.

[105] Folkman J, Hochberg M. Self-regulation of growth in three dimensions. *J Exp Med*. 1973;**138**(4):745–53.

[106] Freyer JP, Sutherland RM. Selective Dissociation and Characterization of Cells from Different Regions of Multicell Tumor Spheroids. *Cancer Res*. 1980;**40**(11):3956–65.

[107] Anderson AR. A hybrid mathematical model of solid tumour invasion: the importance of cell adhesion. *Math Med Biol*. 2005;**22**(2):163–86.

[108] Gatenby RA, Gawlinski ET. A Reaction diffusion Model of Cancer Invasion. *Cancer Res*. 1996;**56**(24):5745–53.

[109] Garg I, Miga MI. Preliminary investigation of the inhibitory effects of mechanical stress in tumor growth. Proc SPIE. Proc. SPIE; 2008. p. 69182L – 69182L – 11.

[110] Gooya A, Biros G, Davatzikos C. Deformable Registration of Glioma Images Using EM Algorithm and Diffusion Reaction Modeling. *IEEE Trans Med Imaging*. 2011;**30**(2):375–90.

[111] Turing AM. The Chemical Basis of Morphogenesis. *Philos Trans R Soc London B Biol Sci*. 1952;**237**(641):37–72.

[112] Chaplain MAJ, Ganesh M, Graham IG. Spatio-temporal pattern formation on spherical surfaces: numerical simulation and application to solid tumour growth. *J Math Biol*. 2001;**42**(5):387–423.

[113] Chen X, Summers RM, Yao J. Kidney Tumor Growth Prediction by Coupling Reaction diffusion and Biomechanical Model. Biomedical Engineering, IEEE Transactions on. 2013. p. 169–73.

[114] Baldock A, Rockne R, Boone A, Neal M, Bridge C, Guyman L, et al. From Patient-Specific Mathematical Neuro-Oncology to Precision Medicine. *Front Oncol*. 2013;**3**.

[115] Swanson KR, Harpold HLP, Peacock DL, Rockne R, Pennington C, Kilbride L, et al. Velocity of Radial Expansion of Contrast-enhancing Gliomas and the Effectiveness of Radiotherapy in Individual Patients: a Proof of Principle. *Clin Oncol*. 2008 May;**20**(4):301–8.

[116] Wang CH, Rockhill JK, Mrugala M, Peacock DL, Lai A, Jusenius K, et al. Prognostic significance of growth kinetics in newly diagnosed glioblastomas revealed by combining serial imaging with a novel biomathematical model. *Cancer Res*. 2009;**69**(23):9133–40.

[117] Milosevic GP and MK and SS and AO and M. Mathematical modeling of brain tumors: effects of radiotherapy and chemotherapy. *Phys Med Biol*. 2007;**52**(11):3291.

[118] Rockne RC, Trister AD, Jacobs J, Hawkins-Daarud AJ, Neal ML, Hendrickson K, et al. A patient-specific computational model of hypoxia-modulated radiation resistance in glioblastoma using (18)F-FMISO-PET. *J R Soc Interface*. 2015;**12**(103):20141174.

[119] Rockne R, Rockhill JK, Mrugala M, Spence a M, Kalet I, Hendrickson K, et al. Predicting

the efficacy of radiotherapy in individual glioblastoma patients in vivo: a mathematical modeling approach. *Phys Med Biol*. 2010;**55**(12):3271–85.

[120] Rockne R, Alvord EC, Rockhill JK, Swanson KR. A mathematical model for brain tumor response to radiation therapy. *J Math Biol*. 2009;**58**(4-5):561–78.

[121] Badoual M, Gerin C, Deroulers C, Grammaticos B, Llitjos J-F, Oppenheim C, et al. Oedema-based model for diffuse low-grade gliomas: application to clinical cases under radiotherapy. *Cell Prolif*. 2014;**47**(4):369–80.

[122] Corwin D, Holdsworth C, Rockne RC, Trister AD, Mrugala MM, Rockhill JK, et al. Toward Patient-Specific, Biologically Optimized Radiation Therapy Plans for the Treatment of Glioblastoma. *PLoS One*. 2013;**8**(11):e79115.

[123] Phillips CHH and DC and RDS and RR and ADT and KRS and M. Adaptive IMRT using a multiobjective evolutionary algorithm integrated with a diffusion–invasion model of glioblastoma. *Phys Med Biol*. 2012;**57**(24):8271.

[124] Bondiau P-Y, Konukoglu E, Clatz O, Delingette H, Frenay M, Paquis P. Biocomputing: numerical simulation of glioblastoma growth and comparison with conventional irradiation margins. *Phys Med*. 2011;**27**(2):103–8.

[125] Gammon K. Mathematical modelling: Forecasting cancer. *Nature*. 2012;**491**(7425):S66–7.

[126] Savage N. Modelling: Computing cancer. *Nature*. 2012;**491**(7425):S62–3.

[127] Russell SM, Elliott R, Forshaw D, Golfinos JG, Nelson PK, Kelly PJ. Glioma vascularity correlates with reduced patient survival and increased malignancy. *Surg Neurol*. 2009;**72**(3):242–6.

[128] Brown JM, Wilson WR. Exploiting tumour hypoxia in cancer treatment. *Nat Rev Cancer*. 2004 Jun;**4**(6):437–47.

[129] Suit H, Skates S, Taghian A, Okunieff P, Efird JT. Clinical implications of heterogeneity of

tumor response to radiation therapy. *Radiother Oncol*. 1992;**25**(4):251–60.

[130] Au JL, Jang SH, Zheng J, Chen C-T, Song S, Hu L, et al. Determinants of drug delivery and transport to solid tumors. *J Control Release*. 2001;**74**(1–3):31–46.

[131] Østergaard L. Principles of cerebral perfusion imaging by bolus tracking. *J Magn Reson Imaging*. 2005;**22**(6):710–7.

[132] Padhani AR, Krohn KA, Lewis JS, Alber M. Imaging oxygenation of human tumours. *Eur Radiol*. 2007;**17**(4):861–72.

[133] Christen T, Lemasson B, Pannetier N, Farion R, Segebarth C, Rémy C, et al. Evaluation of a quantitative blood oxygenation level-dependent (qBOLD) approach to map local blood oxygen saturation. *NMR Biomed*. 2011;**24**(4):393–403.

[134] Colvin DC, Loveless ME, Does MD, Yue Z, Yankeelov TE, Gore JC. Earlier detection of tumor treatment response using magnetic resonance diffusion imaging with oscillating gradients. *Magn Reson Imaging*. 2011;**29**(3):315–23.

[135] Whisenant JG, Ayers GD, Loveless ME, Barnes SL, Colvin DC, Yankeelov TE. Assessing reproducibility of diffusion-weighted magnetic resonance imaging studies in a murine model of HER2+ breast cancer. *Magn Reson Imaging*. 2014;**32**(3):245–9.

[136] Martin I, Dozin B, Quarto R, Cancedda R, Beltrame F. Computer-based technique for cell aggregation analysis and cell aggregation in in vitro chondrogenesis. *Cytometry*. 1997;**28**(2):141–6.

[137] Rouzaire-Dubois B, Milandri JB, Bostel S, Dubois JM. Control of cell proliferation by cell volume alterations in rat C6 glioma cells. *Pflugers Arch*. 2000;**440**(6):881–8.

[138] Joachimowicz N, Pichot C, Hugonin J-P. Inverse scattering: an iterative numerical method for electromagnetic imaging. *IEEE Trans Antennas Propag*. 1991;**39**(12):1742–53.

[139] Ou J, Ong RE, Yankeelov TE, Miga MI. Evaluation of 3D modality-independent

elastography for breast imaging: a simulation study. *Phys Med Biol*. 2008;**53**(1):147.

[140] Lin LI. A concordance correlation coefficient to evaluate reproducibility. *Biometrics*. 1989;**45**(1):255–68.

[141] Dice LR. Measures of the Amount of Ecologic Association Between Species. *Ecology*. 1945;**26**(3):297–302.

[142] Yankeelov TE, Abramson RG, Quarles CC. Quantitative multimodality imaging in cancer research and therapy. *Nat Rev Clin Oncol*. 2014;**11**(11):670–80.

[143] Freyer JP. Role of Necrosis in Regulating the Growth Saturation of Multicellular Spheroids. *Cancer Res*. 1988;**48**(9):2432–9.

[144] Lacroix M, Abi-Said D, Fourney DR, Gokaslan ZL, Shi W, DeMonte F, et al. A multivariate analysis of 416 patients with glioblastoma multiforme: prognosis, extent of resection, and survival. *J Neurosurg*. 2001;**95**(2):190–8.

[145] Gyllenberg M, Webb G. Quiescence as an explanation of Gompertzian tumor growth. *Growth Dev Aging*. 1989;**53**(1-2):25–33.

[146] Sherar MD, Noss MB, Foster FS. Ultrasound backscatter microscopy images the internal structure of living tumour spheroids. *Nature*. 1987;**330**(6147):493–5.

[147] Helmlinger G, Netti PA, Lichtenbeld HC, Melder RJ, Jain RK. Solid stress inhibits the growth of multicellular tumor spheroids. *Nat Biotech*. 1997;**15**(8):778–83.

[148] Giese A, Bjerkvig R, Berens ME, Westphal M. Cost of Migration: Invasion of Malignant Gliomas and Implications for Treatment. *J Clin Oncol*. 2003;**21**(8):1624–36.

[149] Demuth T, Berens M. Molecular Mechanisms of Glioma Cell Migration and Invasion. *J Neurooncol*. Kluwer Academic Publishers; 2004;**70**(2):217–28.

[150] Wong KL, Summers R, Kebebew E, Yao J. Tumor Growth Prediction with Hyperelastic Biomechanical Model, Physiological Data Fusion, and Nonlinear Optimization. Medical Image Computing and Computer-Assisted Intervention – MICCAI 2014 SE - 4. 2014. p. 25–32.

[151] Atuegwu NC, Arlinghaus LR, Li X, Chakravarthy AB, Abramson VG, Sanders ME, et al. Parameterizing the Logistic Model of Tumor Growth by DW-MRI and DCE-MRI Data to Predict Treatment Response and Changes in Breast Cancer Cellularity during Neoadjuvant Chemotherapy. *Transl Oncol*. 2013;**6**(3):256–64.

[152] Shiroishi MS, Castellazzi G, Boxerman JL, D'Amore F, Essig M, Nguyen TB, et al. Principles of T2*-weighted dynamic susceptibility contrast MRI technique in brain tumor imaging. *J Magn Reson Imaging*. 2015;**41**(2):296–313.

[153] Kelloff GJ, Hoffman JM, Johnson B, Scher HI, Siegel BA, Cheng EY, et al. Progress and Promise of FDG-PET Imaging for Cancer Patient Management and Oncologic Drug Development. *Clin Cancer Res*. 2005;**11**(8):2785–808.

[154] Imam SK. Review of positron emission tomography tracers for imaging of tumor hypoxia. *Cancer Biother Radiopharm*. 2010;**25**(3):365–74.

[155] Wise SM, Lowengrub JS, Frieboes HB, Cristini V. Three-dimensional multispecies nonlinear tumor growth — I Model and numerical method. *J Theor Biol*. 2008;**253**:524–43.

[156] Macklin P, McDougall S, Anderson AR a, Chaplain M a J, Cristini V, Lowengrub J. Multiscale modelling and nonlinear simulation of vascular tumour growth. *J Math Biol*. 2009;**58**(4-5):765–98.

[157] Sherratt JA, Chaplain MAJ. A new mathematical model for avascular tumour growth. *J Math Biol*. 2001;**43**(4):291–312.

[158] Byrne H, Preziosi L. Modelling solid tumour growth using the theory of mixtures. *Math Med Biol*. 2003;**20**(4):341–66.

[159] Jain RK, Martin JD, Stylianopoulos T. The Role of Mechanical Forces in Tumor Growth

and Therapy. *Annu Rev Biomed Eng*. 2014;**16**(1):321–46.

[160] Cheng G, Tse J, Jain RK, Munn LL. Micro-Environmental Mechanical Stress Controls Tumor Spheroid Size and Morphology by Suppressing Proliferation and Inducing Apoptosis in Cancer Cells. *PLoS One*. 2009;**4**(2):e4632.

[161] Swanson KR, Rockne RC, Claridge J, Chaplain M a, Alvord EC, Anderson AR a. Quantifying the role of angiogenesis in malignant progression of gliomas: in silico modeling integrates imaging and histology. *Cancer Res*. 2011;**71**(24):7366–75.

[162] Hawkins-Daarud A, Rockne RC, Anderson ARA, Swanson KR. Modeling tumor-associated edema in gliomas during anti-angiogenic therapy and its impact on imageable tumor. *Front Oncol*. 2013;**3**.

[163] Kaufman LJ, Brangwynne CP, Kasza KE, Filippidi E, Gordon VD, Deisboeck TS, et al. Glioma Expansion in Collagen I Matrices: Analyzing Collagen Concentration-Dependent Growth and Motility Patterns. *Biophys J*. 2005;**89**(1):635–50.

[164] Gordon VD, Valentine MT, Gardel ML, Andor-Ardó D, Dennison S, Bogdanov AA, et al. Measuring the mechanical stress induced by an expanding multicellular tumor system: a case study. *Exp Cell Res*. 2003;**289**(1):58–66.

[165] Elkin BS, Ilankovan AI, Morrison III B. A detailed viscoelastic characterization of the P17 and adult rat brain. *J Neurotrauma*. 2011;**28**:2235+.

[166] Lee SJ, King MA, Sun J, Xie HK, Subhash G, Sarntinoranont M. Measurement of viscoelastic properties in multiple anatomical regions of acute rat brain tissue slices. *J Mech Behav Biomed Mater*. 2014;**29**(0):213–24.

[167] Korobenko L, Braverman E. A logistic model with a carrying capacity driven diffusion. *Can Appl Math Q*. 2009;**17**(1):85–104.

[168] Doblas S, He T, Saunders D, Pearson J, Hoyle J, Smith N, et al. Glioma morphology and tumor-induced vascular alterations revealed in seven rodent glioma models by in vivo magnetic resonance imaging and angiography. *J Magn Reson Imaging*. 2010;**32**(2):267–75.

[169] Huston III J. Magnetic Resonance Elastography of the Brain. Magnetic Resonance Elastography SE - 8. 2014. p. 89–98.

[170] Quaranta V, Rejniak K a, Gerlee P, Anderson AR a. Invasion emerges from cancer cell adaptation to competitive microenvironments: quantitative predictions from multiscale mathematical models. *Semin Cancer Biol*. 2008;**18**(5):338–48.

[171] Byrne HM, Chaplain MA. Necrosis and Apoptosis: Distinct Cell Loss Mechanisms in a Mathematical Model of Avascular Tumour Growth. *J Theor Med*. 1998;**1**(3):223–35.

[172] Kiran KL, Jayachandran D, Lakshminarayanan S. Mathematical modelling of avascular tumour growth based on diffusion of nutrients and its validation. *Can J Chem Eng*. 2009;**87**(5):732–40.

[173] Alarcón T, Byrne HM, Maini PK. A multiple scale model for tumor growth. *Multiscale Model Simul*. 2005;**3**(2):440–75.

[174] Yaes RJ, Patel P, Maruyama Y. On using the linear-quadratic model in daily clinical practice. *Int J Radiat Oncol*. 1991;**20**(6):1353–62.

[175] Bentzen SM, Joiner MC. The linear-quadratic approach in clinical practice. In: Joiner MC, van der Kogel AJ, editors. Basic Clinical Radiobiology. 4th ed. CRC Press; 2009. p. 120–34.

[176] Antipas VP, Stamatakos GS, Uzunoglu NK. A Patient-specific in vivo Tumor and Normal Tissue Model for Prediction of the Response to Radiotherapy. *Methods Inf Med*. 2007;**46**(3):367–75.

[177] Parthymou A, Kardamakis D, Pavlopoulos I, Papadimitriou E. Irradiated C6 glioma cells induce angiogenesis in vivo and activate endothelial cells in vitro. *Int J Cancer*. 2004;**110**(6):807–14.

[178] Bencokova Z, Pauron L, Devic C, Joubert A, Gastaldo J, Massart C, et al. Molecular and cellular response of the most extensively used rodent glioma models to radiation and/or cisplatin. *J Neurooncol*. 2008;**86**(1):13–21.

[179] Prokopiou S, Moros EG, Poleszczuk J, Caudell J, Torres-Roca JF, Latifi K, et al. A proliferation saturation index to predict radiation response and personalize radiotherapy fractionation. *Radiat Oncol*. 2015;**10**(1):1–8.

[180] Deasy JJ and KIS and JO. Modelling the interplay between hypoxia and proliferation in radiotherapy tumour response. *Phys Med Biol*. 2013;**58**(14):4897.

[181] Titz B, Jeraj R, Jeraj BT and R. An imaging-based tumour growth and treatment response model: Investigating the effect of tumour oxygenation on radiation therapy response. *Phys Med Biol* [Internet]. 2008;**53**(17):4471. Available from: http://stacks.iop.org/0031-9155/53/i=17/a=001

[182] Vaupel P, Mayer A. Hypoxia in cancer: significance and impact on clinical outcome. *Cancer Metastasis Rev*. 2007;**26**(2):225–39.

[183] Vaupel P, Kallinowski F, Okunieff P. Blood Flow, Oxygen and Nutrient Supply, and Metabolic Microenvironment of Human Tumors: A Review. *Cancer Res*. 1989;**49**(23):6449–65.

[184] Kirkpatrick JP, Meyer JJ, Marks LB. The Linear-Quadratic Model Is Inappropriate to Model High Dose per Fraction Effects in Radiosurgery. *Semin Radiat Oncol*. 2008;**18**(4):240–3.

[185] Brenner DJ. The Linear-Quadratic Model Is an Appropriate Methodology for Determining Isoeffective Doses at Large Doses Per Fraction. *Semin Radiat Oncol*. 2008;**18**(4):234–9.

[186] Bauman GS, Fisher BJ, McDonald W, Amberger VR, Moore E, Del Maestro RF. Effects of radiation on a three-dimensional model of malignant glioma invasion. *Int J Dev Neurosci*. 1999;**17**(5–6):643–51.

[187] Huang RY, Neagu MR, Reardon DA, Wen PY. Pitfalls in the Neuroimaging of Glioblastoma in the Era of Antiangiogenic and Immuno/Targeted Therapy – Detecting Illusive Disease, Defining Response. *Front Neurol* [Internet]. Frontiers Media S.A.; 2015 Feb 23;**6**:33. Available from: http://www.ncbi.nlm.nih.gov/pmc/articles/PMC4337341/

[188] Boxerman JL, Ellingson BM, Jeyapalan S, Elinzano H, Harris RJ, Rogg JM, et al.

Longitudinal DSC-MRI for Distinguishing Tumor Recurrence From Pseudoprogression in Patients With a High-grade Glioma. *Am J Clin Oncol*. 9000;**Publish Ah**.

[189] Wang S, Martinez-Lage M, Sakai Y, Chawla S, Kim SG, Alonso-Basanta M, et al. Differentiating Tumor Progression from Pseudoprogression in Patients with Glioblastomas Using Diffusion Tensor Imaging and Dynamic Susceptibility Contrast MRI. *Am J Neuroradiol*. 2015;

[190] Hu LS, Eschbacher JM, Heiserman JE, Dueck AC, Shapiro WR, Liu S, et al. Reevaluating the imaging definition of tumor progression: perfusion MRI quantifies recurrent glioblastoma tumor fraction, pseudoprogression, and radiation necrosis to predict survival. *Neuro Oncol*. 2012;

[191] Young RJ, Gupta A, Shah AD, Graber JJ, Zhang Z, Shi W, et al. Potential utility of conventional MRI signs in diagnosing pseudoprogression in glioblastoma. *Neurology*. 2011;**76**(22):1918–24.

[192] Fernandez-Palomo C, Mothersill C, Bräuer-Krisch E, Laissue J, Seymour C, Schültke E. γ-H2AX as a Marker for Dose Deposition in the Brain of Wistar Rats after Synchrotron Microbeam Radiation. *PLoS One*. 2015;**10**(3):e0119924.

[193] Kondziolka D, Somaza S, Comey C, Lunsford LD, Claassen D, Pandalai S, et al. Radiosurgery and fractionated radiation therapy: comparison of different techniques in an in vivo rat glioma model. *J Neurosurg*. 1996;**84**(6):1033–8.

[194] Taal W, Brandsma D, de Bruin HG, Bromberg JE, Swaak-Kragten AT, Sillevis Smitt PAE, et al. Incidence of early pseudo-progression in a cohort of malignant glioma patients treated with chemoirradiation with temozolomide. *Cancer*. 2008;**113**(2):405–10.

[195] Sundgren PC, Fan X, Weybright P, Welsh RC, Carlos RC, Petrou M, et al. Differentiation of recurrent brain tumor versus radiation injury using diffusion tensor imaging in patients with new contrast-enhancing lesions. *Magn Reson Imaging*. 2016;**24**(9):1131–42.

[196] Tsien C, Galbán CJ, Chenevert TL, Johnson TD, Hamstra DA, Sundgren PC, et al. Parametric Response Map As an Imaging Biomarker to Distinguish Progression From Pseudoprogression in High-Grade Glioma. *J Clin Oncol*. 2010;**28**(13):2293–9.

[197] Gahramanov S, Raslan AM, Muldoon LL, Hamilton BE, Rooney WD, Varallyay CG, et al. Potential for Differentiation of Pseudoprogression From True Tumor Progression With Dynamic Susceptibility-Weighted Contrast-Enhanced Magnetic Resonance Imaging Using Ferumoxytol vs. Gadoteridol: A Pilot Study. *Int J Radiat Oncol*. 2011;**79**(2):514–23.

[198] Sundgren PC. MR Spectroscopy in Radiation Injury. *Am J Neuroradiol*. 2009;**30**(8):1469–76.

[199] Semmineh NB, Xu J, Skinner JT, Xie J, Li H, Ayers G, et al. Assessing tumor cytoarchitecture using multiecho DSC-MRI derived measures of the transverse relaxivity at tracer equilibrium (TRATE). *Magn Reson Med*. 2015;**74**(3):772–84.

[200] Hanahan D, Weinberg RA. Hallmarks of Cancer: The Next Generation. *Cell*. 2011;**144**(5):646–74.

[201] Raza SM, Lang FF, Aggarwal BB, Fuller GN, Wildrick DM, Sawaya R. Necrosis and Glioblastoma: A Friend or a Foe? A Review and a Hypothesis. *Neurosurgery*. United States; 2002 Jul;**51**(1):2–3.

[202] Barker FG, Davis RL, Chang SM, Prados MD. Necrosis as a prognostic factor in glioblastoma multiforme. *Cancer*. 1996;**77**(6):1161–6.

[203] Sutherland RM. Cell and Environment Interactions in Tumor Microregions: The Multicell Spheroid Model. *Science (80-)*. 1988;**240**(4849):177.

[204] Kim JH, Khil MS, Kolozsvary A, Gutierrez JA, Brown SL. Fractionated radiosurgery for 9L gliosarcoma in the rat brain. *Int J Radiat Oncol*. 1999;**45**(4):1035–40.

[205] Hartung M, Grist T, Francois C. Magnetic resonance angiography: current status and future directions. *J Cardiovasc Magn Reson*. 2011;**13**(1):19.

[206] Buerkle A, Weber W a. Imaging of tumor glucose utilization with positron emission tomography. *Cancer Metastasis Rev*. 2008;**27**(4):545–54.

[207] Walker-Samuel S, Ramasawmy R, Torrealdea F, Rega M, Rajkumar V, Johnson SP, et al. In vivo imaging of glucose uptake and metabolism in tumors. *Nat Med* [Internet]. Nature Publishing Group, a division of Macmillan Publishers Limited. All Rights Reserved.; 2013 Aug;**19**(8):1067–72. Available from: http://dx.doi.org/10.1038/nm.3252

[208] Barth R, Kaur B. Rat brain tumor models in experimental neuro-oncology: the C6, 9L, T9, RG2, F98, BT4C, RT-2 and CNS-1 gliomas. *J Neurooncol*. 2009;**94**(3):299–312.

[209] Szeto MD, Chakraborty G, Hadley J, Rockne R, Muzi M, Alvord EC, et al. Quantitative metrics of net proliferation and invasion link biological aggressiveness assessed by MRI with hypoxia assessed by FMISO-PET in newly diagnosed glioblastomas. *Cancer Res*. 2009;**69**(10):4502–9.

[210] Gerlee P, Anderson a R a. A hybrid cellular automaton model of clonal evolution in cancer: the emergence of the glycolytic phenotype. *J Theor Biol*. 2008;**250**(4):705–22.

[211] Choi IY, Lee SP, Kim SG, Gruetter R. In vivo measurements of brain glucose transport using the reversible Michaelis-Menten model and simultaneous measurements of cerebral blood flow changes during hypoglycemia. *J Cereb Blood Flow Metab*. 2001;**21**(6):653–63.

[212] Barnes SL, Whisenant JG, Loveless ME, Ayers GD, Yankeelov TE. Assessing the reproducibility of dynamic contrast enhanced magnetic resonance imaging in a murine model of breast cancer. *Magn Reson Med*. 2012;**000**(February).

[213] Barth RF. Rat brain tumor models in experimental neuro-oncology: The 9L, C6, T9, F98, RG2 (D74), RT-2 and CNS-1 gliomas. *J Neurooncol*. 1998;**36**(1):91–102.